Photomagnetic Cobalt hexacyanidoferrate(III) Prussian Blue Analogues probed by X-ray Magnetic Circular Dichroism (XMCD)

Sadaf Fatima

Université Pierre et Marie Curie

Thèse de doctorat présentée par :

Sadaf Fatima

Pour obtenir le grade de :

DOCTEUR de l'UNIVERSITÉ PIERRE ET MARIE CURIE (PARIS)

Spécialité : Physique et chimie des matériaux

Photomagnetic Cobalt hexacyanidoferrate(III) Prussian Blue Analogues probed by X-ray Magnetic Circular Dichroism (XMCD)

Soutenue le 28 septembre 2016 devant le jury composé de :

Pr Corine Mathonière	Univ. Bordeaux (ICMCB)	Examinateur
Pr Eric Collet	Univ. Rennes 1 (IPR)	Rapporteur
Pr Rodrigue Lescouëzec	Univ. Pierre et Marie-Curie (IPCM)	Examinateur
Pr Talal Mallah	Univ. Paris-Sud (ICMMO)	Examinateur
Dr Philippe Sainctavit	Univ. Pierre et Marie-Curie (IMPMC)	Directeur de thèse
Pr Cyrille Train	Univ. Grenoble (LNCMI)	Rapporteur

École doctorale Physique et chimie des matériaux – ED 397

Institut de Minéralogie, de Physique des Matériaux et de Cosmochimie – UMR 7590

Acknowledgements

Paris was a foreign land to me when I first arrived here four years ago to pursue my higher education, and now it has become a home away from home which has made me understand the true meaning of the quote by Victor Hugo: “To study in Paris is to be born in Paris!” Undoubtedly, Paris with its great art history, picturesque landmarks and mesmerizing scenic beauty, cross-cultural ambiance on one hand and being the hub of cutting-edge scientific research on the other hand is an ideal place for anyone who seeks Eudaimonia (human flourishing). I admit that living and studying at Paris will always be a wonderful experience of my life which I can never forget.

The quality years of my life that I devoted to my doctoral research were full of adventures and if I put it another way more precisely it is correct to say my PhD was never less than a roller coaster ride. Performing experiments, handling the pressure to get the good results, group meetings, presentations, time management, meeting the deadlines and sleepless nights at synchrotron during beamtimes are few things to mention in the long list of my journey as a PhD researcher. First of all, I am thankful to my PhD advisor Philippe SAINCTAVIT who had been a great mentor throughout my PhD project. I was privileged to work under his supervision and to learn from him. He always encouraged me to present my research work in many conferences. It was his support due to which I presented my work in several conferences, summer school and synchrotron users’ meetings in France, Russia, Germany and Brazil. Despite being the head of the team MIMABADI at IMPMC and the director of research CNRS, his undivided attention towards my PhD project was commendable. I really appreciate his guidance and dedication! I look forward to learn more from him if I get any opportunity in my future research projects to collaborate. Besides, I would like to thank my other team members, Marie-Anne ARRIO and Amélie JUHIN for their encouragement and support during my PhD. I would like to thank for the help they provided me for Ligand Field Multiplet Calculations.

I would like to thank Prof. Eric COLLET and Prof. Cyrille TRAIN for their valuable time they dedicated to review my PhD manuscript. I am very thankful Prof. Talal MALLAH, Prof. Corine MATHONIERE and Prof Rodrigue LESCOUEZEC for their participation in the PhD defense jury.

My special thanks to my collaborators Corine MATHONIERE (ICMCB), Rodolphe CLERAC (CRPP) and Evangelia S. KOUMOUSI (ICMCB, CRPP) from University of Bordeaux on the project of dinuclear Prussian Blue Analogues. Our meetings and discussions at the beamtimes were very fruitful and helped me learn from your experiences. I would like to thank Eva for her help during the beamtimes. Eva, a brilliant chemist trained under Corine and Rodolphe, who synthesized the beautiful samples of photomagnetic dinuclear complexes and their precursors for the XMCD measurements at synchrotron. When a physicist meets a chemist wonderful things happen. This is true in fact! And I am looking forward to our publications together on two dinuclear complexes in near future.

My deepest thanks to my collaborators from ICMMO on the project of tridimensional Prussian Blue Analogues: Anne BLEUZEN, Amélie BORDAGE and Robinson MOULIN. My sincere thanks to Christophe CARTIER DIT MOULIN and Loïc JOLY.

I also would like to thank all the beamline staff from DEIMOS beamline (SOLEIL, France), ID12 beamline(ESRF, France) and SIM beamline(SLS, Switzerland) for their technical support. Beamtimes are tiring and stressful and the beamline staff does whatever it takes to help experiments run smoothly. Special thanks to Edwige OTERO from DEIMOS beamline (SOLEIL, France) and Fabrice Wilhelm from ID12 beamline (ESRF, France) for their help during the experiments.

I would like to thank my colleagues, friends and Post docs at IMPMC with whom I have shared some great moments. Florent, Nadejda, Nieli, Aisha, Ruidy, Mathieu, Lousiane Sara, Manoj, Myrtille, Vincent, Adrient, Nicholas,Areej, Sandy, Pauline, Natan, Guilherme, Henri and Maud. Friends outside the lab have been invaluable. I would like to thank Soria, Florian, Maria, Julie, Eva and David. They were fully confident that I would nail my PhD defense.

My hearfelt appreciation is for my mentor Dr. Sadia MANZOOR who always supported me and encouraged me. She recognized and appreciated my talent. I would like to thank my undergraduate advisor Dr. Iqbal Ahmed KHAN, a dedicated teacher who used to tell me, “Sadaf always do things in the best possible way.”

I would like to thank Erasmus Mundus Europe Asia (EMEA) program which provided me the opportunity to study the NANOMAT masters at University of Pierre and Marie Curie (UPMC) as Erasmus Mundus Scholar and to discover the French culture. Many thanks to my mentors during my NANOMAT masters at INSP (UPMC): Prof. William SACKS, Prof. Nadine WITKOWSKI and Prof. Masimiliano MARANGOLO. I also would like to thank ecole doctorale 397 “Physics and Chemistry of Materials” to give me PhD scholarship to pursue my research at UPMC.

Finally, I thank my dear family for their love and support. Thanks to my siblings who always cheered me up which helped me to accomplish my projects in time. I owe a lot to my lovely sisters Batool and Andaleeb who always believed in me. Thank you for your unconditional love! Thank you my dear sister Batool for being always there for me. You never got tired listening to my stories, daily struggles and achievements. I will never forget our “special” sarcastic jokes and laughter moments. I am confident to say that there is a great part of yours in the success of this doctoral thesis. My special thanks is for my loving parents whose love and care made me who I am today. You have always given me freedom to discover my true potential. I love you papa and mama and I dedicate my doctoral thesis to both of you. P.S: A huge thanks to all the wonderful people I have met so far, the great scientists, friends and mentors who have inspired me!

Sadaf Fatima Jafri

Paris, September 2016.

Dedicated to my loving parents...

"I have discovered the secret that after climbing a great hill, one only finds that there are many more hills to climb. I have taken a moment here to rest, to steal a view of the glorious vista that surrounds me, to look back on the distance I have come. But I can only rest for a moment, for with freedom come responsibilities, and I dare not linger, for my long walk is not ended."

Nelson Mandela, Long Walk to Freedom

Résumé

Les analogues du bleu de Prusse contenant du Fe et du Co (Fe/Co PBA) sont des complexes moléculaires qui présentent des propriétés physiques bistables. Par conséquent, ils sont considérés comme des candidats potentiels pour le stockage d'informations à base de molécules. Cette thèse vise à étudier la structure électronique et magnétique de Fe/Co PBA en utilisant des techniques expérimentales et théoriques avancées. Les techniques X-ray Absorption Spectroscopy (XAS) et X-ray magnetic circular dichroism (XMCD) combinées avec la théorie des multiplets en champ de ligands (LFM) sonde le changement dans les propriétés magnétiques macroscopiques de Fe/Co PBA et peuvent donner des informations locales sur les centres métalliques des complexes. Les spectres XAS et XMCD aux seuils $L_{2,3}$ du Fe et du Co sont simulés en utilisant la LFM. Le composé tridimensionnel RbCoFe PBA, deux complexes de dinucléaire photomagnétiques et les précurseurs de Fe sont étudiés.

L'étude de XMCD combinée avec la LFM a révélé une grande valeur du moment magnétique d'orbite du précurseur FeTp. Une étude détaillée a été effectuée pour vérifier les règles de somme d'orbite et de spin dans le cas des ions de Fe^{III} bas spin et il a été constaté que la règle spin somme n'était pas valide à cause de l'entremélange des seuils L_2 et L_3. L'enquête XMCD des complexes dinucléaires photomagnétiques a confirmé le transfert d'électrons métal-métal. Cette enquête XMCD de la plus petite unité de la famille Fe / Co PBA est utile pour comprendre les propriétés magnétiques de la famille de Fe / Co PBA. L'étude XMCD sur aux seuils K du Fe et du Co d'un composé tridimensionnel RbCoFe PBA a prouvé l'existence d'une interaction antiferromagnétique entre les ions métalliques de Fe et de Co dans l'état photoinduit.

Mots-clés:

bleu de prusse analogues, photomagnetism, Fe, Co, XAS, XMCD, seuils $L_{2,3}$, seuils K.

Abstract

The Fe/Co Prussian Blue Analogues (PBA) are molecular complexes that exhibit externally controlled bistable physical properties. Thus, they are considered as potential candidates for photoswitchable molecule-based information storage. This thesis aims to investigate the electronic and magnetic structure of Fe/Co PBA using advanced experimental and theoretical techniques. X-ray Absorption Spectroscopy (XAS) and X-ray Magnetic Circular Dichroism (XMCD) techniques combined with Ligand Field Multiplet (LFM) theory probe the change in the macroscopic magnetic properties of PBA and can give local information about the metal centers existing in the complexes. The XAS and XMCD spectra at Fe and Co $L_{2,3}$ edges are simulated using Ligand Field Multiplet (LFM) Calculations. The tridimensional RbCoFe PBA, two photomagnetic dinculear complexes and the building blocks Fe-bearing precursors are investigated.

The XMCD study combined with LFM investigation revealed a large value of orbital magnetic moment in FeTp precursor of the dinuclear complex. A detailed study has been performed to check for the orbit and spin sum rules in the case of low spin Fe^{III} ions and it was found that the spin sum rule does not hold because of intermixing between L_2 and L_3 edges. The XMCD investigation of the photomagnetic dinuclear complexes confirmed the metal-to-metal electron transfer. This XMCD investigation of the smallest unit of Fe/Co PBA family is helpful to understand the magnetic properties of the family of Fe/Co PBA. The XMCD study at Fe and Co K edges of a tridimensional RbCoFe PBA proved the existence of an antiferromagnetic interaction between Fe and Co metal ions in the photoinduced state.

Keywords:

Prussian Blue Analgues, Photomagnetism, Fe, Co, XAS, XMCD, $L_{2,3}$ edges, K edges.

Table of contents

Introduction

The family of the Fe/Co Prussian Blue Analogues (PBA) is well known for their bistable physical properties that are triggered and tuned by external stimuli such as light, temperature or pressure. The reversibility of the photo-induced and thermal-induced magnetization makes Fe/Co Prussian Blue Analogues a potential candidate for high density information storage devices. Since the discovery of photomagnetism in Fe/Co PBA, many efforts have been devoted towards the understanding of their interesting bistable properties. Among others, one of the important step in this direction is to study the electronic and magnetic structures of the corresponding precursors. This thesis aims to investigate the electronic and magnetic structure of two different photomagnetic Fe/Co dinuclear complexes, of a tridimensional RbCoFe PBA and of the corresponding Fe-bearing precursors. The manuscript is structured as follows:

Chapter 1 is a brief introduction to photomagnetic Fe/Co Prussian Blue Analogues.

Chapter 2 is dedicated to the experimental and theoretical techniques that were employed for the investigation of the Fe/Co PBA systems. X-ray Absorption spectroscopy (XAS) and X-ray magnetic circular dichroism (XMCD) are combined with Ligand Field Multiplet (LFM) theory to get information about the electronic and magnetic structures of the absorbing atoms.

Chapter 3 deals with the study of Fe-bearing precursors of Fe/Co PBA which includes the Potassium Ferricyanide precursor for tridimensional PBA crystals and FepzTp, FeTp*, FeTp that are the precursors for the cube, the square and the dinuclear molecular complexes respectively. A detailed XMCD investigation on Fe $L_{2,3}$ edges of FeTp precursor is presented. Ligand Field Multiplet calculations have been performed to extract orbit and spin magnetic moments and a value of the orbit magnetic moment larger than the spin magnetic moment is measured along the C_3 axis. Magneto-optical sum rules were applied and tested on Fe^{III}_{LS} bearing **FeTp** precursor. A thorough examination of the LFM results showed that the spin sum rule fails and a systematic study is performed to find out the origin of the failure for Fe^{III}_{LS} system. The results are published in a recently accepted paper.

Chapter 4 is dedicated to the XMCD investigations of two photomagnetic dinuclear Fe/Co PBA complexes, which are the smallest building block of the Fe/Co PBA family. The first dinuclear complex exhibits magnetic and optical bistability in solid state when solvent molecules are evaporated. The metal-to-metal electron transfer (ET) is confirmed by K and $L_{2,3}$ edges XMCD. Most of the results concerning this dinuclear complex are gathered in a paper to be submitted soon. The second dinuclear complex requires its

solvent molecules to display the ET properties. Hence, it is investigated at Fe and Co K edges in an experimental cell preserving from evaporation and the ET is also observed with temperature and light irradiation.

Chapter 5 presents the $L_{2,3}$ edges XMCD results in $Rb_2Co_4[Fe(CN)_6]_{3.3}{\cdot}11H_2O$ tridimensional PBA. The antiferromagnetic coupling between Fe and Co ions is observed in the photo-induced state. This finding is presented in a paper to be submitted.

Chapter 1

Photomagnetism in Molecule-Based Magnets: The Fe/Co Prussian Blue Family

1.1 Introduction

The field of molecular magnetism offers a dynamic range of molecular magnetic materials which are designed from pre-defined molecular precursors using a rational building block approach. The current challenge is to tailor properties of molecular complexes using state-of-the-art techniques to build smart materials. The manipulation of properties of magnetic materials at the nanoscale is an interdisciplinary research field at the crossroad of chemistry, physics and material science. In the last two decades, this field has grown regarding the design and the characterization of materials with novel functionalities. These molecular clusters which have been widely studied include spin cross over (SCO),[1,2] single molecule magnets (SMM)[3–5] and photomagnetic systems.[1,6–8] These molecular magnetic systems offer promising applications based on their multiple bistabilities and structure-based multifunctionalities.[5,8–10]

The study of photomagnetism and related phenomena in molecular systems is appealing because of their technological applications related to externally controlled magnetization.[9,10] Magnetic molecules can act as switches and thus can be used as molecular bits.[11] In this regard, the first example of photo-induced switching of magnetization in molecular species was reported in a Fe^{II} spin-crossover system by the Mainz group in 1984.[1] Spin-crossover is the spin state switching mechanism from low spin (LS) to high spin (HS) triggered by external parameters such as temperature, pressure, light irradiation and magnetic field.[2] In consequence, light-induced excited spin state trapping (LIESST) effect can be observed. An excited HS state is trapped when the energy barrier between the ground state and the excited state prevents the system to go back to the ground state.

In the following a brief overview of photomagnetic Fe/Co Prussian blue analogues is presented to help readers to understand the results described in the next chapters.

1.2 Photomagnetism in metal-to-metal electron transfer systems: Fe/Co Prussian Blue Analogues

Prussian Blue Analogues (PBA) are a prominent class of transition metal cyanide-based systems where the functionality of cyanido ligand is used to build molecular complexes. The cyanido ligand is a non-symmetric bridging molecule, and gives molecular complexes with strong metal–carbon bonds.[12] They are probably the oldest studied family of coordination compounds that has gained recognition for being the prototype of molecular magnets. The Prussian Blue family is widely known for its electronic and magnetic properties. The Prussian Blue can be identified as $Fe_4[Fe(CN)_6]_3$. The intense and characteristic blue color of the Prussian Blue pigment is attributed to the metal-to-metal electron transfer band around 700 nm due to the weak electron delocalization between metallic centres through the cyanide bridge.[13] The general formula of PBA can be written as $A_xM_y[M'(CN)_6]\cdot nH_2O$ where M and M' are transition metal ions, for instance, M = Co, M' = Fe, and A is an alkali metal cation (K^+, Rb^+, Na^+, Cs^+) randomly located in the structure. This coordination network has a face-centered cubic (fcc) structure with $Fm\bar{3}m$ space group and a cell parameter close to 10 Å.[6,14,15] In the schematic representation of tridimensional PBA in Figure 1.1, the metallic centres are connected by cyanide bridges, where Fe^{III} and Co^{II} are bonded to carbon and nitrogen respectively. In 1996, reversible photo-induced magnetism was discovered in $K_{0.2}Co_{1.4}[Fe(CN)_6]\cdot 6.9H_2O$ PBA by Sato *et al.*[6,16] Upon light irradiation at low temperature, diamagnetic Fe^{II}_{LS} (t^6_{2g} e^0_g, S=0)–CN–Co^{III}_{LS} (t^6_{2g} e^0_g, S=0) state is transformed into paramagnetic Fe^{III}_{LS} (t^5_{2g} e^0_g, S=1/2)–CN–Co^{II}_{HS} (t^5_{2g} e^2_g, S=3/2) state. The family of Prussian Blue Analogues offers multi-functional applications based on tunable physical properties.[9,10] These bistable physical properties are triggered and tuned by an external stimuli like light,[6,7,9,17] temperature,[18] electric field,[19] and pressure.[20] The metal-to-metal electron transfer (Figure 1.2) accompanies modification in the electronic structure of the Co centre (HS or LS) also referred as charge-transfer-induced spin transition (CTIST).[18] This metal-to-metal electron transfer is confirmed by infrared (IR),[7] Mössbauer[7] and X-ray absorption near edge structure (XANES) spectroscopies.[21]

A systematic study has been carried out by Sato *et al.*[7] and Verdaguer and co-workers[14,22–25] to investigate the driving factors of photo-induced magnetization in tridimensional Fe/Co PBA. Sato *et al.*[7] performed a study where potassium was replaced by rubidium to have $Rb_{0.66}Co_{1.25}[Fe(CN)_6]\cdot 4.3H_2O$. This compound was characterized by infrared and Mössbauer spectroscopies to understand the photo-induced long-range magnetic order and results were compared with the alkali free PBA. $Co_{1.5}[Fe(CN)_6]\cdot 6H_2O$ is an alkali free compound which served as a model system to look for the effects induced by alkali metal ions. Upon comparison, $Rb_{0.66}Co_{1.25}[Fe(CN)_6]\cdot 4.3H_2O$ was mainly composed of Fe^{II}_{LS}–CN–Co^{III}_{LS} diamagnetic species whereas $Co_{1.5}[Fe(CN)_6]\cdot 6H_2O$ contained paramagnetic Fe^{III}_{LS}–CN–Co^{II}_{HS} species at 5 K. This is attributed to the difference in average coordination sphere of Co in both compounds. The Co/Fe ratio is different in both compounds and this is responsible for the existence of $[Fe(CN)_6]$ vacancies in $Rb_{0.66}Co_{1.25}[Fe(CN)_6]\cdot 4.3H_2O$.

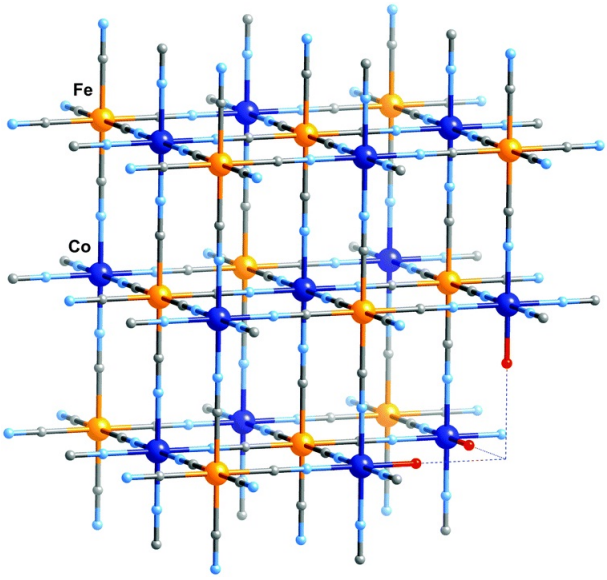

Figure 1.1 – Schematic representation of a Fe/Co Prussian blue network with formula $A_xCo_y[Fe(CN)_6]\cdot nH_2O$ (A: alkaline ions, which have been omitted for clarity; C: grey; N: light blue; Co: blue; Fe: yellow; O: red.This figure is taken from the review by Aguilà *et al.*[9]

The ligand field of nitrogen atoms from cyanido ligand is higher than for an oxygen atom in water molecule. Since, nitrogen atoms from cyanide bond are missing to make Co–NC bond, the ligand field around Co is modified. The ligand field around the Co ions plays a key role in stabilizing the Fe^{II}_{LS}–CN–Co^{III}_{LS} configuration or the other Fe^{III}_{LS}–CN–Co^{II}_{HS}. A series of Na^+ based Fe/Co PBA has also been synthesized where the CTIST temperature was found to vary by controlling the composition Co/Fe ratio. The Co/Fe ratio thus determines the strength of ligand field around Co^{II} ions.[18]

Sato *et al.*[7] and Verdaguer *et al.*[14,26–29] reported that the ground state of the Fe/Co Prussian Blue analogues depends on the type of the interstitial alkali cation. They also studied the effect of different Co environments on the photomagnetic properties. The different environments correspond to different amount of vacancies introduced in the structure. In conclusion, the photomagnetic properties are affected by the chemical composition such as the nature and the amount of alkali metal ion (0 to 4) per unit cell, the $[Fe(CN)_6]^{3-}$ vacancies and the zeolitic water molecules. In the metastable state (i.e. Fe^{III}_{LS}–CN–Co^{II}_{HS}), the framework is stabilized by strong cooperativity effects of the extended lattice as well as structural defects, features that are considered to be prerequisite for trapping the photo-induced species.

In addition, the structural information is significant to understand the fascinating photomagnetic properties in PBA. Extended X-ray absorption fine structure (EXAFS) results have shown that the major structural modifications occur in the vicinity of the Co ion: the Co–N bond length increases by 0.18 Å during the Co^{III}_{LS} to Co^{II}_{HS} spin transition.[30] This transition is isostructural with a change in the unit cell volume.[31] The structural changes were further investigated and characterized by X-ray absorption spectroscopy (XAS) at the metal $L_{2,3}$ edges combined with Ligand Field Multiplet Theory.[25,26,32,33] Thanks to the chemical selectivity of XAS, valuable information on each of the two metallic ions in cyanide based systems (A–CN–B) can be extracted such as oxidation

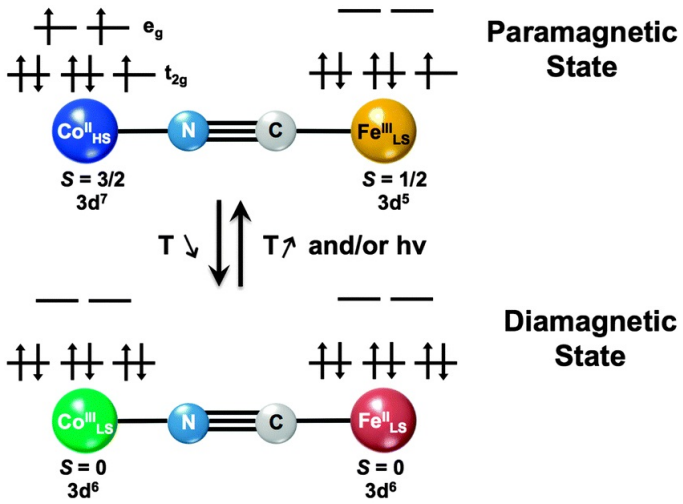

Figure 1.2 – Interconversion between the paramagnetic (Fe^{III}_{LS}–CN–Co^{II}_{HS}) and diamagnetic (Fe^{II}_{LS}–CN–Co^{III}_{LS}) electronic configurations due to thermally and photo-induced metal-to-metal electron transfer processes. This figure is taken from the review by Aguilà *et al.* [9]

state, spin state, local site symmetry. XAS and XMCD spectra can be simulated using Ligand Field Multiplet calculations to obtain the crystal field parameters. Arrio *et al.* [34] characterized the chemical bonds in hexacyanochromate(III) based system of Prussian Blue Analogues having Cr^{III}–CN–A^{II} units (A^{II} = V^{II}, Mn^{II}, Fe^{II}, Co^{II}, or Ni^{II}). The ferro- or ferrimagnetic ordering occurs below critical temperatures that ranges from 66 to 315 K. [35] The comparison of A^{II}–NC and Cr^{III}–CN bonds gives that the A^{II}—NC bond experiences small ligand-metal charge transfer. The LFM calculations show similar results for all four divalent A^{II} ions. In addition, by simulating the XAS and XMCD signals by LFM the orbit and spin magnetic moments of the ground state can be extracted. [36]

The first experimental determination of the Co crystal field parameters in a photomagnetic PBA was reported by Escax *et al.* [25] The spectral signatures for Co^{III}_{LS} and Co^{II}_{HS} ions were found to be characteristic of Co ion in octahedral symmetry. In 2006, Hocking *et al.* [37] performed a detailed investigation of $K_3[Fe^{III}(CN)_6]$ and $K_4[Fe^{II}(CN)_6]$ by LFM calculations. This study helped to understand the role of **Potassium Ferricyanide** as a percursor and to explain the origin of various features on Fe^{III}_{LS} $L_{2,3}$ edges XAS spectrum. Moreover, LFM calculations performed with configuration interaction confirm that X-ray absorption spectroscopy is a direct probe of metal-to-ligand back-bonding. Cafun *et al.* [33] performed the LFM calculations of the Co $L_{2,3}$ edges XAS spectra for the low temperature diamagnetic state and the photo-induced state in three different systems with Na, Rb and Cs alkali ions. They extracted the crystal field value for Co. The 10Dq(Co) was found to be 2.4 eV before irradiation (Fe^{II}_{HS}–CN–Co^{III}_{LS}) and 1.1 eV after irradiation (Fe^{III}_{LS}–CN–Co^{II}_{HS}).

1.3 Towards molecular analogues of Fe/Co PBA

In tridimensional PBA, the quantity and amount of alkali metal ions modify the amount of vacancies. The vacancies influence the environment around the Co ions and the coordination sphere that is completed by water molecules, hence altering the electron transfer properties. The vacancies are difficult to control since they are inhomogeneously inserted in the

structure. This results in the presence of inactive diamagnetic or paramagnetic pairs.[9] For technological applications, the electron transfer properties of tridimensional PBA systems must be transferred to their low-dimensional analogues. Some attempts have been made to develop Fe/Co cyanide complexes but thermal- and/or photo-induced electron transfer properties could not be observed.[38–40] The first evidence of thermally induced metal-to-metal electron transfer was reported in cyanido-bridged Fe/Co pentanuclear $[Fe_2Co_3]$ molecule by Dunbar and co-workers in 2004.[41,42]

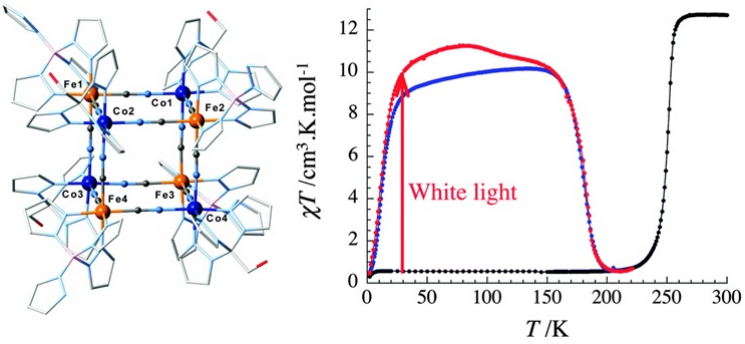

Figure 1.3 – (left) Schematic representation of the molecular structure of the cube analogue $[(pzTp)Fe^{III}(CN)_3]_4[Co^{II}(pz)_3CCH_2OH]_4{\cdot}13DMF{\cdot}4H_2O$ at 260 K (the core $[Co_4Fe_4]$ is emphasized). Lattice solvent molecules, anions, and hydrogen atoms are omitted for clarity. Fe, Co, N, C, O and B atoms are indicated in orange, dark blue, light blue, light grey, red and pink, respectively. (right) Temperature dependence of the χT product at 0.4 K/min for $[Co_4Fe_4]$ before (black dots), after irradiation (red dots); and after thermal quenching (blue dots). This figure is taken from the review by Aguilà *et al.*[9,43]

The group of chemists, C. Mathonière, R. Clérac and co-workers at Bordeaux succeeded in synthesizing the molecular cube and square analogues of tridimensional PBAs with electron transfer properties. The reversible photo-induced electron transfer in molecular cube $[Fe_4Co_4]$ was reported by Li *et al.*[43] This complex is the first molecular system that mimics the optical and magnetic bistability in Co/Fe Prussian Blue complexes. The molecular structure of the cube analogue is presented in Figure 1.3. In this molecular system the photo-induced state obtained by light irradiation or rapid cooling was found to have higher lifetime compared to the tridimensional networks. For Na^+ based PBA the metastable life time was 3 hours at 120 K[44] whereas it was 10 years at 120 K for the molecular cube.[45] In 2010, another discrete molecular system, a cyano-bridged $[Fe_2Co_2]$ square complex (Figure 1.4) was synthesized and characterized by Zhang *et al.*[45,46] In addition, Siretanu *et al.*[47] showed that the magnetic properties of molecular square complexes in solutions and particularly the electron-transfer temperature can be modulated by the nature of the solvent. The thermally induced switchable behavior, as was observed in the solid state for square molecules, had been transferred to diluted solutions. Later in 2012, Hashino *et al.* reported electron transfer properties in [CoFe] chain induced by light or temperature.[48]

Recently, thermal- and photo-induced electron transfer have been demonstrated in the smallest unit of the Fe/Co PBA family by Koumousi *et al.*[49] The molecular structure of the dinuclear complex is presented in Figure 4.1. In this dinuclear complex, the thermal-induced electron transfer is observed at 170 K with a thermal hysteresis of 5 K. At 10 K

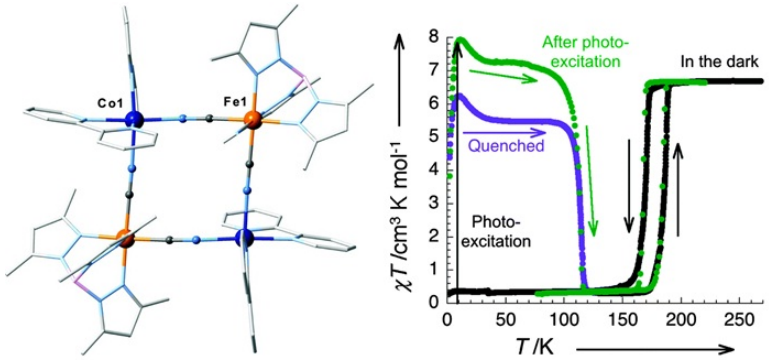

Figure 1.4 – (left) Schematic representation of molecular structure of the square analogue $[(Tp^*)Fe(CN)_3]_2[Co^{II}(bipy)_2]_2.[(OTf)]_2 \cdot 4DMF \cdot 2H_2O$ at $T = 230$ K (the core $[Co_2Fe_2]$ is emphasized). Lattice solvent molecules, anions, and hydrogen atoms are omitted for clarity. Fe, Co, N, C, O and B atoms are indicated in orange, dark blue, light blue, light grey, red and pink, respectively. (right) Temperature dependence of the χT product at 0.4 K/min for $[Co_2Fe_2]$ before (black dots), after irradiation (green dots); and after thermal quenching (purple dots). This figure is taken from the review by Aguilà *et al.*[9,45]

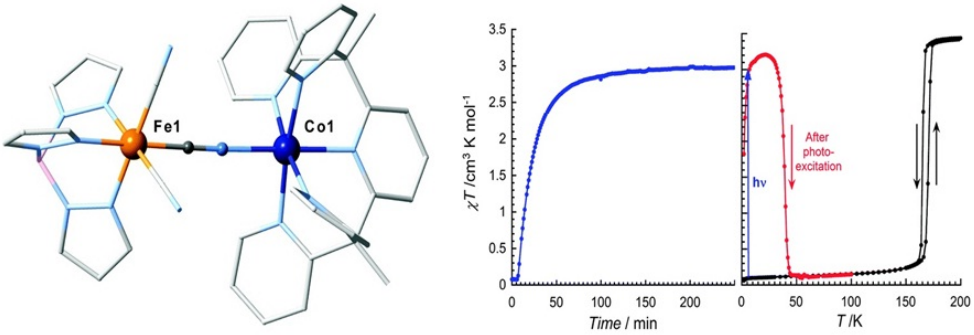

Figure 1.5 – Representation of the molecular structure of the dinuclear complex $[(Tp)Fe(CN)_3Co(PY5Me_2)](OTf) \cdot 2DMF$ at $T = 180$ K (left). Hydrogen atoms, triflate and lattice-solvent molecules are omitted for clarity. Fe,Co, N and C atoms are indicated in orange, dark blue, light blue and light grey, respectively. χT versus time (blue circles) of the desolvated compound, at 1 T and 10 K under white light irradiation (3 mW cm^{-2}) and temperature before (black dots) and after (red dots) white light irradiation with a sweep rate of 0.4 K/min (right). This figure is taken from the review by Aguilà *et al.*[9,49]

under white light irradiation photoconversion occurs. The metastable state of this complex relaxes to the diamagnetic state around 45 K. The miniaturization of molecular species tends to decrease the relaxation temperature which is particularly low in this complex.[9,49]

1.4 Summary of Chapter 1

It is desirable to understand the physical properties of nanostructures of Fe/Co PBA using XAS and XMCD techniques. The XMCD technique is proved to be essential for characterization and determination of the electronic and magnetic structures of molecule based magnets.[34,50–56] Some XAS and/or XMCD measurements have been reported on Fe/Co chain[57] and Fe/Co molecular square.[58,59] In collaboration with Prof. Corine Mathonière and Dr. Rodolph Clérac and their teams, the XAS and XMCD experiments have been performed on two dinuclear complexes and Fe-bearing precursors. In case of the dinuclear complexes, the switching mechanism of the local magnetization is observed. The XMCD results on Fe-bearing precursors and dinuclear complexes are presented in

Chapter 3 and Chapter 4. In a second part, a tridimensional PBA system has been studied in collaboration with Prof. Anne Bleuzen's group at ICMMO. The XMCD at $L_{2,3}$ edges is performed in $Rb_2Co_4[Fe(CN)_6]_{3.3}\cdot 11H_2O$ PBA system. The K edge XMCD results have already confirmed the antiferromagnetic coupling in photo-induced state of this PBA system.[51] In the present study, this antiferromagnetic interaction between Fe and Co is observed by recording XMCD signals at $L_{2,3}$ edges. The results are detailed in Chapter 5.

Chapter 2

Experimental Methods to study Fe/Co Prussian Analogues

2.1 Introduction

This chapter is a brief introduction to the experimental techniques which are employed to study the electronic and magnetic structure of the FeCo Prussian Blue systems in this work. The X-ray absorption spectroscopy (XAS) and X-ray magnetic circular dichroism (XMCD) are element specific techniques to study the local structure, spin, oxidation state and site-symmetry. In the case of coordination complexes, XAS and XMCD have been valuable in determining the details of the electronic and magnetic structures in nanoparticles, molecular materials and single molecule magnets.[50,52,53,56] The XMCD is the difference of two X-ray absorption spectra recorded with left and right circular polarized X-rays. XMCD probes the magnetic moment of individual atoms thanks to the chemical and orbital selectivity of X-ray absorption and can separate the orbit and spin contributions to the total magnetic moment of the absorbing atom.

2.2 XAS and XMCD

2.2.1 X-ray absorption spectroscopy

The X-ray sources from synchrotron radiation are highly intense, tunable and with well defined polarization state. The energy of X-ray photons ranges from few hundreds eV to several tens keV. XAS is a core level spectroscopy that is element specific and is considered as surface sensitive technique in the soft X-ray range (300 to 3000 eV) due to the detection mode that is usually the Total Electron Yield. The chemical sensitivity of XAS is obtained by tuning the incident X-ray photon energy to the core to valence transition energy of a specific element. When the electromagnetic radiation with photon energy E interacts with matter its intensity I as a function of penetration depth d is reduced in result of interaction with matter. The Beer-Lambert law is given as:

$$I(E,d) = I_0(E)\exp^{-\mu(E)d}$$

where μ(E) is the linear photoabsorption coefficient of the sample, $I_0(E)$ is the incident intensity and I is the intensity measured after absorption, behind the sample. At low energy of X-rays, the media are generally not transparent so that the absorption coefficient is not directly measured in the transmission mode and one has to detect a phenomenon that is expected to be proportional to the absorption coefficient. For energies below 20 keV, photoelectric effect is the dominant process compared to both elastic Rayleigh scattering and inelastic Compton scattering.[60] When a X-ray photon with energy $E = \hbar\omega$ is absorbed, a core-level electron with E_i binding energy in the initial state $|i\rangle$ is excited to an empty level $|f\rangle$ above the Fermi level with energy $E_f = E_i + E$. Therefore, XAS probes the empty states of the absorbing atom. The X-ray absorption cross-section is defined as the number of photons absorbed per atom divided by the number of incident photons per unit area and hence the dimension [length^2/atom].[61] The photoabsorption coefficient is proportional to absorption cross section.

In the electric dipole approximation the interaction Hamiltonian writes $\hat{\varepsilon} \cdot \vec{r}$ and the transition probability per unit time is given by the Fermi Golden rule:

$$\sigma(\hbar\omega) = 4\pi^2\alpha\hbar\omega \sum_{i,f} \frac{1}{d_i} |\langle f|\hat{\varepsilon} \cdot \vec{r}|i\rangle|^2 \delta(E_f - E_i - \hbar\omega). \tag{2.1}$$

In Equation 1.1, α is the fine structure constant, $\hbar\omega$ is the photon energy, $|i\rangle$ and $|f\rangle$ are multielectronic wavefunctions for the initial and the final configurations, d_i is the degeneracy of the multielectronic ground state, $\hat{\varepsilon}$ is the photon polarization vector, $\vec{r}$ is the integration variable, E_i and E_f are the energies associated to wavefunctions, $\delta(E_f - E_i - \hbar\omega)$ is the Dirac distribution that ensures energy conservation and the sum $\sum_{i,f}$ extends over all the populated terms of the initial state and all the terms of the final state configuration. The set-up for XAS experiments is illustrated in Figure 2.1.

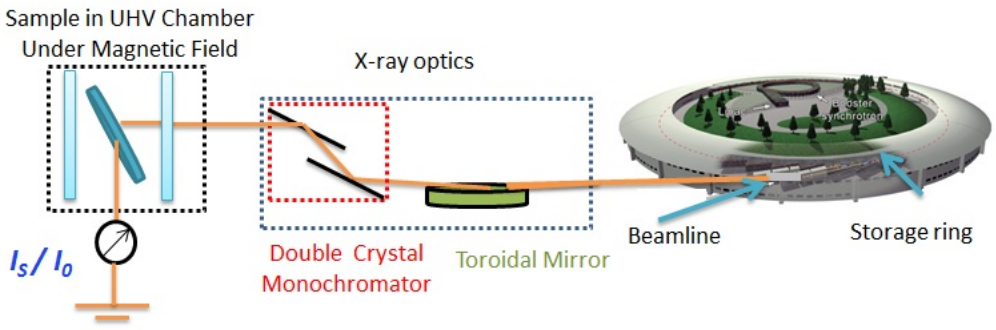

Figure 2.1 – Principle of X-ray absorption spectroscopy (XAS)

When the X-ray energy is close to the binding energy of a core-level, a sharp variation of the absorption coefficient is observed as a function of the X-ray energy, that is called an absorption edge. The characteristic edge jumps are the result of the consecutive excitation of core levels. Core level binding energies are specific for each atom and the absorption edges are labelled as K, L_1, $L_{2,3}$, M_1, $M_{2,3}$, or $M_{4,5}$ edges when the core level is present in the $|1s\rangle$, $|2s\rangle$, $|2p\rangle$, $|3s\rangle$, $|3p\rangle$, or $|3d\rangle$ respectively. The transition matrix elements

$|\langle f|\hat{\varepsilon}\cdot\vec{r}|i\rangle|^2$ characterize the absorption coefficient if initial and final states are properly described. The well localized core level states are atomic-like in character. But the final state description is in general difficult. In photoabsorption, effects such as chemical shift, splitting due to spin-orbit coupling, multiplet interactions due to Coulomb repulsions occur and leave their signatures on the XAS spectrum. Thus, valuable information about the electronic and magnetic structures or the site-symmetry can be extracted from XAS.

Selection rules

In XAS, the electric dipole selection rules only permit transitions where the angular momentum quantum number l changes by unity $\Delta l = \pm 1$ and conserve the spin $\Delta s = 0$. In addition to the selection rules involving l, other selection rules involve the magnetic quantum number m. For linear polarized light the selection rule is $\Delta m_l = 0$, for left circularly polarized light it is $\Delta m_l = +1$, and for right circularly polarized light it is $\Delta m_l = -1$.

In addition for the electric quadrupole transitions, the selection rules writes $\Delta l = \pm 2$ or $\Delta l = 0$. For $3d$ transition elements, the electric quadrupole transitions are negligible at $L_{2,3}$ edges and often detectable at K edges although they are found between 10 and 100 times weaker than the electric dipole transitions. [61]

In the electric dipole approximation, the isotropic absorption is the average of absorption measured for the three directions perpendicular to the polarization. The polarization vectors $\hat{\boldsymbol{\varepsilon}}^-$, $\hat{\boldsymbol{\varepsilon}}^+$ and $\hat{\boldsymbol{\varepsilon}}^{||}$ are orthogonal and defined as (to some phase conventions),

$$\hat{\boldsymbol{\varepsilon}}^- = -\frac{1}{\sqrt{2}}(\hat{\mathbf{e}}_x - i\hat{\mathbf{e}}_y)$$

$$\hat{\boldsymbol{\varepsilon}}^+ = -\frac{1}{\sqrt{2}}(\hat{\mathbf{e}}_x + i\hat{\mathbf{e}}_y)$$

$$\hat{\boldsymbol{\varepsilon}}^{||} = \hat{\mathbf{e}}_z$$

Then:

$$\sigma_{\text{iso}} = \frac{1}{3}(\sigma^+ + \sigma^- + \sigma^{||})$$

2.2.2 X-ray magnetic circular dichroism (XMCD)

Dichroism refers to the polarization dependent absorption of a material and is the manifestation that the optical response of a material depends upon the relative orientation of the polarization direction of light with respect to the symmetry axes of the material. It arises due to the charge or spin anisotropy in the system. The charge anisotropy (crystal field) causes the 'natural dichroism' like X-ray natural linear dichroism (XNLD) and X-ray natural circular dichroism (XNCD) whereas, X-ray magnetic linear dichroism (XMLD) and X-ray magnetic circular dichroism (XMCD) occur due to the anisotropy of

spin distribution.[60] When a sample carries a net magnetic moment, the system is no more invariant by time reversal so that the absorption with left polarized X-rays is no more equal to the absorption with right polarized X-rays: this is the origin of XMCD. XMCD effect was predicted theoretically in 1975 by Erskin and Stern and observed experimentally at Fe K edge in a Fe foil by Schütz *et al.*[62] At $L_{2,3}$ edges, a strong XMCD effect was first reported in ferromagnetic nickel by Chen *et al.*,[63]. The effect was ≈2 orders of magnitude larger than those at the K edges of transition metals.[62] The principle of XMCD measurements is illustrated in Figure 2.2. The quantization axis is defined in the $\hat{z}$ direction that is usually the direction of the wave vector of the incident beam. When necessary, a magnetic induction is applied along $\hat{z}$ to induce a net magnetic moment in the sample. The XMCD signal is the difference $\Delta\sigma$ between the two absorption cross sections for left and right polarized X-ray beam defined as,

$$\Delta\sigma = \sigma^{-}(B) - \sigma^{+}(B) = \sigma_{right}(B) - \sigma_{left}(B),$$

when **B** is parallel to the propagation vector **k**.

The signs "+" or "−" in σ^{+} and σ^{-} refer to X-ray helicity with "+" for left and "−" for right polarized X-rays.

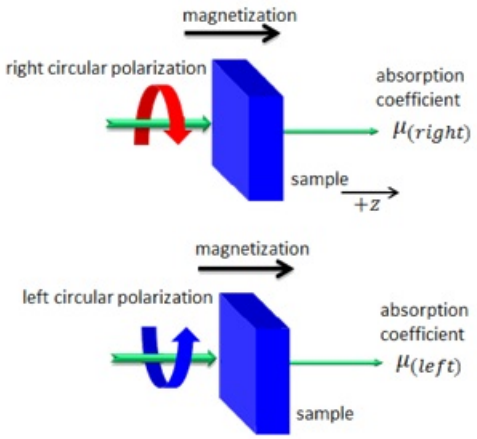

Figure 2.2 – Principle of X-ray Magnetic Circular Dichroism (XMCD)

The XMCD signal can be obtained either by taking the difference of two XAS spectra measured for two different circular polarization state (right and left) at a given magnetic induction direction or by keeping the circular polarization state of incoming X-rays fixed and then take the difference of two XAS spectra with two magnetic induction directions parallel and antiparallel to the propagation vector. The XMCD signals thus obtained in both cases remain equivalent. In this case it is useful to express XMCD signal in another notation such as σ^{ab}. In this notation, the superscript **a** represents the polarization state of the incoming X-ray beam and **b** represents the direction of the applied magnetic induction **B** with respect to the propagation vector **k** of the incoming X-ray beam. Then, **a** = ↓ (↑) for right (left) circular polarization and **b** = ↑ (↓) for magnetic induction **B** parallel (antiparallel) to **k**. The equivalence between the inversion of polarization state or magnetic induction **B** direction is only fully valid in the electric dipole approximation and allows to write:

$$\sigma^- = \sigma^{\uparrow\downarrow} = \sigma^{\downarrow\uparrow} \text{ and } \sigma^+ = \sigma^{\uparrow\uparrow} = \sigma^{\downarrow\downarrow}$$

The absorption cross section for a right circularly polarized beam and for a magnetic induction **B** applied parallel (or antiparallel) to the propagation vector **k** is labelled $\sigma^{\downarrow\uparrow}$ (or $\sigma^{\downarrow\downarrow}$ respectively). Similarly, for left circularly polarized beam the corresponding absorption cross sections are represented by $\sigma^{\uparrow\uparrow}$ or $\sigma^{\uparrow\downarrow}$ respectively for **B** and **k** in parallel or antiparallel configuration. If all types of measurements can be performed, the XMCD signal is obtained by $\sigma_{\text{XMCD}} = \frac{(\sigma^{\uparrow\downarrow}+\sigma^{\downarrow\uparrow})}{2} - \frac{(\sigma^{\downarrow\downarrow}+\sigma^{\uparrow\uparrow})}{2}$. With these definitions, a negative XMCD signal at the L_3 edge of $3d$ transition elements corresponds to a magnetic moment pointing in the same direction as the external magnetic induction.

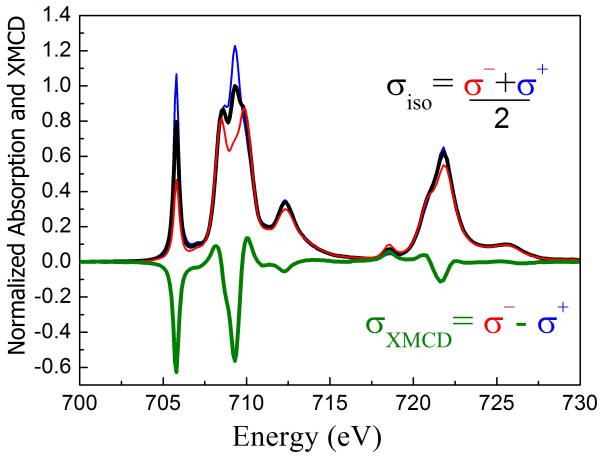

Figure 2.3 – Experimental XAS (black line) and XMCD (green line) at Fe $L_{2,3}$ edges is presented for illustration.

For powder samples with negligible XMLD, the equation $\sigma^+ + \sigma^- = 2\sigma^{||}$ holds and then the absorption cross section can be written as $\sigma_{\text{iso}} = \frac{\sigma^+ + \sigma^-}{2}$. The XAS and XMCD spectra at Fe $L_{2,3}$ edges are presented in Figure 2.3.

One of the important aspect of XMCD is the ability of measuring the element-specific magnetization curves. In this method, the intensity of dichroic signal is recorded by setting the monochromator at a given energy and the external magnetic induction is varied. When the XMCD signal is proportional to the magnetization of the absorbing atom, the XMCD detected magnetization curve is specific of the magnetization of the absorbing atom and can be compared to conventional magnetization curves such as those measured by SQUID or VSM magnetometers.

The review by Van der Laan *et al.*[64,65] summarizes the main applications in a variety of fields. XMCD is an excellent local probe which has been used to understand the switching mechanism, magnetic interactions and electronic structure of the metal in complexes.[50,51,66,67] Moreover, XMCD measurements under pressure have also been reported to study the structural distortions in these complexes.[68] Thanks to the magneto-optical sum rules applied to the XMCD spectra, spin and orbit contribution to the total magnetic moment can be separated and thus orbit and spin magnetic moments can be extracted. The sum rules were developed by B.T Thole, G. Van der Laan and P. Carra *et al.*[69,70] With $p = \int_{L_3}(\sigma^- - \sigma^+)dE$, $q = \int_{L_3+L_2}(\sigma^- - \sigma^+)dE$, and $r = \frac{1}{2}\int_{L_3+L_2}(\sigma^+ +$

$\sigma^-)dE$, the sum rules can be written as $\langle L_z \rangle = \frac{2}{3}\frac{q}{r}n_h$ and $\langle S_z \rangle + \frac{7}{2}\langle T_z \rangle = \frac{3p-2q}{2r}n_h$ where T_z is the magnetic dipole operator [70] along the $\hat{z}$ axis and n_h is the number of holes on the $3d$ shell. The integrals of XAS (r) and XMCD (p and q) are presented in figure 2.4. These sum rules relates the integral of XMCD at a specific edge to the ground state expectation values of orbit and spin magnetic moments. The sum rules are derived after several approximations. The energy dependency of the wave function in the matrix elements is not taken into account. Moreover, the L_3 and L_2 edges should be well separated to ensure correct integration on each edge. Hence, applicability of the sum rules on various systems requires great care. Some d states are present in the continuum and may also complicate the interpretation of the sum rules. The applicability of the magneto-optical sum rules is extensively addressed in the study of Fe^{III}_{LS} ion in **FeTp** in the next chapter.

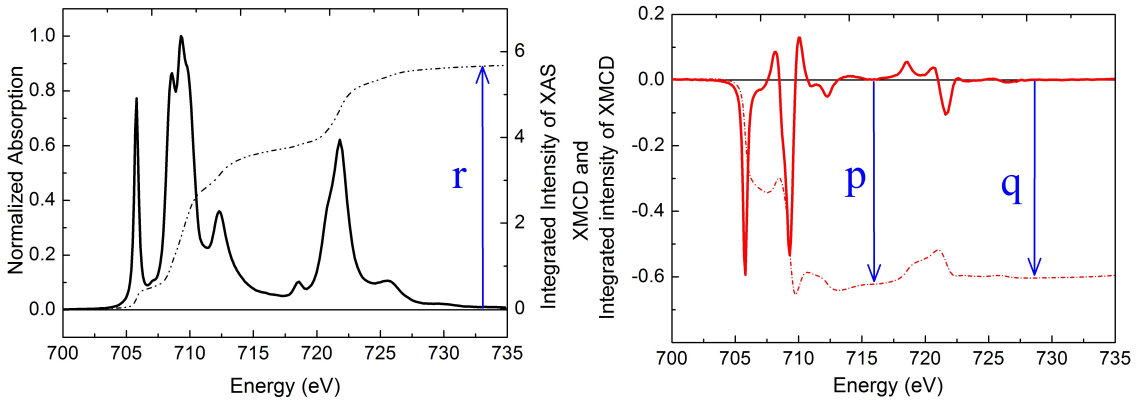

Figure 2.4 – Experimental XAS (black line), integrated intensity of XAS (black dashed line) (left) and XMCD (red line), integrated intensity of XMCD (red dashed line) (right) at Fe $L_{2,3}$ edges is presented for illustration.

Detection Methods

In the soft X-ray range the detection mode is the Total Electron Yield (TEY). TEY refers to the current of secondary electrons emitted as a consequence of the absorption of an X-ray photon. In this work absorption spectra are recorded with TEY by means of sample current measurements. The total electron yield is proportional to the absorption coefficient as long as the escape depth λ_{e^-} of the electron is much smaller compared to absorption length $1/\mu(E)$.[71,72] In the soft X-ray range, one can safely say that $\lambda_{e^-} \leq 5$ nm whereas $1/\mu(E) \geq 500$ nm.

For hard X-rays (i.e. Fe and Co K edges), the XAS spectra have been recorded by Total Fluorescence Yield (TFY). TFY is easier to measure than the transmitted flux that relies mainly on the sample thickness and homogeneity of the sample. Unfortunately, TFY is often damaged by the so-called reabsorption effects that have then to be corrected. In the present case of FeCo PBA, the Fe and Co concentrations are low enough to reduce the reabsorption effects to a minimum and it was found that it was not necessary to apply any correction.

2.3 Program TT-Multiplet

The details of the Ligand Field Multiplet calculations are given in next chapter. For in-depth understanding of the theoretical concepts of multiplet calculations, readers can consult *The hitchhiker's guide to multiplet calculations* by Gerrit van der Laan.[73]

The program RCN was written by Cowan.[74,75] This program utilizes the Hartree-Fock model to calculate the radial integrals for a given atomic configuration in a spherical Hamiltonian where kinetic energy, electron-nucleus Coulomb attraction, electron-electron Coulomb repulsions and spin-orbit coupling are present (see section Ligand Field Multiplet Calculations in Paper I). The outputs are the average energy of the electronic configuration, the Slater integrals associated to multielectronic Coulomb repulsions $F^k_{3d,3d}$, $F^k_{2d,3d}$, $G^k_{3d,2p}$ and the spin-orbit coupling terms ζ_{2p} and ζ_{3d}. The program TTRCG calculates all the matrix elements between the initial and the final state configurations calculated for a spherical Hamiltonian. Due to Wigner-Eckart theorem, the main calculation is the one associated to the reduced matrix elements. In program TTRAC the matrix elements are calculated for a symmetry lower than O(3). It is usually a point group symmetry that is consistent with the crystal-field symmetry, the presence of an external magnetic induction and a possible exchange magnetic field. When the matrix elements are known, the cross section is simply obtained by applying Equation 1.1. The program PLOTTER yields a spectrum by convoluting the sum of Dirac distribution by a Lorentzian function to account for the finite lifetime of the core-hole and by a Gaussian function to account for the instrumental resolution.

Chapter 3

Fe-bearing Precursors of Photomagnetic FeCo Prussian Blue Complexes

3.1 Introduction

In cyanometalate TM (TM : transition metal) complexes, cyanido ligand acts as strong mediator of magnetic coupling between the transition metal ions. These complexes are synthesized by pre-formed precursors using a building block approach. Cyanometalate precursors being the smallest units are likely to influence the magnetic, electronic and optical properties of cyanido-based molecular magnets such as Prussian Blue Analogues. In this chapter we present the study of the electronic structure of four Fe^{III}_{LS} bearing cyanometalate precursors that are used to synthesize the Fe/Co based PBA molecules. Most of the findings are obtained from XMCD measured at the Fe $L_{2,3}$ edges. Following are the chemical formulae of the four precursors :

$(NEt_4)[(Tp^*)Fe^{III}(CN)_3]$ (Tp*=tris(3,5-dimethyl)pyrazolyl borate) **FeTp***

$(NEt_4)[(pzTp)Fe^{III}(CN)_3]$, (pzTp = tetra-pyrazolyl borate) **FepzTp**

$(NBu_4)[(Tp)Fe^{III}(CN)_3]$ (Tp = hydridotris-pyrazolyl borate) **FeTp**

$K_3[(Fe^{III}(CN)_6]$ **Potassium hexacyanidoferrate(III)**

FeTp* [76,77] is the precursor for the square molecule,[45,46] **FepzTp**[78] is the precursor for the cube[43] and **FeTp** is the precursor used in the synthesis of the dinuclear Fe/Co PBA.[49] These samples were synthesized following the procedure developed by Li *et al.*,[43,77] Lescouëzec *et al.*[79] and Koumousi *et al.*[49] **Potassium hexacyanidoferrate(III)**[80,81] is the precursor for 3-dimensional bulk PBA systems discussed in the review by Aguilà *et al.*[9]

The structures of the four precursors are presented in Figure 3.1 and crystallographic data are presented in Table 3.1, as reported by Li *et al.*,[77,78] Jafri *et al.*[82] and Figgis.[81] In **FeTp**, **FeTp*** and **FepzTp**, Fe^{III} ions are connected to 3 cyanido ligands on one side and three Nitrogen atoms on the other side as shown in Figure 3.1. In these precursors the local point group symmetry around Fe ions is close to C_{3v}.[77,79] In **Potassium**

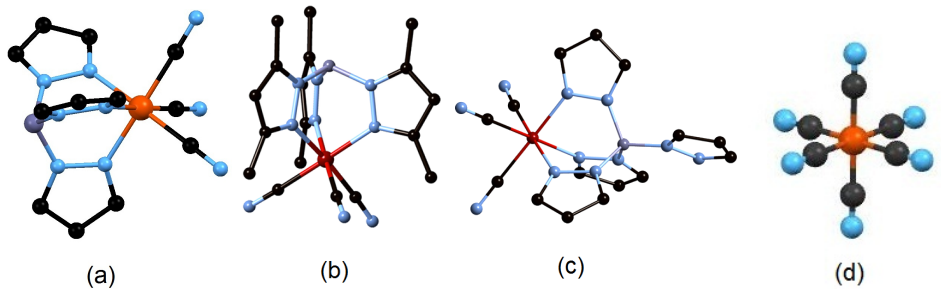

Figure 3.1 – Structure of the complex anions of (a) **FeTp** $[(Tp)Fe^{III}(CN)_3]^-$, (b) **FeTp*** $[(Tp^*)Fe^{III}(CN)_3]^-$, (c) **FepzTp** $[(pzTp)Fe^{III}(CN)_3]^-$ and (d) **Potassium hexacyanidoferrate(III)** $[Fe^{III}(CN)_6]^{3-}$. Color Scheme: Iron ions are drawn in red, Carbon atoms in black, Nitrogen atoms in blue and Boron atoms in grey. Hydrogen atoms and counterions (NBu_4^+, NEt_4^+, NEt_4^+ and K_3^+ respectively) are omitted for clarity.

hexacyanidoferrate(III), Fe^{III} ions are connected to the six cyanides forming a distorted octahedral coordination sphere.[83] When Fe^{III} ion is bonded to carbon atoms of the cyanido ligand this imposes a large π-back bonding in addition to σ bonding.[37] In case of **Potassium hexacyanidoferrate(III)** $K_3[(Fe^{III}(CN)_6]$, π-back bonding is larger than for the three other Fe precursors because of the six NC-Fe^{III} bonds. The σ bonding and π-back bonding are described as ligand-to-metal charge transfer (LMCT) and metal-to-ligand charge transfer (MLCT) respectively.

Compound	FeTp*	FepzTp	FeTp	Potassium hexacyanidoferrate(III)
Crystal system	trigonal	monoclinic	triclinic	monoclinic
Space group	$P3_1$	$P2_1/n$	$P\bar{1}$	$P2_1/c$
Temperature / K	90	90	120	295
a / Å	9.77400(10)	10.2580(2)	11.1956(4)	7.047
b / Å	9.77400(10)	15.2386(3)	11.2191(4)	10.4
c / Å	26.1990(4)	16.9912(4)	15.9740(6)	8.384
α / °	90.00	90.00	87.2840(10)	90
β / °	90.00	96.1396(7)	76.7360(10)	107.29
γ / °	120.00	90.00	60.8650(10)	90
Z	3	4	2	2

Table 3.1 – Crystallographic data of **FeTp***,[77] **FepzTp**,[78] **FeTp**[82] and **Potassium hexacyanidoferrate(III)**.[81]

The study of the precursors (which are non-photomagnetic systems) follows a methodological approach where the experimental spectra at the Fe $L_{2,3}$ edges are analyzed in order to yield valuable information concerning their impact on the properties exhibited by various photomagnetic Prussian Blue molecular magnets.

3.2 Paper I: Magnetic properties of the FeTp precursor

The precursor **FeTp** has been studied extensively. Theoretical and experimental details with the presentation of results on **FeTp** precursor can be found in the following paper that is printed in Section 3.2 with Supporting Information in Section 3.3. The paper has been accepted for publication in Inorganic Chemistry in June 2016.[82] (DOI: 10.1021/acs.inorgchem.6b00664)

Large orbital magnetic moment measured in the $[TpFe^{III}(CN)_3]^-$ precursor of photomagnetic molecular Prussian Blue Analogues

Sadaf Fatima Jafri,[†] Evangelia S. Koumousi,[‡,¶,§,‖] Philippe Sainctavit,[†,⊥] Amélie Juhin,[†] Vivien Schuler,[†] Oana Bunau,[†] Dmitri Mitcov,[§,‖] Pierre Dechambenoit,[§,‖] Corine Mathonière,[¶,‡] Rodolphe Clérac,[§,‖] Edwige Otero,[⊥] Philippe Ohresser,[⊥] Christophe Cartier dit Moulin,[#,@] and Marie-Anne Arrio*[,†]

†*Institut de Minéralogie, de Physique des Matériaux et de Cosmochimie, UMR7590, CNRS, UPMC, IRD, MNHN, 75252 Paris Cedex 05, France*

‡*CNRS, ICMCB, UPR 9048, F-33600, Pessac, France*

¶*Univ. Bordeaux, ICMCB, UPR 9048, F-33600, Pessac, France*

§*CNRS, CRPP, UPR 8641, F-33600, Pessac, France*

‖*Univ. Bordeaux, CRPP, UPR 8641, F-33600, Pessac, France*

⊥*Synchrotron SOLEIL, L'Orme des Merisiers Saint-Aubin, France*

#*CNRS, UMR 8232, Institut Parisien de Chimie Moléculaire, F-75005, Paris, France*

@*Sorbonne Universités, UPMC Univ Paris 06, UMR 8232, IPCM, F-75005, Paris, France.*

E-mail: marie-anne.arrio@impmc.upmc.fr

TOC figure

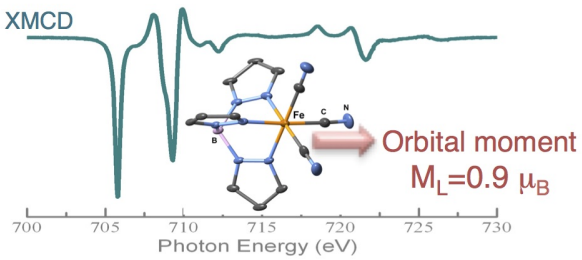

The **FeTp** ($(N(C_4H_9)_4[TpFe^{III}(CN)_3]$) complex is a precursor in the synthesis of recently reported photomagnetic cyanido-bridged Fe/Co complex. It was investigated by X-ray Magnetic Circular Dichroism measurements at the Fe $L_{2,3}$ edges, supported by Ligand Field Multiplet calculations, to determine the spin and orbit magnetic moments. The S=1/2 low spin state Fe^{III} ion is found to have an exceptionally large orbital magnetic moment (0.9 μ_B at $T = 2$ K and $B = 6.5$ T).

Abstract

Photomagnetism in three-dimensional Co/Fe Prussian Blue Analogues is a complex phenomenon, whose detailed mechanism is not yet fully understood. Recently, researchers have been able to prepare molecular fragments of these networks using a building block synthetic approach from mononuclear precursors. The main objective in this strategy is to isolate the smallest units that show an intramolecular electron transfer to have a better understanding of the electronic processes. A prior requirement to the development of this kind of system is to understand to what extent electronic and magnetic properties are inherited from the corresponding precursors. In this work, we investigate the electronic and magnetic properties of the **FeTp** precursor ($(N(C_4H_9)_4[TpFe^{III}(CN)_3]$), (Tp being tris-pyrazolyl borate) of a recently reported binuclear cyanido-bridged Fe/Co complex. X-ray Absorption Spectroscopy and X-ray Magnetic Circular Dichroism measurements at the Fe $L_{2,3}$ edges ($2p \rightarrow 3d$) supported by Ligand Field Multiplet calculations have allowed to determine the spin and orbit magnetic moments. Inaccuracy of the spin sum rule in the case of low spin Fe^{III} ion was demonstrated. An exceptionally large value of the orbital magnetic moment is found (0.9 μ_B at $T = 2$ K and $B = 6.5$ T) that is likely to play an important role in the magnetic and photomagnetic properties of molecular Fe/Co Prussian Blue Analogues.

3.2.1 Introduction

Molecule-based magnets, derived from three-dimensional (3D) Prussian Blue Analogues (PBA), are the topic of intensive research [35,84–86] since they are potential candidates for future molecular electronic devices [10,87–89] due to their tunable physical properties as a function of external stimuli such as magnetic field, light, pressure or temperature. [9,85,86] In this class of materials, cobalt ferricyanides are among the most well-known compounds exhibiting electron transfer switching induced by temperature and light. One of the most important aspects is their capability to act as photoswitches. [9,85,86] In 1996, the first evidence of photo-induced ferrimagnetism was reported by Hashimoto *et al.* [6] in a 3D network of PBA, $K_{0.2}Co_{1.4}[Fe(CN)_6]\cdot 6.9H_2O$, that crystallizes in a face-centered cubic

lattice. Upon irradiation with visible light ($\lambda = 660$ nm), an electron transfer converts diamagnetic Fe^{II}(d^6, low spin, $S = 0$)-CN-Co^{III}(d^6, low spin, $S = 0$) units into paramagnetic Fe^{III}(d^5, low spin, $S = 1/2$)-CN-Co^{II}(d^7, high spin, $S = 3/2$) units. In these systems, the photoinduced paramagnetic units in the 3D network after light irradiation led to the stabilization of a ferrimagnetic ground state with a Curie temperature of about 19 K.[6] Similar behavior has been also evidenced in other Co/Fe PBAs where the alkali metal ion has been substituted.[9] In one of these systems, $Rb_{1.8}Co_4[Fe(CN)_6]_{3.3}\cdot 13H_2O$, an X-ray Magnetic Circular Dichroism study has been performed in the photoexcited state and shows an antiparallel alignment of the Fe and Co sites confirming the photoinduced ferrimagnetic state.[51]

Whereas these tridimensional systems exhibit very interesting properties for technological applications, they contain many structural defects and are not soluble in common solvents. Consequently, they are difficult to manipulate and to shape for the future use. This drawback oriented research efforts to the synthesis of Prussian Blue molecular fragments that can be easily manipulated and studied. The design of soluble molecules that possess tunable magnetic, electrical and optical properties is based on the building block approach.[9,46] This synthetic path uses preformed precursors of the desired metal centers (Fe or Co) that are bearing at least one cyanido group and organic capping ligands. Indeed the redox properties of these precursors control the electron transfer behavior of the Prussian Blue molecules as recently demonstrated.[43] Therefore, a careful study of the precursors is required in order to design the electron transfer properties of the molecules. Recently, complexes with either a cubic octanuclear, a square tetranuclear, or a linear dinuclear shape have been synthesized,[9,11,43,45,46,49,77] and they have been found to exhibit thermally- and light-induced electron transfer at the molecular scale. This prompted us to carry out a detailed investigation of the Fe^{III} precursor used in the synthesis of the linear dinuclear Co ferricyanide PBA.[49] More precisely, this paper describes the mononuclear ($N(C_4H_9)_4[TpFe^{III}(CN)_3]$) complex, (Tp being tris-pyrazolyl borate; named hereafter **FeTp**). The molecular structure of this complex was determined by single-crystal X-ray crystallography (see Figure 3.2 and Supporting Information). Combined experimental and theoretical studies based on X-ray absorption spectroscopy (XAS) and X-ray magnetic circular dichroism (XMCD) were performed and allowed us to describe in detail the magnetic and electronic structures of the iron metal ion in this complex.

3.2.2 Experimental section

Sample was synthesized following the procedure described in work by Koumousi *et al.*[49] The crystal structure of **FeTp** at 120 K revealed an anionic mononuclear complex, where the Fe^{III} metal ion is in a meridional octahedral geometry formed by the tripodal Tp ligand and completed by three cyanido groups linked to the ion center by the C atoms (Figure 3.2). The negative charge of the complex is compensated by the $[N(C_4H_9)_4]^+$ cation (Supprting Information: Figure 3.6). The magnetic properties were investigated as a microcrystalline powder using a SQUID magnetometer with the field dependence of the magnetization (M) at different temperatures (from 1.85 to 8 K) and the thermal dependence of the χT

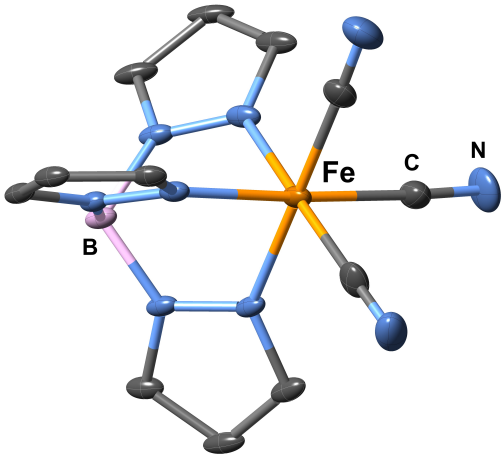

Figure 3.2 – ORTEP-type view of the anionic complex $(N(C_4H_9)_4)[TpFe^{III}(CN)_3]\cdot 3H_2O$ (**FeTp**) at 120 K. Thermal ellipsoids are depicted at the 50 % probability level. All anions, solvent molecules and hydrogen atoms are omitted for clarity. Fe, N, C and B atoms are indicated in orange, light blue, grey and pink, respectively.

product in the 1.85-300 K range (χ being the paramagnetic susceptibility and defined as M/B, B standing for the applied direct-currect (dc) field). The magnetic properties are shown in Supporting Information (SI: Figure 3.7). These magnetic measurements confirm the $S = 1/2$ ground state of the Fe^{III} center in **FeTp** with a g value of 2.37(5). The magnetization at 1.85 K does not saturate under the applied *dc* field up to 7 T (0.88 μ_B), indicating the presence of a strong magnetic anisotropy in the complex. At 6.5 T, the field used for the XMCD experiments, the magnetization reaches 0.86 μ_B.

XAS and XMCD spectra were recorded at the Fe $L_{2,3}$ edges on the soft X-ray beamline DEIMOS at SOLEIL synchrotron (France).[90] Circularly polarized photons delivered by an Apple II undulator were monochromatized by a plane grating monochromator working in the Petersen geometry. Samples were prepared by drop-casting on silicon wafers. All spectra were measured in total electron yield mode at $T = 2$ K and under ultra high vacuum (UHV) in the 1×10^{-10} mbar range.

The XMCD signal is defined as the difference between the XAS spectra measured with right and left circularly polarized X-rays. The XMCD signals were recorded by flipping both the circular polarization (either left or right helicity) and the external magnetic field (either $B^+ = +6.5$ T or $B^- = -6.5$ T). This method minimizes most of the spurious residual signals that might pollute the XMCD signal. The XMCD signal is obtained as the difference $\sigma_{XMCD} = \sigma^- - \sigma^+$ where $\sigma^- = (\sigma_L(B^-) + \sigma_R(B^+))/2$, $\sigma^+ = (\sigma_L(B^+) + \sigma_R(B^-))/2$, σ_L (σ_R) is the cross-section with left (right) polarized X-rays, and B^+ (B^-) the magnetic field parallel (antiparallel) to the X-ray propagation vector. With these definitions, a negative XMCD signal at the L_3 edge of $3d$ metals corresponds to a magnetic moment pointing in the same direction as the external magnetic field. The background is subtracted using two arctangent functions that model the $2p_{3/2} \rightarrow$ continuum and $2p_{1/2} \rightarrow$ continuum transitions following the method described by Chen *et al.*[91] The isotropic spectra are then normalized to 1 at the maximum of the L_3 edge so that comparison between experimental

and calculated spectra is straightforward.

The analysis of XAS and XMCD signals can either make use of the magneto-optical sum-rules developed by Thole and Carra [69,70] or be performed using Ligand Field Multiplet (LFM) calculations. For a magnetic field $\boldsymbol{B}$ along the $\hat{z}$ axis, the orbit and spin magnetic moments along $\hat{z}$ are related to the orbit and spin kinetic momentum operators by $m_{orbit} = -\langle L_z \rangle \mu_B$ and $m_{spin} = -g_o \langle S_z \rangle \mu_B = -2\langle S_z \rangle \mu_B$, where μ_B is positive and L_z and S_z are defined by $L_z = \hat{L}_z/\hbar$, $S_z = \hat{S}_z/\hbar$, where $\hat{L}_z$ and $\hat{S}_z$ are the z components of the orbital and spin kinetic momentum operators; $g_0 \approx 2$ is the electron Landé factor and $\langle O \rangle = \langle i|O|i \rangle$ is the expectation value of operator O (calculated over the ground state at 0 K, or its average calculated over all populated states at a finite temperature). With $p = \int_{L_3}(\sigma^- - \sigma^+)/(\hbar\omega)dE$, $q = \int_{L_3+L_2}(\sigma^- - \sigma^+)/(\hbar\omega)dE$, and $r = \frac{1}{2}\int_{L_3+L_2}(\sigma^+ + \sigma^-)/(\hbar\omega)dE$, the sum rules can be written as $\langle L_z \rangle = \frac{2}{3}\frac{q}{r} n_h$ and $\langle S_z \rangle + \frac{7}{2}\langle T_z \rangle = \frac{3p-2q}{2r} n_h$ where T_z is the magnetic dipole operator [70] along the $\hat{z}$ axis and n_h is the number of holes on the $3d$ shell. The effective spin kinetic momentum value is defined by $\langle S_z^{\text{eff}} \rangle = \langle S_z \rangle + \frac{7}{2}\langle T_z \rangle$. [92]

3.2.3 Ligand Field Multiplet (LFM) calculations

The detailed interpretation of XAS and XMCD spectra was achieved within the LFM theory, which is known to describe well the atomic-like ground and excited states, such as those involved in the XAS $L_{2,3}$ edges of $3d$ transition elements in iono-covalent compounds. LFM theory and its practical implementation for the calculation of XAS spectra are due to the pioneering work by Theo Thole, [93] based on atomic theory developed by Cowan [74] and the crystal field interactions (*i.e.*, symmetry) described by Butler. [94] In the electric dipole approximation, the absorption cross section is calculated according to the Fermi golden rule at 0 K:

$$\sigma(\hbar\omega) = 4\pi^2 \alpha \hbar\omega \sum_{i,f} \frac{1}{d_i} |\langle f|\hat{\varepsilon} \cdot \tilde{\mathbf{r}}|\mathbf{i}\rangle|^2 \delta(\mathbf{E_f} - \mathbf{E_i} - \hbar\omega), \tag{3.1}$$

where $|i\rangle$ and $|f\rangle$ are the many-body eigenfunctions associated to the ground state (with no core-hole) and to the final state (with a $2p$ core-hole in the present case), respectively. Many-body eigenfunctions $|i\rangle$ and $|f\rangle$, as well as the corresponding eigenvalues E_i and E_f, are determined from the exact diagonalization of an atomic, multielectronic, semi-empirical Hamiltonian. In the absence of magnetic field, the multielectronic ground state $|i\rangle$ is possibly degenerate (with d_i the degeneracy). The Hamiltonian describing the interaction between light and matter, $\hat{\boldsymbol{\varepsilon}} \cdot \vec{\mathbf{r}}$, is expressed in the electric dipole approximation, with $\hat{\boldsymbol{\varepsilon}}$ being the polarization vector, $\vec{\mathbf{r}}$ the position vector, $\hbar\omega$ the photon energy, and α the fine structure constant. The Dirac distribution $\delta(E_f - E_i - \hbar\omega)$ ensures the conservation of energy.

In the LFM approach, the spherical part of the atomic Hamiltonian takes into account the electron kinetic energy, the electron-nucleus Coulomb attractions, all the many-body electron-electron Coulomb repulsions between open shells, and the spin-orbit interaction on every shell of the absorbing ion. The geometrical environment of the absorbing atom is taken into account through the crystal field potential, *i.e.* an electrostatic field that obeys

the point group site symmetry of the absorbing atom.[94,95] Inter-electronic repulsions are taken into account by Slater integrals, F^2_{dd} and F^4_{dd} in the ground state, and F^2_{dd}, F^4_{dd}, F^2_{pd}, G^1_{pd}, and G^3_{pd} in the final state. Slater integrals are calculated in an atomic Hartree-Fock model and are scaled down by a reduction factor κ that reflects the electronic delocalization of the $3d$ electrons. The κ parameter follows the trends of the nephelauxetic series.[95] The atomic spin-orbit coupling parameters on the open shells are calculated through a spherical monoelectronic potential around the free ion. The symmetry for Fe^{III} metal ion in **FeTp** is very close to C_{3v}[79] so that the strength of the crystal field potential is parametrized by three independent parameters $10Dq$, $D\sigma$ and $D\tau$.[96] In the case of weakly covalent bond, the Fe^{III} ground state is described by only one configuration, $|i\rangle = |2p^6 3d^5\rangle$, and the corresponding excited state by $|f\rangle = |2p^5 3d^6\rangle$.[34] The chemical bond between a transition metal and a CN^- ligand is generally described in terms of σ donation between the occupied orbitals of the ligand and the unoccupied and partially occupied orbitals of the metal, and π back bonding between the occupied orbitals of the metal ion and the unoccupied orbitals of the ligand.[34,37] In the LFM model, several configurations are needed to account for these charge-transfers. The σ donation is modeled by the reduction in electron repulsion (κ) known as the nephelauxetic effect and by the ligand-to-metal charge transfer (LMCT) through the configuration interaction between $|2p^6 3d^5\rangle$ and $|2p^6 3d^6 \underline{L}\rangle$, where $\underline{L}$ stands for one hole in a ligand orbital. The π back bonding is modeled by the metal-to-ligand charge transfer (MLCT) through the configuration interaction between $|2p^6 3d^5\rangle$ and $|2p^6 3d^4 L^-\rangle$, where L^- stands for one additional electron on a ligand orbital. In Hocking *et al.*[37], the ground state of the $3d^5$ Fe^{III} ion was alternatively taken as a linear combination of the three configurations $|2p^6 3d^5\rangle$, $|2p^6 3d^4 L^-\rangle$ and $|2p^6 3d^6 \underline{L}\rangle$, while the final state was expressed as the linear combination of $|2p^5 3d^6\rangle$, $|2p^5 3d^5 L^-\rangle$ and $|2p^5 3d^7 \underline{L}\rangle$. Their results are excellent although not much better than ours (see Section Results), so that we preferred to stick to two configurations, which model only MLCT, therefore using a reduced number of parameters. In the present work, the ground state is expressed as a combination of $|2p^6 3d^5\rangle$ and $|2p^6 3d^4 L^-\rangle$, where the charge transfer energy Δ_i is the energy difference between both configurations. For the final state, the charge transfer energy Δ_f is the energy difference between $|2p^5 3d^6\rangle$ and $|2p^5 3d^5 L^-\rangle$. The strength of the charge transfer is represented in O_h symmetry by two ligand-metal charge transfer integrals V_{e_g} and $V_{t_{2g}}$, with $V = \langle 3d^5||H||3d^4 L^-\rangle$.

Once the $|i\rangle$ and $|f\rangle$ states have been calculated, the absolute intensities of the spectra are calculated in $Å^2$. At the $L_{2,3}$ edges, electric dipole allowed transitions from $2p$ to empty s levels have been calculated and found negligible. Consequently, they are not considered in the following. At a finite temperature, the population of the initial-state levels $|i\rangle$ is given by a Boltzmann law. The transition intensities are convoluted by a Lorentzian function (with $\gamma = 0.25$ eV at the L_3 edge and 0.5 eV at the L_2 edge) and a Gaussian function (with $\sigma = 0.1$ eV), which respectively take into account the lifetime of the Fe *2p* core-hole and the instrumental resolution.[37]

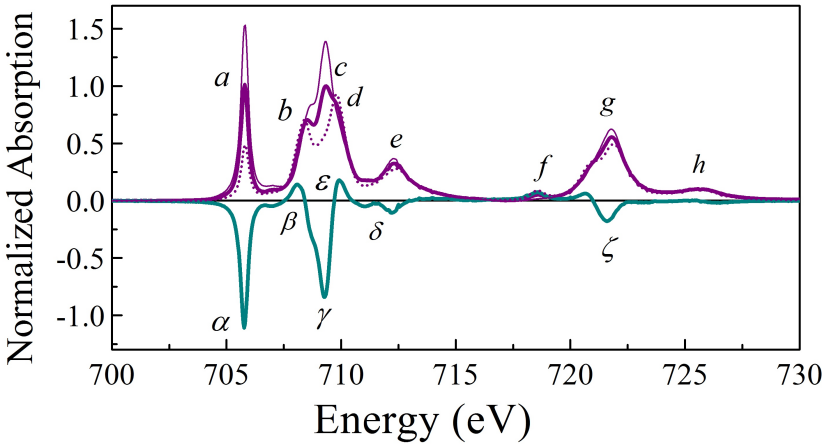

Figure 3.3 – Experimental isotropic XAS (thick purple line) and XMCD (cyan line) spectra for sample **FeTp** at ± 6.5 T and 2 K. XAS spectra with left (thin purple line) and right (dotted purple line) circular polarization are shown. XAS and XMCD signals are normalized to peak **c** of the isotropic XAS.

3.2.4 Results

The XAS and XMCD spectra measured for the **FeTp** complex are shown in Figure 3.3. The spectral shape is characteristic of low spin Fe^{III} ion and is similar to $K_3Fe(CN)_6$.[37,57] In particular, the peak **a** in the XAS spectrum is the electronic signature of a Fe^{III} ion surrounded by cyanido ligands. In a very simple purely atomic picture with no spin-orbit coupling and no distortion (O_h symmetry), peak **a** is attributed to the transition $2p^6t_{2g}^5 \rightarrow 2p^5t_{2g}^6$. Differences in the XAS intensity can be noticed for the two peaks (**b,c**) around 708.5eV and the big charge transfer feature (**e**) at 712.3 eV which could be related to the structural environment of Fe that is bound to three cyanido ligands in **FeTp** at the difference of $K_3Fe(CN)_6$ where Fe is surrounded by six cyanido ligands.[37] The intensity of the XMCD signal α for **FeTp** is close to 100 % of the normalized isotropic XAS, which is a strong indication that this sample has not suffered from the UHV conditions and that it contains only low spin Fe^{III} sites. This assumption is strongly supported by our LFM calculations, which are described in the next paragraph.

In order to extract electronic and magnetic information from the XAS and XMCD spectra, LFM calculations were performed for **FeTp**. As shown in Figure 3.4, the model, that provides the best agreement between the theoretical and experimental XAS and XMCD spectra (top panel), includes three theoretical key ingredients: the trigonal distortion of the Fe site (C_{3v} point group symmetry), the σ donation with 70 % of nephelauxetic reduction and the π back bonding (MLCT). The parameters used in the best simulation are given in Table 3.2. Parameters for all the calculations are given in Supporting Information (Table 3.5).

When the three ingredients are properly taken into account, the main features of the XAS spectrum are properly reproduced, *i.e.* the four main peaks at the L_3 edge (**a** : 705.8, **b** : 708.5, **c** : 709.3 and **e** : 712.3 eV), the small shoulder **d** at 709.8 eV, and the three peaks at the L_2 edge (**f** : 718.5, **g** : 721.8 and **h** : 725.8 eV). However although the intensity of most features are correctly simulated, the calculated intensity for the sharp peak **a** is largely underestimated. This feature might correspond to transitions with a longer lifetime

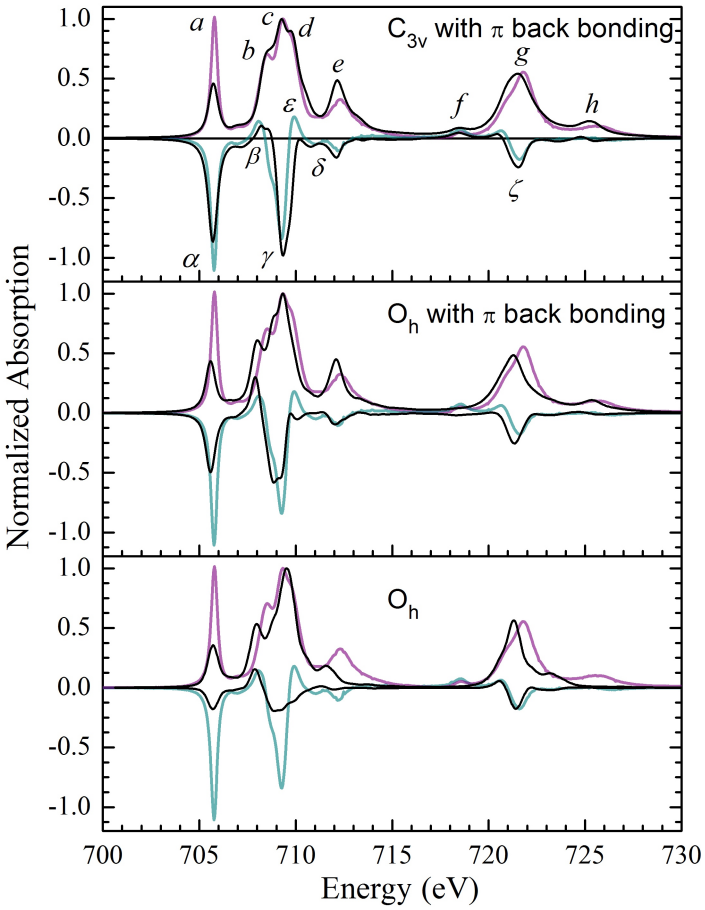

Figure 3.4 – Comparison of the normalized XAS (purple line) and XMCD (cyan line) experimental spectra, at ±6.5 T and 2 K, and calculated XAS and XMCD (thin black line) at the Fe $L_{2,3}$ edge for **FeTp**. Upper panel: calculations in C_{3v} with π back donation. Middle panel: calculation in O_h symmetry with π back donation. Lower panel: calculation in O_h symmetry without π back donation. All calculations include 70 % of nephelauxetic reduction. Isotropic XAS and XMCD are normalized to peak **c** of the isotropic XAS.

so that the constant Lorentzian broadening used at the L_3 edge is overestimated. The XMCD simulation is also quite good since all the experimental features are present in the calculation, with intensities that are fairly reproduced. The only slight discrepancy is found for the negative feature γ followed by the positive peak ϵ.

Table 3.2 – Parameters used in the Ligand Field Multiplet simulations for $B = 6.5$ T and $T = 2$ K. All energies are given in eV (1 eV corresponds to 11605 K), κ is dimensionless. The $3d$ and $2p$ spin-orbit coupling constants are the atomic values: $\zeta_{3d} = 0.059$ eV and $\zeta_{2p} = 8.199$ eV.

$10Dq$	$D\sigma$	$D\tau$	κ	Δ_i	Δ_f	V_{e_g}	$V_{t_{2g}}$
2.8	0.07	0.12	0.7	3.0	3.4	-0.8	1.8

3.2.5 Discussion

Since LFM simulations of the isotropic XAS and XMCD spectra yield a good agreement with the experiment, it is now possible to identify the role played by the various ingredients of the calculations, such as π back donation of the chemical bond around the Fe^{III} metal ion, and its local symmetry including possible distortions.

3.2.5.1 Influence of bond covalency and site symmetry

The lower panel of Figure 3.4 reports XAS and XMCD spectra calculated for a pure ionic model (single $|2p^6 3d^5\rangle$ configuration) in regular octahedral (O_h) symmetry, where the large crystal field ($10Dq = 2.8$ eV) and the nephelauxetic reduction ($\kappa = 70$ %) imposed by the cyanido ligands were taken into account, but not the associated π back bonding effect. In addition, the XAS and XMCD spectra calculated in O_h symmetry and including MLCT due to π back bonding are shown in the middle panel of Figure 3.4.

It is clear that the peak **e** cannot be properly reproduced unless π back bonding (MLCT) is taken into account using a configuration interaction. Also, the XMCD intensity is strongly reduced when the π back bonding is not taken into account. The energy difference between $|2p^6 3d^5\rangle$ and $|2p^6 3d^4 L^-\rangle$ configurations (Δ_i) used for MLCT was estimated from the energy difference measured on the experimental XAS spectrum between the main features **c** at the L_3 edge and the satellite peak **e** ($\Delta_i \approx 3.0$ eV). Note that in our calculation, LMCT was mimicked by simply using a nephelauxetic parameter $\kappa = 0.7$. Charge transfer parameters V_{eg} and V_{t2g} change only the shape of the peak **e**. It is well known that there is a large π back bonding between the iron metal ion and cyanido ligands[37], which implies that the π overlap integral has to be increased relative to the σ one in the model. Thus, the $|V_{t2g}/V_{eg}|$ ratio is larger than 2, like in $K_3Fe(CN)_6$.[37]

For the calculations performed in the O_h symmetry with MLCT, the peak **e** is well reproduced and small discrepancies in intensities are observed for the different peaks. The main missing feature is a small peak **f**, which is absent in both XAS and XMCD spectra. When the calculation is performed in C_{3v} symmetry (upper panel), the peak **f** is present in both XAS and XMCD signals. One can also notice that the intensity of the XMCD signal is reproduced at best for the calculation in C_{3v} symmetry with the external magnetic field set along the C_3 axis. From the previous discussion, we conclude that both π back bonding and C_{3v} symmetry are mandatory ingredients in the calculation to obtain a fair agreement with experiment.

3.2.5.2 Determination of expectation values from LFM calculations

From the LFM calculations, ground state expectation values $\langle O\rangle = \langle i|O|i\rangle$ can be directly computed for the orbital angular kinetic momentum L_z, the spin kinetic momentum S_z, the magnetic dipole T_z and n_h the number of holes on the $3d$ shell. The L_z, S_z, T_z expectation values for the different set of parameters (O_h, O_h with LMCT, C_{3v} and C_{3v} with LMCT) are given in Supporting Information (Table 3.6). Using the parameter set yielding the best agreement to experiment (Table 3.2), ground state expectation at T = 0 K are: $\langle L_z^{LFM}\rangle = -1.236$, $\langle S_z^{LFM}\rangle = -0.488$ and $\langle T_z^{LFM}\rangle = -0.115$. Since $\langle T_z\rangle$ is significantly different from zero, it has to be taken into account in the spin sum rule. Then, from the values of $\langle S_z\rangle$ and $\langle T_z\rangle$, one obtains the effective spin kinetic momentum $\langle S_z^{\text{eff}}\rangle = \langle S_z\rangle + \frac{7}{2}\langle T_z\rangle = -0.889$. At 0 K, the spin magnetic moment for the Fe ion is $m_{\text{spin}} = -2\langle S_z\rangle\mu_B = 0.98\mu_B$ as can be expected for an $S = 1/2$ low spin Fe^{III} ion and in agreement with the magnetic measurements (Supporting information Figure 3.7). The main new information is that the orbital magnetic moment is thus quite large with

$m_{\text{orbit}} = -\langle L_z \rangle \mu_B = 1.24 \mu_B$.

The LFM calculated ground state writes $\alpha|3d^5\rangle + \beta|3d^4 L^-\rangle$, with $\alpha^2 = 0.73$ and $\beta^2 = 0.27$ so that the effective electron number on the $3d$ shell is 4.73 and then $n_h = 10 - 4.73 = 5.27$ for the number of holes on the $3d$ shell. Thus, the π back bonding induces a strong reduction of the local electronic density (4.73 compared to 5 for a free Fe^{III} ion).

3.2.5.3 Application of magneto-optical sum rules to the LFM calculated spectra

The values of orbital and spin magnetic moments can also be determined by application of the magneto-optical sum rules.[69,70] In the case of highly covalent high spin Fe^{III} center, Piamonteze *et. al.* showed that the sum rule for the orbital magnetic moment is expected to be followed, but a systematic underestimation of $\langle S_z \rangle$ by 30% is expected from the spin sum rule.[92] However, Piamonteze and coworkers did not include neither the case of a low spin Fe^{III} center nor the case of a covalent Fe^{III} metal ion. The LFM calculations suppose that the radial integrals of the 3d orbitals and other radial integrals are energy independent. Several papers questionned whether this approximation might impair the application of the orbit sum rule to the K edges or $L_{2,3}$ edges of 3d transitions elements.[97–99] The generally excellent agreement observed between the experimental $L_{2,3}$ edges spectra for 3d transition metal ion and the spectra calculated in the LFM framework tend to indicate that the energy dependence of the radial integrals is expected to be highly negligible, at least for $L_{2,3}$ edges. The values extracted from the sum rules are reported in Table 3.3.

Table 3.3 – $\langle L_z \rangle$, $\langle S_z \rangle$, $\langle S_z^{\text{eff}} \rangle$ and $\langle T_z \rangle$ obtained from LFM calculations (expectation values obtained from the ground state calculation), from sum rules applied to LFM calculated spectra and from sum rules applied to the experimental spectra.

	LFM calculation		Experiment
	$\langle i\|O_z\|i\rangle^{(a)}$	sum rules	sum rules
$\langle L_z \rangle$	-1.236	-1.236	-0.88
$\langle S_z \rangle$	-0.488	-0.214^b	-0.17^b
$\langle S_z^{\text{eff}} \rangle$	-0.889	-0.615	-0.57
$\langle T_z \rangle$	-0.115	-	-

[a] Expectation values obtained from the ground state calculation at 0 K; [b] Using $\langle T_z \rangle$ obtained from the LFM calculation.

The sum rule for the orbital magnetic moment yields $\langle L_z \rangle = -1.2357$, which is very close to the value computed for the Fe^{III} ground state ($\langle L_z^{\text{LFM}} \rangle = -1.2361$), with a difference less than 0.02%. This confirms the fact that the orbital sum rule is valid even when configuration interaction is needed to give a proper description of the ground state.[100] On the contrary, the sum rule for the spin magnetic moment yields $\langle S_z^{\text{eff}} \rangle = -0.615$, which is very different from the value obtained from the LFM calculation (*i.e.* $\langle S_z^{\text{LFM,eff}} \rangle = -0.889$), with a corresponding deviation larger than 30%. From $\langle S_z^{\text{eff}} \rangle = -0.615$ and $\langle T_z \rangle = -0.115$, the sum rule yields $\langle S_z \rangle = -0.214$ ($m_{spin} = 0.43 \mu_B$) whereas the LFM calculation gives $\langle S_z^{LFM} \rangle = -0.488$ ($m_{spin} = 0.98 \mu_B$). The error on the estimation of the spin magnetic moment calculated from the spin sum rule is found to be close to 60%. In the next section, we investigate the origin of the spin sum rule breakdown.

3.2.5.4 Origin of the failure of the spin sum rule

The application of the spin sum rule requires a separated integration of the XMCD data at the L_3 edge on one hand, and at the L_2 edge on the other hand. Three main reasons could make such integrations unreliable: *(i)* the instrumental and intrinsic resolutions might broaden the L_3 or L_2 edges, *(ii)* the determination of the cutoff energy separating the L_3 edge from the L_2 edge might be not straightforward, and *(iii)* a large component of the $2p_{1/2}$ core-hole might be present in the L_3 edge as well as a large component of the $2p_{3/2}$ core-hole in the L_2 edge (*i.e.*, the so-called intermixing).
The influence of spectral resolution on the spin sum rule is detailed in the Supporting Information (Section 3.3.5) . It is found to be small. The error coming from the choice of the cutoff energy separating the L_3 edge from the L_2 edge is also small (see Supporting Information Section 3.3.5) and can not explain the inaccuracy of the spin sum rule.

Influence of $2p$ spin-orbit coupling

Finally, we questioned the possible intermixing of L_3 and L_2 edges. By definition, the L_3 edge should correspond to transitions where the final state is exclusively built from the $2p_{3/2}$ core-hole. Similarly, the L_2 edge should correspond to transitions where the final state is exclusively built from $2p_{1/2}$ core-hole. Intermixing means that in the L_3 edge region, there is a contribution from transitions built with a final state made of $2p_{1/2}$ core-hole and that in the L_2 edge region, there is a contribution from transitions built with a final state made of $2p_{3/2}$ core-hole. When such intermixing is present, the spin sum rule is expected to yield incorrect $\langle S_z^{\text{eff}} \rangle$ values.

The origin of intermixing resides in the ratio between the $2p$ core-hole spin-orbit coupling, ζ_{2p}, and the electron-electron Coulomb repulsions. The largest ζ_{2p}, the smallest the intermixing is. The impact of ζ_{2p} on the intermixing can be tested by increasing its value artificially in the LFM calculations. Note that, since ζ_{2p} is only present in the final state, ground state expectation values for $\langle L_z^{\text{LFM}} \rangle$, $\langle S_z^{\text{LFM}} \rangle$ and $\langle T_z^{\text{LFM}} \rangle$ are not modified when changing ζ_{2p}. On the contrary, ζ_{2p} strongly changes the splitting between the L_3 and L_2 edges since the splitting scales roughly as $\frac{3}{2}\zeta_{2p}$.

A series of theoretical XAS and XMCD spectra has been computed for different values of $2p$ spin-orbit coupling, starting from its atomic value ζ_{2p}^{Fe} (8.199 eV), and by increasing it to $2 \times \zeta_{2p}^{\text{Fe}}$, $4 \times \zeta_{2p}^{\text{Fe}}$, $8 \times \zeta_{2p}^{\text{Fe}}$, $10 \times \zeta_{2p}^{\text{Fe}}$, $12.5 \times \zeta_{2p}^{\text{Fe}}$ and finally $125 \times \zeta_{2p}^{\text{Fe}}$.

The spin sum rule was applied in order to estimate the $\langle S_z^{\text{eff}} \rangle$ value as a function of ζ_{2p}. The error computed as $\frac{\langle S_z^{\text{LFM}} \rangle - \langle S_z^{\text{eff}}(\zeta_{2p}) \rangle}{\langle S_z^{\text{eff,LFM}} \rangle}$ (where $\langle S_z^{\text{LFM,eff}} \rangle = -0.889$ is the expectation value determined previously) is reported in Figure 3.5. It is now very clear that the origin of the failure for the spin sum rule resides in the value of the $2p$ core-hole spin-orbit coupling, which is too small with respect to the energy splittings induced by the Coulomb repulsions and the configuration interaction. The error is larger than $\approx 3\%$ when the $2p$ spin-orbit coupling is $12.5 \times \zeta_{2p}^{\text{Fe}} \approx 100$ eV. For the spin sum rule to be satisfied (error less than 0.2%), the $2p$ spin-orbit coupling has to be as large as $125\ \zeta_{2p}^{\text{Fe}} \approx 1000$ eV.

To conclude, the spin sum rule fails because of large intermixing in the present case of

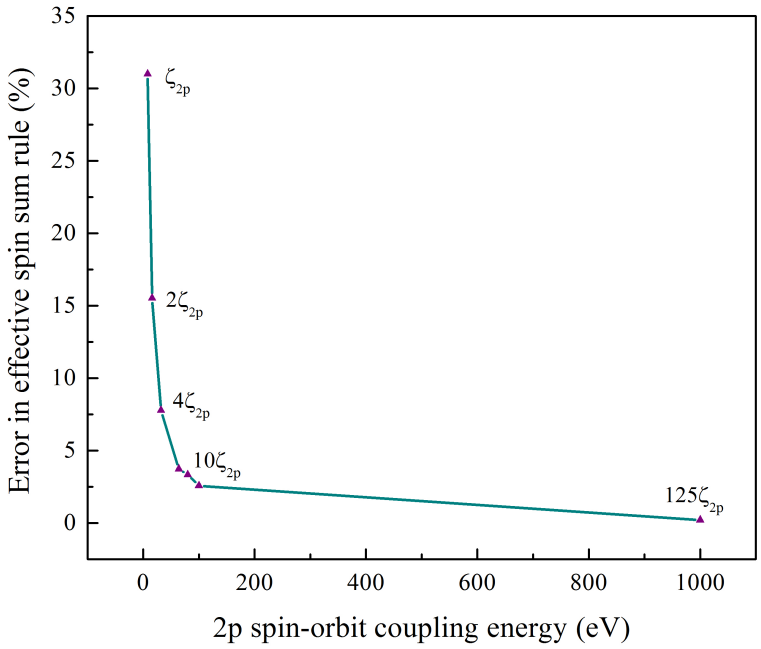

Figure 3.5 – Variation of error in the spin sum rule as a function of $2p$ spin-orbit coupling.

a low spin configuration for the Fe^{III} metal ion combined with the large crystal field and the large π back bonding of the cyanido ligands. This conclusion is also valid at finite temperatures. Indeed, by performing LFM calculations and applying the sum rules, we checked that whatever the temperature, the orbital sum rule is obeyed whereas the spin sum rule is not. The results are summarized in Table 3.7 of Supporting Information.

3.2.5.5 Application of the sum rule to the experimental spectra and comparison to the experimental magnetization data

As discussed previously, we can expect the orbital sum rule applied to the experimental spectra to yield a good estimate of the orbital magnetic moment. To do so, LFM calculations are essential since they provide the value of the effective number of holes (n_h) on the metal $3d$ shell. On the contrary, the spin sum rule can not provide a reliable value since it already fails when applied to the theoretical spectra. In addition, the determination of m_{spin} from the experimental spectra would require the knowledge of $\langle T_z \rangle$, which is unknown and very likely different from zero, as it found from the expectation value determined by LFM ($\langle T_z \rangle_{\text{LFM}} = -0.115$). One can then conclude that it is impossible to extract the spin magnetic moment from the spin sum rule applied to the experimental spectra for low spin Fe^{III} $L_{2,3}$ edges. Nevertheless, results of its application are presented in Table 3.3 for completeness.

Application of the orbital sum rule to the experimental spectra yields $\langle L_z \rangle = -0.88$ ($m_{\text{orbit}} = 0.88\mu_B$) with an usual estimated error of approximately 10%. The spin sum rule does not hold and we used the following strategy to determine the spin magnetic moment. We suppose that the ratio between the LFM values for $\langle L_z \rangle_{\text{LFM}}$ and $\langle S_z \rangle_{\text{LFM}}$ is the same

as the ratio of the experimental values for $\langle L_z \rangle_{\mathrm{Exp}}$ and $\langle S_z \rangle_{\mathrm{Exp}}$. Considering that $\langle L_z \rangle_{\mathrm{LFM}}$ and $\langle S_z \rangle_{\mathrm{LFM}}$ are given by the LFM calculation, and $\langle L_z \rangle_{\mathrm{Exp}}$ is determined by the sum rule for the orbital magnetic moment, $\langle S_z \rangle_{\mathrm{Exp}}$ is simply determined by Equation 3.2.

$$\langle S_z \rangle_{\mathrm{Exp}} = \langle S_z \rangle_{\mathrm{LFM}} \times \frac{\langle L_z \rangle_{\mathrm{Exp}}}{\langle L_z \rangle_{\mathrm{LFM}}} \tag{3.2}$$

Application of Eq. 3.2 yields $\langle S_z \rangle = -0.35$ ($m_{\mathrm{spin}} = 0.70\mu_B$) and a total magnetic moment $m_{\mathrm{total}} = 1.58\mu_B$. For the **FeTp** complex, the value of the orbital magnetic moment m_{orbit} is thus very large and slightly larger than m_{spin} ($m_{\mathrm{orbit}}/m_{\mathrm{spin}} > 1$). This is a quite unique situation, because the orbital magnetic moment is usually quenched for $3d$ transition ions and smaller than the spin magnetic moment. Our findings are in line with previous reports[101–104] that stated that the value of the orbital magnetic moment increases as the dimensionality of the system decreases, although the m_{orbit} values were always less than the m_{spin} values. Nevertheless Figgis predicted a high value of orbital magnetic moment for a low spin Fe^{III} ion in the $K_3Fe(CN)_6$ compound.[105] Moreover, Day and coworkers predicted that the orbital magnetic moment is 60% of the total magnetic moment in $Cs_2KFe(CN)_6$.[83] However, no direct measurement of m_{orbit} has been reported yet. In addition, magnetic measurements show that the value of the g factor deviates significantly from 2 which is consistent with a large value of the orbital magnetic moment. The XAS and XMCD measurements performed in this work give for the first time a direct measurement of m_{orbit} for a low spin Fe^{III} center and corroborate previous findings.

Nevertheless, the total magnetic moment deduced from the present XMCD investigation ($\approx 1.6\ \mu_B$) exceeds significantly the one deduced from the magnetization measurements ($0.86\ \mu_B$). In order to solve this apparent discrepancy, we investigated the theoretical angular dependence of the XMCD spectra and of the orbital and spin magnetic moments. Indeed, the magnetization data (Figure 3.7) have been recorded on a fully isotropic powder for which the sample grains are physically aleatory blocked in the measured sample at low temperature, while XMCD measurements were made on drop cast. The LFM calculations shown in Figure 3.4 were performed for an external magnetic field parallel to the C_3 axis of the molecule. We performed complementary calculations by varying the respective orientation of the magnetic field $\boldsymbol{B}$ and the C_3 axis. We found that the XMCD intensity as well as $\langle S_z \rangle$ and $\langle L_z \rangle$ are highly dependent on the α angle between $\boldsymbol{B}$ and the C_3 axis. In the local orthonormal frame where [001] is along the C_3 axis and [010] lies in one of the three σ_V planes, we tested the following orientations for $\boldsymbol{B}$ parallel to [001] ($\alpha = 0°$), [100] ($\alpha = 90°$), [010] ($\alpha = 90°$), [110] ($\alpha = 90°$), [011] ($\alpha = 45°$), [101] ($\alpha = 45°$) and [111] ($\alpha = 54.7°$). We found that $\langle L_z \rangle(\alpha) \approx \cos(\alpha) \times \langle L_z \rangle(0)$ and $\langle S_z \rangle(\alpha) \approx \cos(\alpha) \times \langle S_z \rangle(0)$ (see Table Table 3.8 in Supporting Information; note that z is the direction of $\boldsymbol{B}$ and $\langle O_z \rangle$ is the projection of the operator $\hat{O}$ on the z direction). Interestingly the averaged value for $\langle T_z \rangle(\alpha)$ does not follow the $\cos(\alpha)$ law as can be seen from Table 3.8. This is very likely because $\langle T_z \rangle(\alpha)$ is quadratic in the orbit kinetic momentum and linear in the spin kinetic momentum so that the angular dependence is more involved. One can notice that $\langle T_z \rangle$ remains small for all the calculated angles. The angular dependence for $\langle L_z \rangle$ and

$\langle S_z \rangle$ supports the fact that the C_3 axis is an easy axis of magnetization. The theoretical LFM values of $\langle L_z \rangle_{\mathrm{LFM}}$ and $\langle S_z \rangle_{\mathrm{LFM}}$ that would be expected for a fully disordered sample are therefore obtained by the angular spherical average, yielding respective values of $\frac{1}{2}\langle L_z \rangle_{\mathrm{LFM}}(0) = 0.618\ \mu_B$ and $\frac{1}{2}\langle S_z \rangle_{\mathrm{LFM}}(0) = 0.244\ \mu_B$ (see supporting information Section 3.3.6) and a total theoretical magnetic moment of 1.106 μ_B at 0 K. Remarkably, this value is fully compatible with the magnetization data (Figure 3.7). As mentioned previously, the XMCD measurements were performed on a dropcasted sample. The crystals show a needle-shaped morphology with the C_3 axis almost perpendicular to the needle axis.[106] When the ±6.5 T magnetic field is applied on such a sample, the crystallites for which the C_3 axis makes a large angle with respect to the $\boldsymbol{B}$ direction experience a torque, rotate along the needle axis and tend to orientate along the magnetic field direction so that the measured sample can be considered as partially oriented with the C_3 axis along the $\boldsymbol{B}$ direction. A simple analysis of the intensity of the experimental XMCD signal compared to its maximum calculated value along the ternary axis indicates that the C_3 axis of the measured crystallites are distributed inside a cone centered along the $\boldsymbol{B}$ direction and with a half angle at the summit of 65°. Hence the XMCD measurements were obviously performed on an oriented sample and this explains the larger experimental orbital and spin magnetic moments determined from XMCD with respect to the SQUID magnetization data.

3.2.6 Conclusion

The ground state electronic and magnetic properties of the Fe^{III} metal ion in the **FeTp** building block of the molecular Prussian Blue Analogues have been determined by measuring low temperature XAS and XMCD spectra at the Fe^{III} $L_{2,3}$ edges. As expected, it is found that the electronic structure is in agreement with a low spin Fe^{III} state and an effective electron number of 4.73 due to the π back bonding of the cyanido ligands. The inaccuracy of the spin sum rule has been demonstrated and its origin is found in the intermixing between L_3 and L_2 edges. This result completes the previous work from Piamonteze[92] and leads to the conclusion that the spin sum rule is inaccurate in the general case of Fe^{III} ion. In its ground state, the Fe^{III} ion carries an exceptionnally large orbital magnetic moment where $m_{\mathrm{orbit}}/m_{\mathrm{spin}}$ is slightly larger than 1. Along the magnetic easy axis, the orbital moment can be as large as 1.2 μ_B. Such a strong orbital moment is expected to significantly influence the magnetic properties of the compound. Indeed, spin-orbit coupling links the spin magnetic moment to the orbital part, which depends on the spatial organization around the ion. When the precursors are engaged in building Prussian Blue Analogues, the orbital magnetic moment couples efficiently to the crystallographic structure. Therefore, a change of valency and magnetism, such as observed for Fe^{III} ($S = 1/2$) to Fe^{II} ($S = 0$) transformation in Fe/Co cyanido bridged complexes exhibiting electron transfer, shall be accompanied by crystallographic relaxations, and therefore, the large orbital magnetic moment is likely to play a major role in the photoconversion mechanism.

In a next future, we will report the X-ray absorption and XMCD studies of Fe/Co photomagnetic molecular PBAs involving the **FeTp** precursor.

Acknowledgement

This work was supported by the Centre National de la Recherche Scientifique (CNRS, France), the Ministère de l'Enseignement Supérieur et de la Recherche (MESR, France), the Aquitaine region, the Institut Universitaire de France (IUF) and partially funded by ANR (ANR-10-BLAN-0712; ANR-09-BLAN-0175; ANR-12-PDOC-0038), and GDR MCM2. We thank SOLEIL staff for running the machines, Abhishake Mondal (CRPP) for helping with the **FeTp** crystallization, Lorenzo Paulatto and Alain Soyer (IMPMC) for computing support and Rodrigue Lescouëzec (IPCM) for fruitful discussion on magnetic anisotropies.

3.3 Supporting Information of Paper I

This section contains some technical information that we have been using for the understanding of the electronic and magnetic properties of **FeTp**. These are the crystallographic data of the **FeTp** complex, the magnetic susceptibility and magnetization measured by SQUID, the parameters used for the Ligand Field Multiplet calculations, a review of the validity of the spin sum rule and the analysis of the angular dependence of the orbit and spin magnetic moments extracted from LFM calculations.

3.3.1 Crystallographic data of the FeTp complex

Single crystal of $(N(C_4H_9)_4[(Tp)Fe^{III}(CN)_3]\cdot 3H_2O)$ (**FeTp**) was mounted in Cargille TM NHV immersion oil on a 50 mm MicroMountsTM rod at 120 K. The crystallographic data were collected with Bruker APEX II Quasar diffractometers, housed at the Institut de Chimie de la Matière Condensée de Bordeaux, and equipped with a graphite monochromator centered on the MoKα path. The program SAINT was used to integrate the data, which was thereafter corrected for absorption using SADABS.[107] The structure was solved by direct methods and refined by a full-matrix least-squares method on F^2 using SHELXL-2013.[108] All non-hydrogen atoms were refined anisotropically. Hydrogen atoms were assigned to ideal positions and refined isotropically using suitable riding models. Reflections were merged by SHELXL according to the crystal class for the calculation of statistics and refinement. Figures 3.6 was generated using CrystalMaker®(CrystalMaker Software Ltd, www.crystalmaker.com).

3.3.2 Magnetic data of the FeTp complex

Magnetic susceptibility measurements were performed on a Quantum Design SQUID magnetometer MPMS-XL housed at the Centre de Recherche Paul Pascal (Pessac) at temperatures between 1.85 and 300 K and dc magnetic fields ranging from -7 to 7 T. Microcrystalline powder of **FeTp** (13.24 mg) introduced in sealed polyethylene bag, which was containing 10.88 mg of paraton oil. Prior to the experiments, the field-dependent magnetization was measured at 100 K in order to detect the presence of any bulk ferromagnetic impurities. In fact, paramagnetic or diamagnetic materials should exhibit a perfectly linear dependence of the magnetization that extrapolates to zero at zero dc field. The sample appeared to be free of any significant ferromagnetic impurities. The magnetic data were corrected for the sample holder, paratone oil and the intrinsic diamagnetic contributions.

3.3.3 Experimental XAS : raw data and background subtraction

The baseline function (bl(E) with E the photon energy in eV) is a linear combination of two arctangent function to fit the absorption step edge at L_3 (711.4 eV) and L_2 (723.7 eV) edges:

$$bl(E) = \left[\{\frac{1}{\pi}\left(\arctan(Energy - 711.4) + \frac{\pi}{2}\right)\frac{2}{3}\} + \{\frac{1}{\pi}\left(\arctan(Energy - 723.7)\frac{\pi}{2}\right)\frac{1}{3}\}\right] * 0.044$$

After subtraction of the baseline, the XAS spectrum is normalized to 1 at peak **c** of the L_3 edge *i.e* is divided by the absorption value at the energy of peak **c**. The XMCD

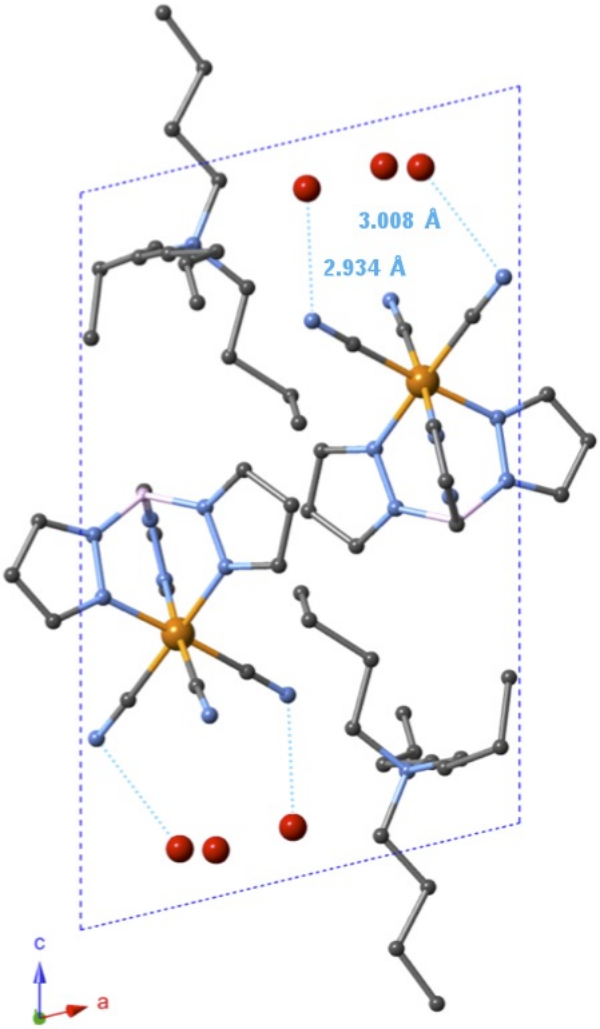

Figure 3.6 – Projection view of the crystal structure of **FeTp** at 120 K showing the packing of the anionic complexes, the $[N(C_4H_9)_4]^+$ cations and the lattice water molecules in the (ac) plane. All the hydrogen atoms are omited for clarity. Fe, N, C, O and B atoms are indicated in orange, light blue, grey, red and pink, respectively. The light blue dotted lines are indicating the H-bonding between the cyanide groups and the lattice water molecules.

spectrum is divided by the same value.

3.3.4 Parameters used for Ligand Field Multiplet calculations and L_z, S_z, T_z expectation values

The parameters used for Figure 3.4 are given in Table 3.5 and L_z, S_z, T_z expectation values for the three previous set of parameters are given in Table 3.6.

Compound	$(N(C_4H_9)_4)[(Tp)Fe^{III}(CN)_3]\cdot 3H_2O$
FW / g mol^{-1}	643.94
Crystal color	orange
Crystal system	triclinic
Space group	$P\bar{1}$
Temperature / K	120
a / Å	11.1956(4)
b / Å	11.2191(4)
c / Å	15.9740(6)
α / °	87.2840(10)
β / °	76.7360(10)
γ / °	60.8650(10)
V / Å^3	1700.91(11)
Z	2
$^aR_1(I > 2\sigma(I))$	0.0630
$^bwR_2$ (all data)	0.1801
R_{int}	0.0277
CCDC	1451192
$^aR_1 = \sum \lvert\lvert F_0\rvert - \lvert F_c\rvert\rvert / \sum \lvert F_0\rvert$, $^bwR_2 = [\sum(F_0^2 - F_c^2)^2 / \sum(F_0^2)^2]^{1/2}$	

Table 3.4 – Crystallographic data of **FeTp**.

	$10Dq$	$D\sigma$	$D\tau$	κ	Δ_i	Δ_f	V_{eg}	V_{t2g}	B
C_{3v} with MLCT	2.8	0.07	0.12	0.7	3.0	3.4	-0.8	1.8	6.5
C_{3v} no MLCT	2.8	0.07	0.12	0.7	-	-	-	-	6.5
O_h with MLCT	2.8	0	0	0.7	3.0	3.4	-0.8	1.8	6.5
O_h no MLCT	2.8	0	0	0.7	-	-	-	-	6.5

Table 3.5 – Parameters used in the Ligand Field Multiplet simulations. All the calculations were made with $\zeta_{3d} = 0.059$ eV, $\zeta_{2p} = 8.199$ eV (atomic values). κ is dimensionless, B is expressed in Tesla. The other parameters are given in eV.

	$\langle L_z \rangle$	$\langle S_z \rangle$	$\langle T_z \rangle$
C_{3v} with MLCT	-1.2361	-0.4882	-0.1146
C_{3v} no MLCT	-1.3941	-0.5012	-0.0924
O_h with MLCT	-0.7754	-0.1704	-0.0594
O_h no MLCT	-0.8521	-0.1786	-0.0523

Table 3.6 – Expectation values for the orbit magnetic moments, the spin magnetic moments and the magnetic dipole terms.

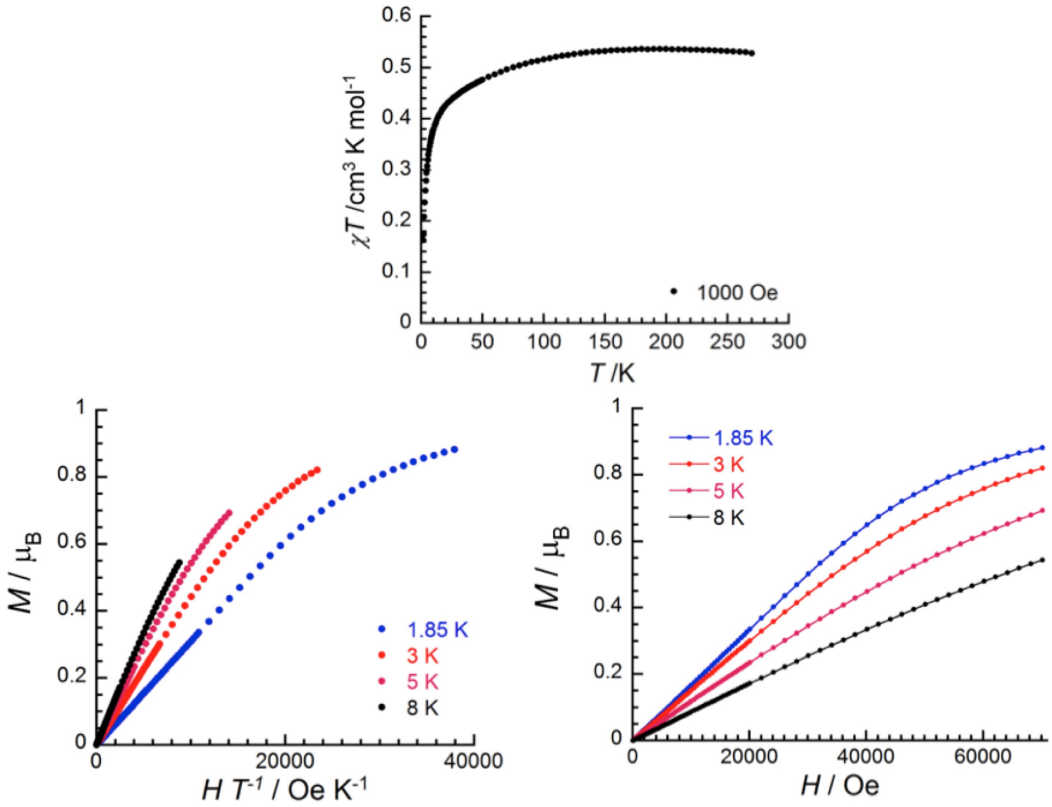

Figure 3.7 – (top) χT versus T curves at 0.1 T, (bottom right) reduced magnetization curve (M versus B/T), and (bottom left) magnetization versus field B for **FeTp** at different temperatures. χ is defined as the molar magnetic susceptibility and equal to M/B, M being the magnetization and B the *dc* applied magnetic field.

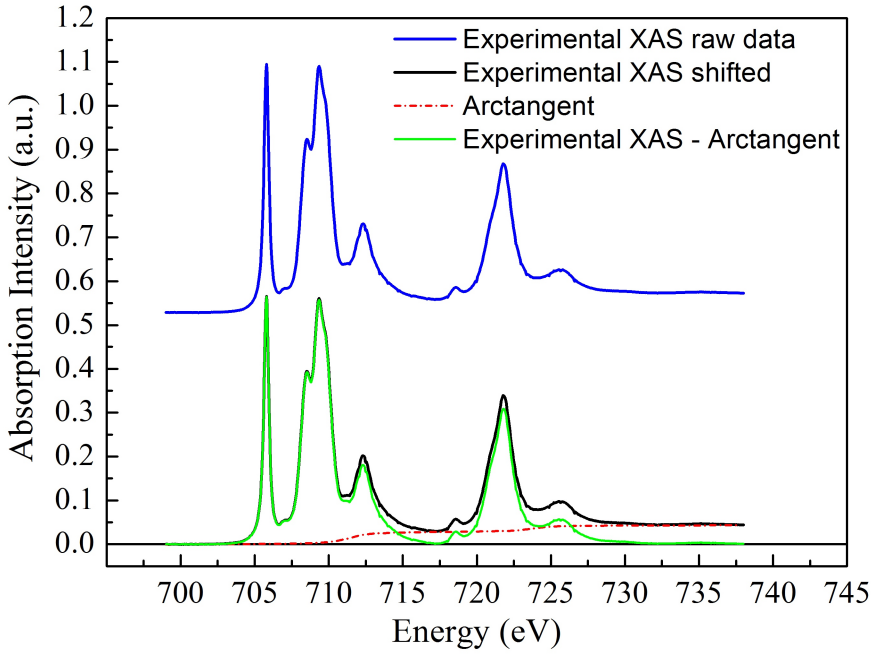

Figure 3.8 – Experimental XAS spectrum (blue line), XAS spectrum before the edge set to zero (black line), XAS spectrum after subtraction (green line) of the arctangent functions (dashed red line) for sample **FeTp** at 2 K.

3.3.5 Origin of the failure of the spin sum rule

Influence of spectral resolution

Instead of applying the sum rules to the convoluted calculated spectra, it can be applied to the calculated discrete transitions before applying any broadening function. By doing so, we discard the possible weight transfer between L_3 and L_2 edges induced by spectral broadening. With this approach, one obtains $\langle S_z^{\text{eff}} \rangle = -0.634$, which is indeed quite similar to the value obtained by the sum rule applied to the convoluted theoretical spectra. The deviation is still equal to 29% compared to the LFM value $\langle S_z^{\text{LFM,eff}} \rangle = -0.889$, so that the failure of the spin sum rule cannot fully be attributed to the spectral broadening.

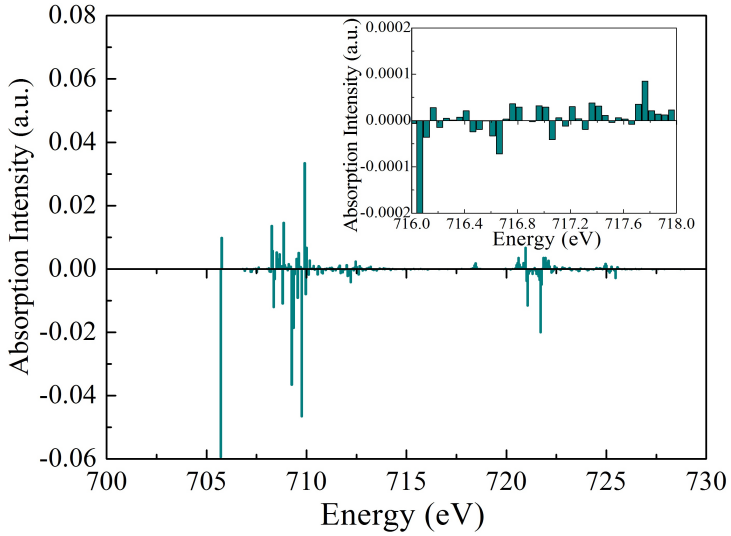

Figure 3.9 – Unconvoluted transition intensities (sticks : $|\langle f|\hat{\boldsymbol{\varepsilon}} \cdot \vec{\mathbf{r}}|i\rangle|^2$) for the XMCD spectrum calculated at $T = 0$ K using the parameters listed in Table 3.2 (main text). Insert : zoom of the region between L_3 and L_2 edges

Influence of cutoff energy between L_3 and L_2 edges

Another important aspect for the application of the spin sum rule is the choice of the cutoff energy that separates the XMCD signal into its contribution to the L_3 edge and to the L_2 edge. The value chosen here was 716.8 eV, although this choice is not straightforward because there are many transitions with non-zero amplitudes close to this energy (*i.e.*, 1000 times smaller than the largest transitions, see Figure 3.9). If the cutoff energy is varied between 715.8 and 717.8 eV, one finds that the effective spin $\langle S_z^{\text{eff}} \rangle$ changes by $\approx 1\%$. Hence, we can conclude that the cutoff energy cannot be the cause for the failure of the spin sum rule.

3.3.5.1 Influence of temperature

The calculation for $\langle L_z \rangle$, $\langle S_z \rangle$ and $\langle T_z \rangle$ have been performed at 0 K. For finite temperatures, we first calculated the thermal average values for $\langle L_z \rangle$, $\langle S_z \rangle$ and $\langle T_z \rangle$ which are given by the Boltzmann distribution at temperature T. For $\langle L_z \rangle$ it reads

$$\langle L_z \rangle(T) = \frac{\sum_{i=0}^{n} \langle i|L_z|i\rangle \exp[-(\frac{E_i - E_o}{kT})]}{\sum_{i=0}^{n} \exp[-(\frac{E_i - E_o}{kT})]} \tag{3.3}$$

where i is the index running on the initial states, E_i is the energy of the initial state i and the Boltzmann constant $k = 8.617 \times 10^{-5}$eV.K^{-1}. For $\langle S_z \rangle$ and $\langle T_z \rangle$, similar formula are applied. The values obtained from the calculations at 0 K, 2 K and 4 K are reported in Table 3.7. Whatever the temperature, the orbit sum rule is obeyed whereas the spin sum rule is not.

	LFM calculations			Sum rules: calculated Spectra			Sum rules: calculated sticks		
	0 K	2 K	4 K	0 K	2 K	4 K	0 K	2 K	4 K
$\langle L_z \rangle$	-1.2361	-1.2359	-1.2216	-1.2358	-1.2357	-1.2225	-1.2363	-1.2362	-1.2230
$\langle S_z \rangle$	-0.4882	-0.4881	-0.4825	-0.2135	-0.2136	-0.2117	-0.2319	-0.2318	-0.2295
$\langle S_z^{\text{eff}} \rangle$	-0.8894	-0.8893	-0.8791	-0.6149	-0.6149	-0.6083	-0.6331	-0.6330	-0.6261

Table 3.7 – Ground state average values of L_z, S_z and S_z^{eff} extracted from multiplet calculations and spin sum rules (on calculated spectra and sticks of calculated spectra) at 0 K, 2 K and 4 K for the atomic value of $2p$ spin-orbit coupling $\zeta_{2p} = 8.199$ eV.

3.3.6 Angular dependence of the orbit and spin magnetic moments and average values

3.3.6.1 Angular dependence

$[ijk]$	$\alpha(^\circ)$	$\langle S_z \rangle$	$\langle S_z \rangle (0) \times \cos(\alpha)$	$\langle L_z \rangle$	$\langle L_z \rangle (0) \times \cos(\alpha)$	$\langle T_z \rangle$
[001]	0	-0.4882	-0.4882	-1.2361	-1.2361	-0.1146
[100]	90	-0.0060	0.0	-0.0636	0.0	-0.0989
[010]	90	-0.0060	0.0	-0.0636	0.0	-0.0989
[110]	90	-0.0060	0.0	-0.0636	0.0	-0.0989
[011]	45	-0.3476	-0.3452	-0.8758	-0.8740	-0.0827
[101]	45	-0.3476	-0.3452	-0.8758	-0.8740	-0.0827
[111]	54.7	-0.2850	-0.2821	-0.7163	-0.7143	-0.0689

Table 3.8 – $\langle S_z \rangle$, $\langle L_z \rangle$ and $\langle T_z \rangle$ values calculated in the LFM model for different orientations of the external magnetic field relative to the C_3 axis of the molecule. The C_3 axis is along the [001] axis of the molecule and α is the angle between the C_3 axis and the z axis that is the direction of the X-ray propagation vector **k** (i.e. the direction of B in the present XMCD experiments). $\langle S_z \rangle (0)$ and $\langle L_z \rangle (0)$ are the values of $\langle S_z \rangle$ and $\langle L_z \rangle$ at $\alpha = 0$.

3.3.6.2 Average values

From LFM calculations, we obtained $\langle L_z \rangle(\alpha) \approx \cos(\alpha) \times \langle L_z \rangle(0)$. In the present case, α is obviously the acute angle between the C_3 axis and the **B** direction so that $0 \leqslant \alpha \leqslant \frac{\pi}{2}$ (this is equivalent to say that, for a paramagnetic ion, the magnetization is never antiparallel to the external magnetic field). Then the **k** propagation vector only maps the half sphere along the [001] direction of the C_3 axis. The average value of a $f(\alpha, \phi)$ function (α, ϕ are

the angular spherical coordinates) on the half sphere is given by:

$$f_{average} = \frac{1}{2\pi} \int_{\alpha=0}^{\alpha=\pi/2} \int_{\phi=0}^{\phi=2\pi} \sin(\alpha) f(\alpha, \phi) d\alpha d\phi \tag{3.4}$$

If $f(\alpha, \phi) = \langle L_z \rangle(\alpha) = \cos(\alpha).\langle L_z \rangle(0)$ then

$$\begin{aligned} \langle L_z \rangle_{average} &= \frac{1}{2\pi} \int_0^{\pi/2} \int_0^{2\pi} \sin(\alpha) \langle L_z \rangle(\alpha) d\alpha d\phi & (3.5) \\ &= \frac{1}{2\pi} \langle L_z \rangle(0) \int_0^{\pi/2} \int_0^{2\pi} \cos(\alpha) \sin(\alpha) d\alpha d\phi & (3.6) \\ &= \frac{1}{2} \langle L_z \rangle(0) & (3.7) \end{aligned}$$

Similarly one obtains: $\langle S_z \rangle_{average} = \frac{1}{2} \langle S_z \rangle(0)$.

If the C_3 axes are uniformly distributed in a cone of half angle at maximum of Θ then the angular average for the orbital magnetic moment yields $\langle L_z \rangle_{average} = \frac{1}{2}[1 + \cos(\Theta) \langle L_z \rangle(0)]$ and a similar expression for the spin magnetic moment. From the ratio between the measured and the calculated magnetic moments, one deduces that $\Theta = 65^\circ$.

3.4 Probing the electronic and magnetic structures of FeTp*, FepzTp and Potassium hexacyanidoferrate(III)

3.4.1 XMCD at $L_{2,3}$ edges

X-ray absorption and X-ray magnetic circular dichroism experiments have been performed at the $L_{2,3}$ edges in three low spin Fe^{III} paramagnetic precursors other than **FeTp**. XAS and XMCD spectra were recorded at 2 K under a magnetic field of 6.5 T on DEIMOS beamline of SOLEIL synchrotron. In this section, a comparison between **FeTp***, **FepzTp**, and **Potassium hexacyanidoferrate(III)** precursors and **FeTp** is presented. Figure 3.10 shows the XAS and XMCD experimental spectra. Each XAS spectra is normalized to 1 at peak **c**, and the XMCD signals are normalized to the maximum of peak **c**. Hence, the comparison of different spectral features and their respective intensities can be made directly.

XAS spectra are plotted separately in Figure 3.11. The features on XAS spectra look rather similar for all precursors and are signature of Fe^{III}_{LS}. However, slight differences can be seen, which will provide a deeper understanding of their electronic structure. The L_3 edge contains four main peaks. Except for **Potassium hexacyanidoferrate(III)**, the peaks at L_3 edge are at the same energy (**a**: 705.8 eV, **b**: 708.5 eV, **c**: 709.3 eV, **e**: 712.3 eV), the small shoulder **d** at 709.8 eV and the L_2 edge has three peaks (**f**: 718.5 eV, **g**: 721.8 eV, **h**: 725.8 eV).

For **Potassium hexacyanidoferrate(III)**, at the L_3 edge peak positions are **a**: 705.8 eV, **b**: 709.1 eV, **c**: 709.8 eV, and at the L_2 edge the peak positions are **f**: 718.5 eV, **g**: 722.5 eV, **h**: 725.4 eV. The intensity of Fe^{III}_{LS} signature peak (705.8 eV) varies in all precursors. This characteristic peak of low spin Fe^{III} ion corresponds to the transition from $2p^6t^5_{2g}$ to $2p^5t^6_{2g}$ in a simple monoelectronic picture. From the comparison of isotropic spectra, one can see that the intensity of Fe^{III}_{LS} signature peak (705.8 eV) (a/c) is ≈ 1 in **Potassium hexacyanidoferrate(III)** (1.08) and **FeTp** (1.01) whereas it is ≈ 0.76 for **FepzTp** and **FeTp***. On the high energy side of the L_3 edge of **Potassium hexacyanidoferrate(III)**, a sharp peak **e** is present at 712 eV. The presence of this feature is attributed to the 6 cyanido ligands in $K_3[(Fe^{III}(CN)_6]$ as shown in Figure 3.1 (d). Due to the presence of 6 cyanido ligands in $K_3[(Fe^{III}(CN)_6]$ one expects a charge transfer between the Fe ion and the cyanido ligands that is larger than for the other three precursors. The intensity of peak **e** is then simply a sign of π-back bonding and MLCT.[34]

Figure 3.12 compares the XMCD spectra of the different precursors. The shape of the XMCD signal is rather similar in all precursors. L_3 edge XMCD spectra has two main negative features α (705.8 eV) and γ (709.3) eV. For **Potassium hexacyanidoferrate(III)** feature γ is at 709.9 eV. The intensity of α changes considerably. The ratio α/c is 86.9 % for **Potassium hexacyanidoferrate(III)**, 110.7 % for **FeTp**, 75.6 % for **FeTp*** and 62.6 % for **FepzTp**. The intensity of the α XMCD peak for samples **Potassium hexacyanidoferrate(III)**, **FeTp*** and **FepzTp** are respectively $\approx$ 20 % , 30 % and 40 % smaller than for sample **FeTp**. These variations probably find their origin in the angular

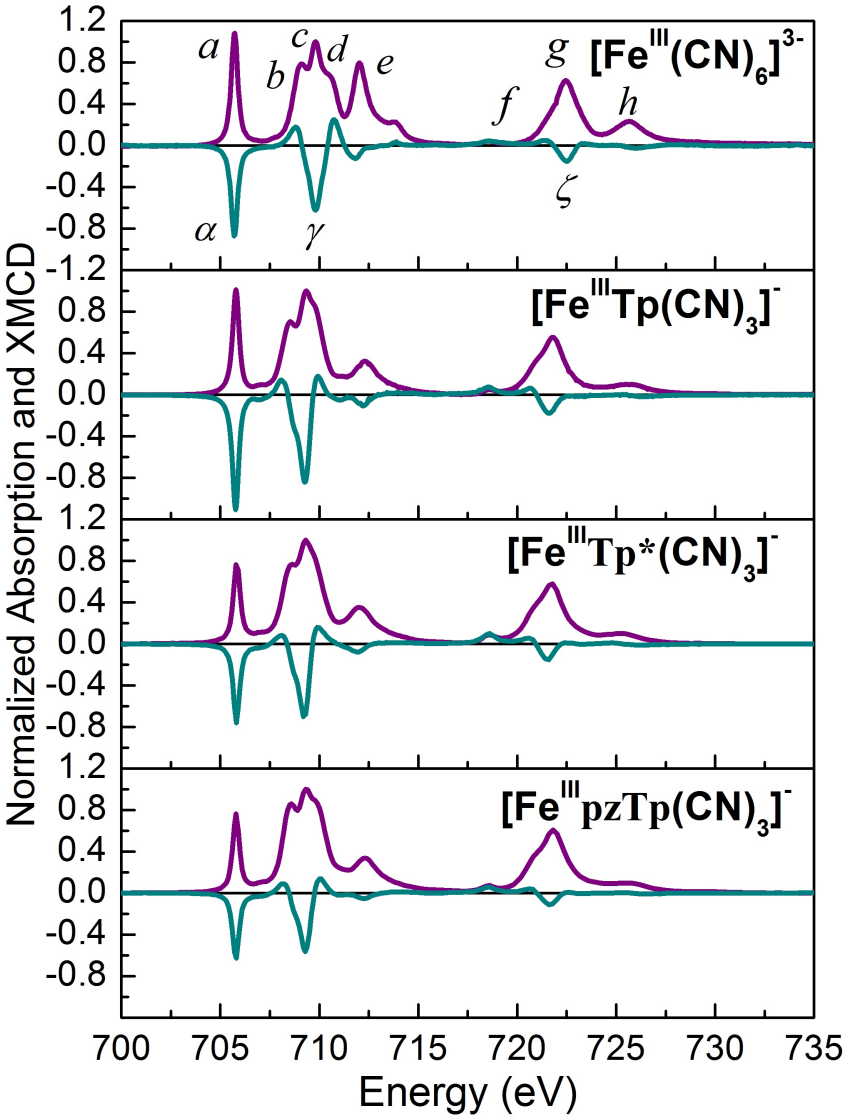

Figure 3.10 – Experimental XAS (purple line) and XMCD (green line) spectra for samples **Potassium hexacyanidoferrate(III)** $K_3[(Fe^{III}(CN)_6]$, **FeTp** $(NBu_4)[(Tp)Fe^{III}(CN)_3]$, **FeTp*** $(NEt_4)[(Tp^*)Fe^{III}(CN)_3]$ and **FepzTp** $(NEt_4)[(pzTp)Fe^{III}(CN)_3]$. All spectra all normalized to XAS at peak **c**.

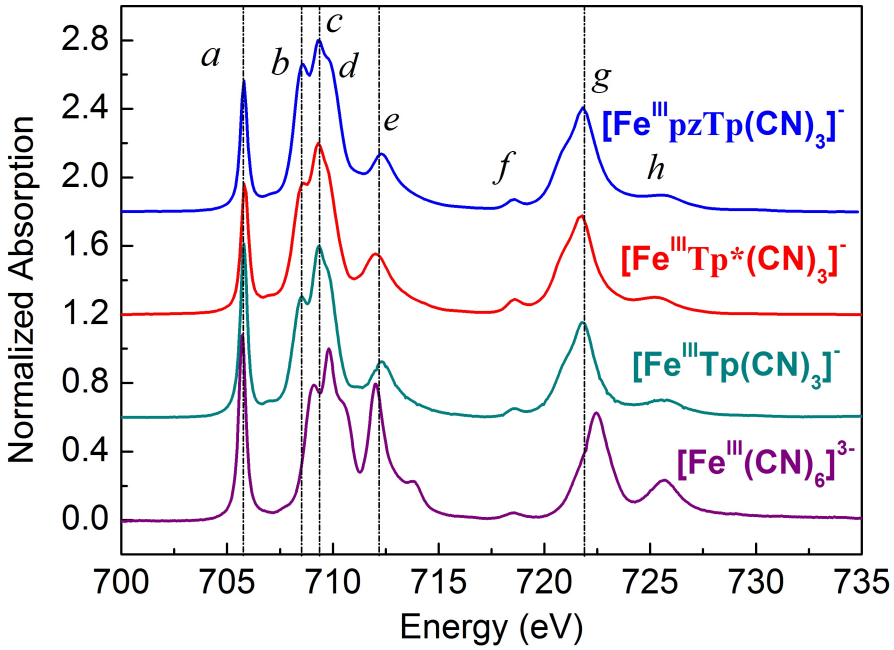

Figure 3.11 – Experimental XAS spectra measured at 2 K with 6.5 T for samples **Potassium hexacyanidoferrate(III)** $K_3[(Fe^{III}(CN)_6]$ (purple line), **FeTp** $(NBu_4)[(Tp)Fe^{III}(CN)_3]$ (green line), **FeTp*** $(NEt_4)[(Tp^*)Fe^{III}(CN)_3]$ (red line) and **FepzTp** $(NEt_4)[(pzTp)Fe^{III}(CN)_3]$(blue line).

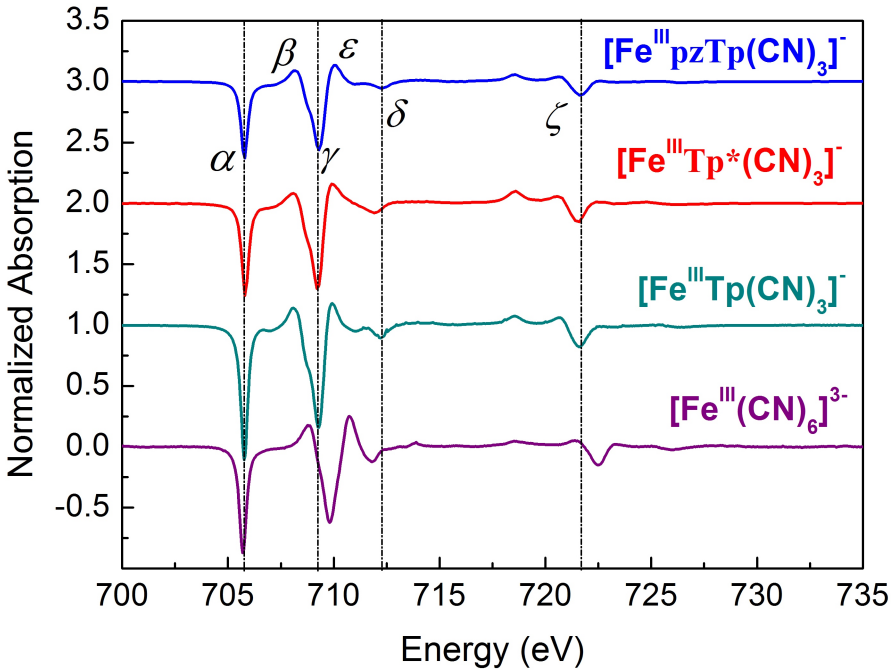

Figure 3.12 – Experimental XMCD spectra measured at 2 K and with 6.5 T for samples **Potassium hexacyanidoferrate(III)** $K_3[(Fe^{III}(CN)_6]$ (purple line), **FeTp** $(NBu_4)[(Tp)Fe^{III}(CN)_3]$ (green line),**FeTp*** $(NEt_4)[(Tp^*)Fe^{III}(CN)_3]$ (red line) and **FepzTp** $(NEt_4)[(pzTp)Fe^{III}(CN)_3]$ (blue line).

dependence that has been found for the magnetic moments in **FeTp** (see Section 3.3.6). We did not perform X-ray Natural (or Magnetic) Linear Dichroism so that this assertion is sensible but highly speculative. The difference in the relative intensities of α and γ is larger in **Potassium hexacyanidoferrate(III)** (1.4) than in other three precursors (**FeTp** (1.3), **FeTp*** (1.1) and **FepzTp**(1.1)). Also, β and ϵ, two positive peaks at the L_3 edge XMCD spectra are more pronounced in **Potassium hexacyanidoferrate(III)** than in the other precursors.

Precursor	$\frac{\alpha}{a}$	$\frac{\alpha}{c}$	$\frac{\gamma}{a}$	$\frac{\gamma}{c}$
FeTp	109.4	110.7	82.8	83.9
FeTp*	99.2	75.6	91.8	69.9
FepzTp	82.0	62.6	73.7	56.3
Potassium hexacyanidoferrate(III)	80.5	86.9	57.6	62.2

Table 3.9 – % XMCD for the four precursors.

3.4.2 Influence of crystal field on the XAS spectral shape

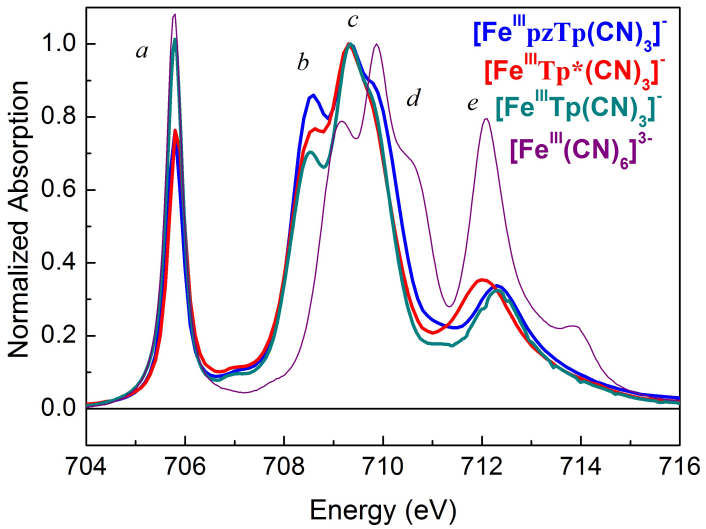

Figure 3.13 – Experimental XAS spectra measured at 2 K for samples **Potassium hexacyanidoferrate(III)** $K_3[(Fe^{III}(CN)_6]$ (thin purple line), **FeTp** $(NBu_4)[(Tp)Fe^{III}(CN)_3]$(thick green line), **FeTp*** $(NEt_4)[(Tp^*)Fe^{III}(CN)_3]$(thick red line) and **FepzTp** $(NEt_4)[(pzTp)Fe^{III}(CN)_3]$(thick blue line).

The intensity and shape of XAS spectrum at $L_{2,3}$ edges are a probe of the electronic and magnetic structure of the absorbing atom. In addition to the total nuclear charge (Z_{eff}), the effective chemical valence and the ligand field around the absorbing ion also contribute to the precise energy of the edge, the so-called chemical shifts. From the work by Hocking *et al.*, the energy position of the multiplet features (Figure 3.13) can be affected by the $10D_q$ value for crystal field and the Coulomb repulsions between the open shells.[37] The total integrated intensity of XAS $L_{2,3}$ edges spectra for the four precursors are roughly the same, indicating that the number of holes on the 3d shell is a constant for the four precursors.

This is best seen by comparison of the energy difference between peak **a** and peak **c**. The difference is roughly 4.0 eV for **Potassium hexacyanidoferrate(III)** and 3.5 eV for the three other precursors. From Ligand Field Multiplet, the energy difference between **a** and **c** scales with the $10D_q$ value around the absorbing ion so that it can be deduced from the XAS spectra that the crystal field around the **Potassium hexacyanidoferrate(III)** is 0.5 eV larger than around the three other precursors. Hocking *et al.*[37] found 10Dq = 3.8 - 4.0 eV for Potassium hexacyanidoferrate(III) and we found 10Dq = 2.8 eV for FeTp (see Table 3.2 in FeTp paper). This can be easily understood if one remembers that in the **Potassium hexacyanidoferrate(III)**, Fe is surrounded by 6 cyanides whereas for the three other precursors, Fe is surrounded by 3 cyanides and 3 Nitrogen atoms. Nitrogen ligands are known to induce much smaller crystal fields than cyanides as can be best seen from the spectrochemical series. Interestingly, one observes that the energy difference between peaks **a** and **e** is almost constant (it is 6.3 eV for **Potassium hexacyanidoferrate(III)** and 6.5 eV for the other precursors) whereas the intensity is much different. As a rule of thumb, one could say that the intensity scales with the number of surrounding cyanides, whereas the energy of peak **e** only depends on the nature of the covalent neighbour. Such an hypothesis would require an extensive study of the $L_{2,3}$ edges through Ligand Field Multiplet calculations that I have not done it during my Ph.D.

3.4.3 Comparison of SQUID with XMCD detected magnetization curves

We have shown in the preceding paper that **FeTp** entities are highly anisotropic.[82] Recently, Ridier *et al.*[106] confirmed this finding with polarized neutron diffraction. We guess that the situation is quite similar for **FeTp*** and **FepzTp**. As for **Potassium hexacyanidoferrate(III)**, the situation is not so clear. Its space group is monoclinic so that one can suppose that the expected large orbital magnetic moment for Fe is coupled to the low symmetry of the space group to yield a substantial magnetic anisotropy. Polarized neutron diffraction on $Cs_2K[Fe(CN)_6]$ by Day *et al.*[83] evidenced strong anisotropy dominated by the orbital magnetic moment.

The magnetization curves measured by SQUID for three of the four Fe precursors are reported in Figure 3.14. The magnetization curves are compared to XMCD detected magnetization curves. They have been measured by setting the energy of the monochromator at the energy of peak α where the XMCD is large. The magnetization curve is then simply the variation of the intensity of peak α as a function of the external magnetic induction. The intensity of the XMCD detected magnetization curves have been rescaled arbitrarily to fit at best the SQUID measurements. The general shape of the magnetization curves measured by either SQUID or XMCD have roughly the same shape so that there is no apparent deviation between the bulk and surface sensitive measurements of magnetization as shown in Figure 3.14.

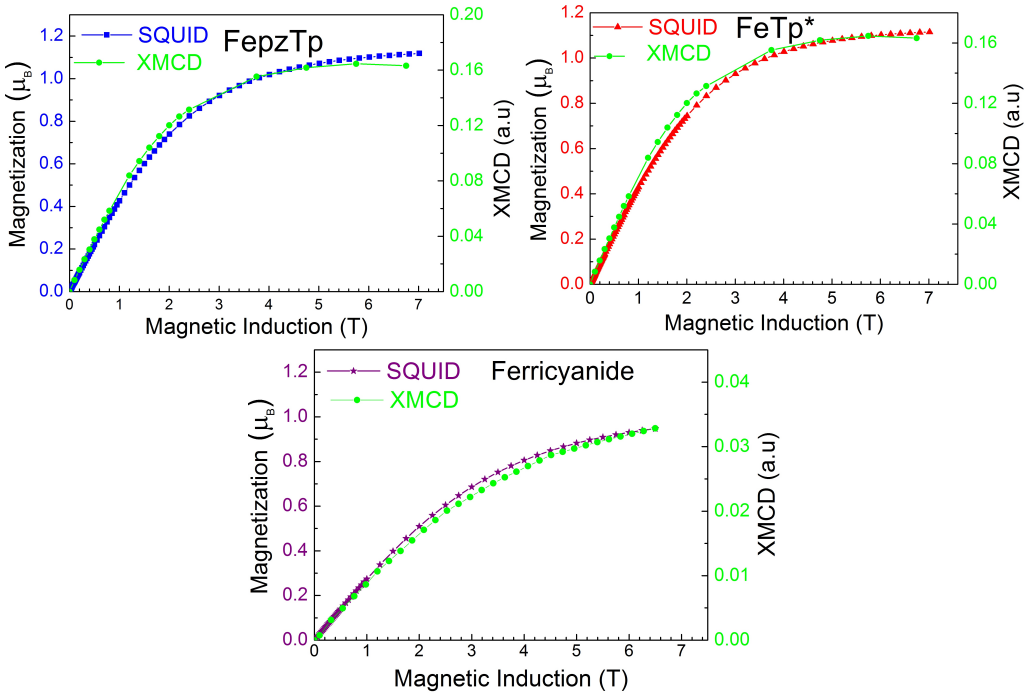

Figure 3.14 – Comparison of XMCD detected magnetization curves (light green line) at T = 2 K with 6.5 T and SQUID measurements (top left) for **FepzTp** $(NEt_4)[(pzTp)Fe^{III}(CN)_3]$(blue), (top right) for **FeTp*** $(NEt_4)[(Tp^*)Fe^{III}(CN)_3]$ (red line), and (bottom) for **Potassium hexacyanidoferrate(III)** $K_3[Fe^{III}(CN)_6]$ (purple line).

3.4.4 Application of Sum Rules

We have shown that the spin sum rule does not hold for Fe^{III}_{LS} ions.[82] Therefore, we have applied only the orbital magnetic sum rule on the experimental Fe^{III}_{LS} XAS spectra and extracted the expectation value of orbit magnetic moment $\langle L_z \rangle$ for each precursor. We find that the average value is very close to 0.6 μ_B for **FepzTp**, **FeTp*** and **Potassium hexacyanidoferrate(III)** that is the averaged expected value at 0 K for fully magnetized Fe^{III}_{LS} ion in a completely disordered system (powder). This tends to indicate that the four Fe^{III}_{LS} ions behave in a very similar way.

Precursor	$\langle L_z \rangle$
FeTp	-0.88
FeTp*	-0.52
FepzTp	-0.45
Potassium hexacyanidoferrate(III)	-0.45

Table 3.10 – Value of $\langle L_z \rangle$ from sum rules applied to the experimental spectra of precursors at $T = 2$ K and $\boldsymbol{B} = 6.5$ T.

3.5 Summary of Chapter 3

In this chapter, I have presented four different precursors with low spin Fe^{III} ions. The environment of Fe ion in the precursors remains almost unchanged when they enter the

associated PBA so that understanding the electronic and magnetic structures of Fe in the precursors can be highly enlightening for the understanding of the electronic and magnetic properties of the PBA.

The main outcome of this chapter concerns the high orbital magnetic moment that low spin Fe^{III} ions possess. The orbital magnetic moment is as large as 1.2 μ_B (along the C_3 axis) that is even larger than the spin magnetic moment that equals $\approx 1\mu_B$. This high orbital magnetic moment is accompanied by a very large magnetic anisotropy such that the easy axis of magnetization is along the trigonal (or almost trigonal) axis of the Fe ions. The anisotropy is so strong that the orbital and spin magnetic moments are almost zero when external magnetic field is applied perpendicular to the trigonal axis.

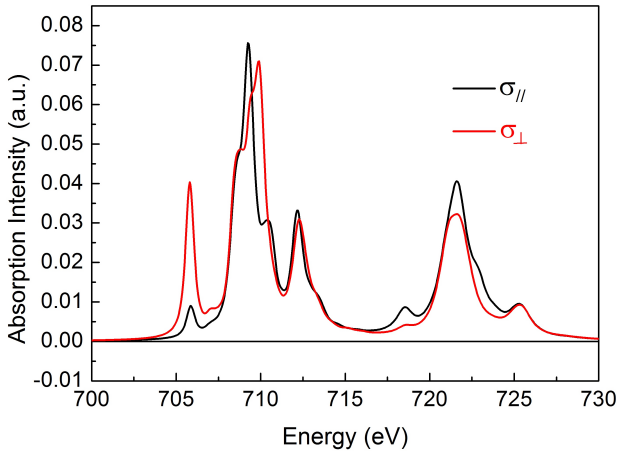

Figure 3.15 – Theoretical XNLD spectra of FeTp calculated in absence of magnetic field with the parameters given in table 3.2. The absorption cross sections are calculated for the polarization vector, $\hat{\varepsilon}$, parallel (black line) and perpendicular (red line) to the C_3 axis of **FeTp**.

In our desire to understand the XMCD of Fe $L_{2,3}$ edges, I examined very carefully the reason why the spin sum rule does not hold for low spin Fe^{III}. I showed that among the many possible sources of breakdown, the intermixing was the most important one and it could not be safely overcome to yield values for the spin magnetic moment. Although my findings are essentially applicable to low spin Fe^{III}, the type of analysis that I have developed can be extended to other ions for which the validity of the spin sum rule is under question.

We have performed Ligand Field Multiplet calculations for Fe with special emphasis for the XAS and XMCD signal of **FeTp**. The calculations helped us understand the magnetic anisotropy and the angular dependence of the orbit and spin magnetic moment. A rather large X-ray Natural Linear Dichroism (XNLD) has been predicted in our calculations (see Figure 3.15) and this opens the door to experimental measurements of XNLD or even X-ray Magnetic Linear Dichroism.

Chapter 4

Photomagnetism in Dinuclear Fe/Co Prussian Blue Analogues probed by K and $L_{2,3}$ edges XMCD

Contents

4.1 Introduction

The detailed experimental and theoretical studies of Fe bearing precursors, including the **FeTp** precursor for dinuclear PBA have been presented in the previous chapter. We showed that the **FeTp** precursor carried a large orbital magnetic moment equal to 0.9 μ_B at 2 K and with 6.5 T. This large orbital moment might play a role in the magnetic transition by linking the magnetic properties to the structure. The present chapter is dedicated to the XMCD investigations on two recently reported photomagnetic [Fe−CN−Co] PBA dinuclear complexes synthesized by Koumousi *et al.*[49] [8] Both dinuclear complexes have **FeTp** as Fe bearing precursor and have the following chemical formula :

$[(Tp)Fe^{III}(CN)_3Co^{II}PY5Me_2](CF_3SO_3)$ (labeled **1**)

$[(Tp)Fe^{III}(CN)_3Co^{II}PY5Me_2](PF_6)\cdot 2DMF$ (labeled **2**·2DMF)

The dinuclear complex **1** displays thermal- and light-induced electron transfer properties after desolvation (when it is dried in oven under vacuum) whereas **2**·2DMF needs to be kept in its mother solution to preserve its electron transfer properties. These dinuclear complexes were synthesized by Dr. Evangelia S. Koumousi (former Ph.D. student in the

group of Prof. Corine Mathonière and Dr. Rodolphe Clérac at University of Bordeaux). The results on **1** are presented in Sections 4.2 and 4.3 and the results for **2**·2DMF are presented in Section 4.4 of this chapter.

The photomagnetic measurements on **1** (see Fig. 4 in the study by Koumousi *et al.*[49]) demonstrates the first dinuclear PBA with thermal- and photo-induced reversible electron transfer. The paramagnetic state is reached by white light irradiation at 10 K. Upon heating above 45 K, the metastable state thermodynamically relaxes back to the diamagnetic state. This is by far the lowest relaxation temperature reported for any PBA molecular systems. Measurements of the macroscopic magnetic susceptibility and the X-ray diffraction patterns confirmed the complete and reversible electron transfer in **1**. This is the first dinuclear complex to exhibit both thermal and photomagnetic bistability in solid state and mimics the properties of the 3-dimensional network of PBAs. Hence, it serves as a model system with a simple structure to study the electron transfer mechanism at low temperature by XAS and XMCD which are element specific techniques. Since Complex **1** preserves its properties under vacuum, it is possible to record XAS and XMCD spectra in the Total Electron Yield mode that is the preferred mode in the soft X-ray range of Fe and Co $L_{2,3}$ edges.

The next part of the present chapter concerns the XMCD results at Fe and Co K edges for **2**·2DMF. Complex **1** is obtained by desolvation of the complex with the chemical formula $[(\mathrm{Tp})\mathrm{Fe^{III}}(\mathrm{CN})_3\mathrm{Co^{II}PY5Me_2}](\mathrm{CF_3SO_3})\cdot 2\mathrm{DMF}$ (labelled **1**·2DMF)[8,49]. In her Ph.D. manuscript, E.S. Koumousi detailed the magnetic and photomagnetic studies on **1**·2DMF that reveal a partial electron transfer.[49] Moreover, single crystal analysis suggests that van der Waals interactions between the solvent molecules and the [Fe–CN–Co] complex influence the electron transfer process. Therefore, by slight modifications in the environment of these molecular complexes, E.S. Koumousi has been able to obtain new systems showing interesting thermal- and/or light-induced intramolecular electron transfer. Indeed, Koumousi found that different counter ions ($\mathrm{CF_3SO_3^-}$ *vs* $\mathrm{PF_6^-}$) induce different temperatures of thermal conversion and different relaxation temperature of the metastable state. Thus, Koumousi obtained another dinuclear complex **2**·2DMF for which macroscopic magnetic studies evidenced a complete thermal-induced electron transfer in presence of solvent molecules. The electron transfer takes place at 100 K with 20 K wide thermal hysteresis. The transition temperature is ≈70 K lower than the transition temperature for complex **1**. In addition, the photo-induced paramagnetic state $\mathrm{Fe^{III}_{LS}}$–$\mathrm{Co^{II}_{HS}}$ fully relaxes into the diamagnetic state $\mathrm{Fe^{II}_{LS}}$—$\mathrm{Co^{III}_{LS}}$ at 53 K compared to 45 K for complex **1**.[8] Complex **2**·2DMF can only be measured with its solvent, therefore, XAS and XMCD spectra at $L_{2,3}$ edges are almost impossible to record. This prompted us to record the XMCD signals at Fe K edge. Another related complex, the $[\mathrm{Fe_2Co_2}]$ square, has already been studied by XAS where the thermal and X-ray induced electron transfer have been followed at Fe and Co K edges.[58,59]

XAS and XMCD are excellent probes to follow the change in oxidation state, the spin state and the local magnetic moments during thermal- or photo-induced electron transfer. We succeeded to draw a nice picture of the electronic structure of complex **1**. For complex

2·2DMF, the situation is not as satisfying because the analysis of Fe and Co K edges mainly rests on a finger print approach and performing XMCD calculations within the DFT approximation is well beyond the scope of my thesis.

4.2 Paper II: XMCD studies at K and $L_{2,3}$ edges of Fe and Co in dinuclear complex 1

Status: To be submitted

Atomic scale evidence of the switching mechanism in a photomagnetic CoFe dinuclear Prussian Blue Analogue

Sadaf Fatima Jafri[1], Evangelia S. Koumousi[2,3,4,5], Marie-Anne Arrio[1], Amélie Juhin[1], Dmitri Mitcov[4,5], Mathieu Rouzières[4,5], Pierre Dechambenoit[4,5], Corine Mathonière[2,3], Rodolphe Clérac[4,5], Dongfeng Li[6], Edwige Otero[7], Fabrice Wilhelm[8], Andrei Rogalev[8], Loïc Joly[7,9], Jean-Paul Kappler[7,9], Christophe Cartier dit Moulin[10,11], and Philippe Sainctavit*[1,7]

[1]Institut de Minéralogie, de Physique des Matériaux et de Cosmochimie, UMR7590, CNRS, UPMC, IRD, MNHN, 75252 Paris Cedex 05, France
[2]CNRS, ICMCB, UPR 9048, F-33600, Pessac, France.
[3]Univ. Bordeaux, ICMCB, UPR 9048, F-33600, Pessac, France.
[4]CNRS, CRPP, UPR 8641, F-33600, Pessac, France.
[5]Univ. Bordeaux, CRPP, UPR 9048, F-33600, Pessac, France.
[6]College of Chemistry, Key Laboratory of Pesticide and Chemical Biology of Ministry of Education, Central China Normal. University (CCNU), 430079 Wuhan, P. R. China.
[7]Synchrotron SOLEIL, L'Orme des Merisiers Saint-Aubin, France.
[8]European Synchrotron Radiation Facility, BP 220, F-38043 Grenoble, France.
[9]CNRS, IPCMS, BP 43, 67034 Strasbourg Cedex 02, France.
[10]CNRS, UMR 8232, Institut Parisien de Chimie Moléculaire, F-75005, Paris, France.
[11]Sorbonne Université, UPMC Univ Paris 06, UMR 8232, IPCM, F-75005, Paris, France.

Abstract

Molecular complexes based on Prussian Blue Analogues have recently attracted considerable interest for their unique bistable properties combined to ultimately reduced dimensions. Here we investigate the first dinuclear Fe/Co complex exhibiting both thermal and photomagnetic bistability in solid state. Through experimental and theoretical approaches combining element selective probes, X-ray Absorption Spectroscopy and X-ray Magnetic Circular Dichroism- and Ligand Field Multiplet calculations, we were able to evidence the changes occuring at the atomic scale in the electronic and magnetic properties: *(i)* the 300 K phase and the light-induced excited state at 4 K are both built from Fe^{III}_{LS}—Co^{II}_{HS} paramagnetic pairs with no apparent reorganization of the local structure, *(ii)* the 100 K phase is built from Fe^{II}_{LS}—Co^{III}_{LS} diamagnetic pairs, *(iii)* the light-induced excited state is fully relaxed at ≈50 K. In the paramagnetic pairs at 2 K and under an external magnetic induction of 6.5 T, both Fe and Co ions exhibit a rather large orbital magnetic moment (0.31 μ_B and 0.32 μ_B, respectively) and no antiferromagnetic coupling was detected between both ions.

4.2.1 Introduction

With growing technological interests, smart molecular materials with reduced dimensions[88,89,109,110] are being designed, synthesized and investigated for quantum computing applications,[111] which include, for instance, switching devices,[112] data storage and processing,[113] and logic gates[114] where a single molecular specie is employed to perform numerous binary operations based on logic. Molecular complexes exhibiting externally-controlled bistable physical properties are well-suited for these applications because of their flexible and versatile chemistry. The ON-OFF switching capability between two molecular states, for example, magnetic (ON or 1) and diamagnetic (OFF or 0) states is termed as bi-stability. This switching phenomenon can be used to store data as binary units "0" and "1" if the molecules possess a memory effect after the triggering source (light, temperature, magnetic field, pressure etc) has been switched off. To develop such smart materials using state-of-the-art techniques, careful manipulation and tailoring of molecular properties, with control down to a single spin, is a current challenge.[17,85,88,115] In this regard, the versatile molecular chemistry of mixed valence cyanido-bridged Prussian Blue (Fe^{II}–CN–Fe^{III}) and its derivatives (A^{II}–CN–B^{III}, where A and B are 3*d* transition metal ions) referred to as Prussian Blue analogues (PBA) has been exploited to engineer bi-stable systems.[9] The first evidence of light-induced magnetism in 3-dimensional network of Fe/Co PBA by Hashimoto and co-workers[6] fuelled the quest of designing molecular magnets with novel functionalities in this family. Fe/Co PBA molecular magnets are unique systems exhibiting bi-stability where electron transfer transforms Fe^{II}_{LS} (S=0)–CN–Co^{III}_{LS} (S=0) diamagnetic entities into Fe^{III}_{LS} (S=1/2)–CN–Co^{II}_{HS} (S=3/2) paramagnetic ones (LS = low spin; HS = high spin).

The presence of the bi-stability is attributed to this metal-to-metal electron transfer via cyanido bridge which is tuned by external parameters like light, temperature and pressure.[6,7,20,85–87,116] Reducing the dimensionality of molecular complexes allows miniaturisation of devices, which is the ultimate goal. The first step is to develop Fe/Co nanostructures of PBA with desired thermal and photo-induced electron transfer properties. Some attempts have been made to develop Fe/Co cyanide complexes but thermal- and/or photo-induced electron transfer properties could not be observed.[38–40] The first evidence of thermally induced metal-to-metal electron transfer is reported in cyanido-bridged Fe/Co pentanuclear [Fe_2Co_3] molecule by Dunbar and co-workers in 2004.[41,42] PBA based [Fe_nCo_n] nanostructures such as 1-dimensional chain,[48,57,77,117] and 0-dimensional molecular cube,[43] square,[11,45,46,118] and dinuclear complex[49,119] have been synthesized. However, few are supported by structurally characterized light-induced metastable state.[11,120] Furthermore, there are not many examples where the light-induced electron transfer is observed at the atomic scale using XAS/XMCD techniques.[59]

Recently, Koumousi et al. succeeded in synthesizing the first dinuclear complex which exhibits both thermal and photomagnetic bistablility in solid state.[49] It is a dinuclear complex which is built from Fe^{III} cyanides and Co^{II} ions that can be seen as the elementary motif of Fe/Co PBA (see Figure 4.1). At room temperature, the Fe/Co PBA is in the Fe^{III}_{LS} (S=1/2)—CN—Co^{II}_{HS} (S=3/2) paramagnetic state and it undergoes a temperature induced

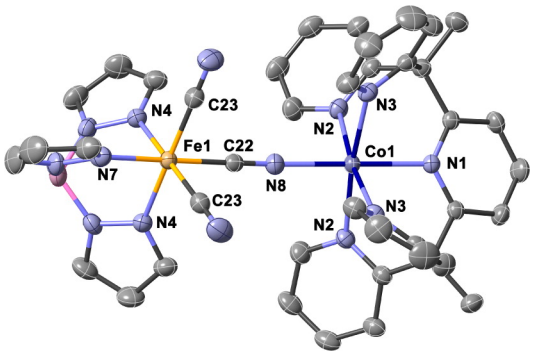

Figure 4.1 – Molecular structure of the cationic complex of dinuclear Fe/Co PBA. All anions, lattice solvents, and hydrogen atoms are omitted for clarity. Fe, Co, N, C, and B atoms are indicated in orange, dark blue, light blue, gray, and pink, respectively.

transition below 150 K toward the Fe^{II}_{LS} (S=0)—CN—Co^{III}_{LS} (S=0) diamagnetic state. At low temperature (below 10 K) and under white light irradiation, diamagnetic pairs undergo a light-induced transition toward the Fe^{III}_{LS} (S=1/2)–CN–Co^{II}_{HS} (S=3/2) paramagnetic state. A quick increase in χT product is observed at 10 K and within 4 hours of irradiation it reached at the maximum value of 2.77 cm^3 K mol^{-1}. The electron transfer process is complete and reversible, which is for the first time observed in a dinuclear system.[9,49] The thermal- and optical bistability of the this dinuclear complex can be used to design new multifunctional materials. All the above mentioned phase transitions driven by electron transfer have been proposed to explain the variation of the magnetic susceptibility measured by SQUID magnetometry.[49] However, there has been so far no direct confirmation at the atomic scale of Fe and Co ions that such a electron transfer does indeed take place. Therefore, we have investigated the modification of the electronic and magnetic structure by temperature and light irradiation using X-ray Absorption Spectroscopy (XAS) and X-ray Magnetic Circular Dichroism (XMCD), which are element-specific synchrotron based techniques. The goal is to determine the electronic and magnetic structures of Fe and Co ions in the three phases involved in the photomagnetic mechanism: the 300 K paramagnetic phase, the 100 K diamagnetic phase and the 4 K photo-induced paramagnetic phase. The analysis of the XAS and XMCD experimental data is supported by Ligand Field Multiplet (LFM) calculations[93] developed by Theo Thole and application of magneto-optical sum rules[69,70] in order to yield the orbit and spin magnetic moments of Fe and Co in the 4 K photo-induced paramagnetic phase. The nature of the magnetic coupling between Fe and Co ions in the dinuclear complex was investigated using element specific magnetization curves measured by XMCD.

Previously, element specific and surface sensitive XAS has been successfully employed to understand bistability in other molecular systems such as spin cross over (SCO) systems,[121–123] or Cobalt-dioxolene Valence tautomers.[124–127] In SCO compounds, one follows a high spin (HS) to low spin (LS) transition in the absence of electron transfer while in Cobalt-dioxolene Valence tautomers, an electron transfer takes place between a Cobalt ion and the dioxolene ligand. In PBAs, the situation is quite different from both previous ones because one observes a metal-to-metal electron electron transfer via cyanido ligands.[14,15,21,26,51,58,59] The metal-to-metal electron transfer is accompanied by a HS to

LS transition of the Co ions. On cyanido-bridged tetranuclear systems of Fe/Co PBA, investigation of thermal- and photo-induce electron transfer by XAS is reported by Sekine *et al.* at K edges.[58,59] The originality of the results shown in the present work stems from the possibility to record XAS and XMCD spectra independently for both metallic ions involved in the electron transfer, thus providing an atomic scale picture of the switching mechanism and to check possible antiferromagnetic coupling as suggested by Koumousi *et al.*[49]

4.2.2 Experimental Section

4.2.2.1 Sample Preparation

The FeCo dinuclear complex referred to as sample **1** with the with stoichiometric formula $[(Tp)Fe^{III}(CN)_3Co^{II}(PY5Me_2)](OTf)$ (OTf : CF_3SO_3, Trifluoromethanesulfonate) and the corresponding Fe and Co precursors (referred to as **2** and **3** respectively) were synthesized following the procedure used by Koumousi *et al.*[49] The chemical formulae for Fe and Co are $(NBu_4)[(Tp)Fe^{III}(CN)_3]$ and $[(Tp)Co^{II}(PY5Me_2)\cdot H_2O](BF_4)_2$ respectively. For sample **1** the metal-to-metal electron transfer in solid state was studied using standard magnetometric techniques, single crystal diffraction and optical reflectivity methods (Reference by Koumousi *et al.* and Supporting Information).[49] The crystals of **1** were then deposited on doubly coated conductive carbon tape suitable for cryogenic temperatures and mounted on a copper sample holder.

4.2.2.2 XAS and XMCD measurements

XAS and XMCD measurements were performed at both K and $L_{2,3}$ edges of Fe and Co. Spectra at the $L_{2,3}$ edges were recorded on the soft X-ray beamline DEIMOS at SOLEIL synchrotron (France)[90] and at SIM beamline in SLS (Paul Scherrer Institute, Switzerland).[54,128] All spectra at $L_{2,3}$ edges were measured by recording the total electron yield (TEY) under UHV conditions. K edge XAS spectra were recorded at ID12 beamline[129,130] of the ESRF (France) by measuring the total fluorescence yield.

The DEIMOS beamline is equipped with a 7 T cryo-magnet that has a variable temperature insert. To avoid any spurious signals, XMCD signal was measured by taking the difference of two XAS spectra recorded for left and right polarized X-rays with propagation vector parallel or antiparallel to the direction of external magnetic induction $\boldsymbol{B}$. By definition, the XMCD signal is obtained by $\sigma_{\mathrm{XMCD}} = \sigma^- - \sigma^+$ where $\sigma^- = [\sigma_L(B^-) + \sigma_R(B^+)]/2$ and $\sigma^+ = [\sigma_L(B^+) + \sigma_R(B^-)]/2$.[131] XAS and XMCD spectra for sample **1** were first recorded at 300 K, 100 K and 4 K to check for thermal-induced conversion. At 4 K, the sample was irradiated with a laser ($\lambda =$ 660 nm) for 2 hours and the the photo-converted state was studied. We also followed the relaxation of the light-induced excited state when the temperature was raised up to 50 K. The reversibility of the thermal- and photo-induced conversion has been checked by recording XAS spectra for temperatures between 100 K and 300 K.

To check for the nature of the magnetic coupling between the Fe and Co ions in the photo-induced state, XMCD signals should be measured in sub-kelvin temperature because

the Fe–Co exchange coupling is expected to be small. On the SIM beamline, the French TBT-mK cryomagnet is a unique tool to perform XMCD measurements in the sub-kelvin range down to 300 mK.[54] However, due to technical issues, the measurements could only be performed at 2 K. At 2 K, the sample was irradiated using the 660 nm laser and the XMCD signal of the photo-excited paramagnetic state was measured. Thanks to XMCD, it is possible to record magnetization curves that are specific of the absorbing ion. One sets the energy of the monochromator at the maximum (in absolute value) of the XMCD signals and then sweeps the intensity of the magnetic induction. As can be seen from the magneto-optical sum rules, the variation of the intensity of the XMCD signal at $L_{2,3}$ edges is a measure of the magnetization of the absorbing atom.

At ID12 beamline, Fe and Co K edge XAS were measured at 300 K and at 2 K. At 2 K, sample **1** was irradiated for 3 hours by the white light delivered by a tungsten halogen lamp and then Fe and Co K edge spectra were measured in the photoexcited state.

4.2.3 Ligand Field Multiplet calculations

The quantitative information from the XAS/XMCD spectra can be extracted by using Ligand Field Multiplet (LFM) calculations.[93,132,133] These calculations are performed employing LFM theory which is developed by Theo Thole[93], based on atomic theory developed by Cowan[74] and the crystal field interactions (*i.e.*, symmetry) described by Butler.[94] We have performed LFM calculations to simulate the Co L_3 edge spectra. The LFM calculations on Co are done in distorted octahedral environment. The parameters of calculations are presented in the supporting information in Table 4.1. In addition, application of magneto-optical sum rules[69,70,91] are applied on the experimental spectrum to obtain orbit magnetic moments for Fe and Co ions in photo-induced state.

4.2.4 Results

4.2.4.1 Thermal-and light-induced metal-to-metal electron transfer process

In Figure 4.2 are shown the XAS experimental spectra at Fe and Co L_3 edges for sample **1** at 300 K, 100 K before laser irradiation and at 4 K after laser irradiation (λ = 660 nm). At 300 K before irradiation, the spectral shape is characteristic of Fe^{III}_{LS}[37] and Co^{II}_{HS} ions.[25,32] Peak **a** on the Fe L_3 XAS is the electronic signature of Fe^{III}_{LS} ions surrounded by cyanido ligands, and peaks **a**' to **d**' on the Co L_3 XAS are mainly the contribution from Co^{II}_{HS}.[37] After sample **1** is cooled down to 100 K, peak **b** at the Fe L_3 edge and peak **e**' at the Co L_3 edge become the main features. Both **b** and **e**' can be respectively associated to Fe^{III}_{LS} and Co^{III}_{LS} ions, thus confirming the temperature-induced switching mechanism proposed from SQUID measurements.[49] Nevertheless, at 100 K peaks **a**, **a**', **b**' and **c**' have not completely disappeared, which implies that conversion is not complete for both Fe and Co ions. One can estimate that around 22 % of the high temperature phase is still present at 100 K. This percentage is determined by linear combinations of LFM reference spectra calculated for Co^{II}_{HS}, Co^{III}_{LS}, Fe^{II}_{LS} and Fe^{III}_{LS} ions. Then, sample **1** is further cooled down to 4 K and irradiated by a laser (λ = 660 nm). From a straightforward comparison with the XAS signature at 300 K and with literature[37], it is clear that the light-induced state is

mainly built from paramagnetic Fe^{III}_{LS} and Co^{II}_{HS} species. The respective contributions of low spin and high spin characteristic features in the Fe and Co L_3 XAS spectra therefore clearly confirm the existence of thermal- and photo-induced electron transfer.

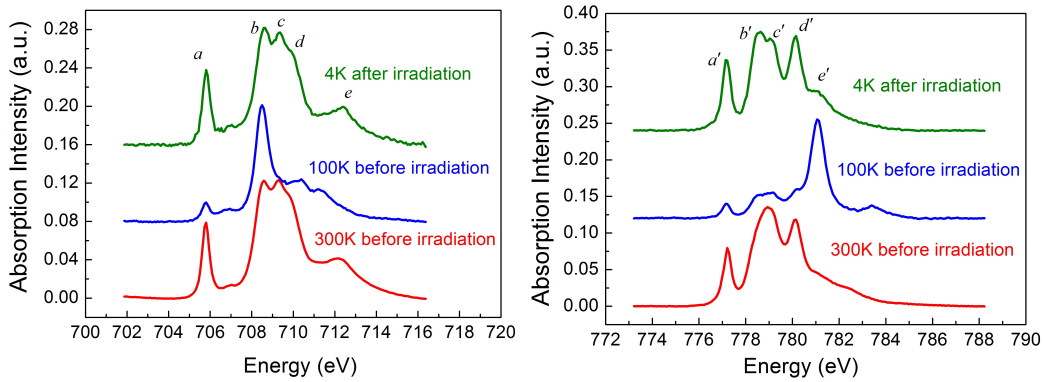

Figure 4.2 – Experimental XAS spectra at the Fe (left) and Co (right) L_3 edge before laser irradiation at 300 K (red line), 100 K (blue line) and 4 K (green line) after irradiation (λ = 660 nm, 2 hours) at $\boldsymbol{B}$ = 2 T.

4.2.4.2 Thermal Relaxation of the photo-induced excited state

We have recorded the relaxation of the photoexcited state to the thermodynamically stable diamagnetic state when the temperature is increased. After sample **1** is cooled to 4 K and irradiated with the 660 nm laser, the temperature is raised from 4 K to 10 K and then from 10 K to 50 K by steps of 5 K. At each temperature point, Fe and Co L_3 edges spectra are recorded (Figure 4.3). When the temperature increases, one observes a gradual decrease from the main signature of Fe^{III}_{LS} (peak **a**) and Co^{II}_{HS} (peak **a'**) ions. As mentioned before, at 100 K the signals for Fe and Co before and after irradiation are built from 78 % of Fe^{II}_{LS}—Co^{III}_{LS} diamagnetic pairs and 22 % of residual Fe^{III}_{LS}—Co^{II}_{HS} paramagnetic pairs. At a given temperature, each spectrum is analyzed as a linear combination of the spectra measured at T = 4 K and T = 100 K (see supporting Information Figure 4.17), which allows plotting the fraction of each paramagnetic ion as a function of temperature (Figure 4.4). One observes that the relaxation curves for Fe and Co are almost identical indicating that the reduction of Fe ions is accompanied by the oxidation of Co ions, as expected for the electron transfer mechanism. The relaxation is almost finished at 50 K.

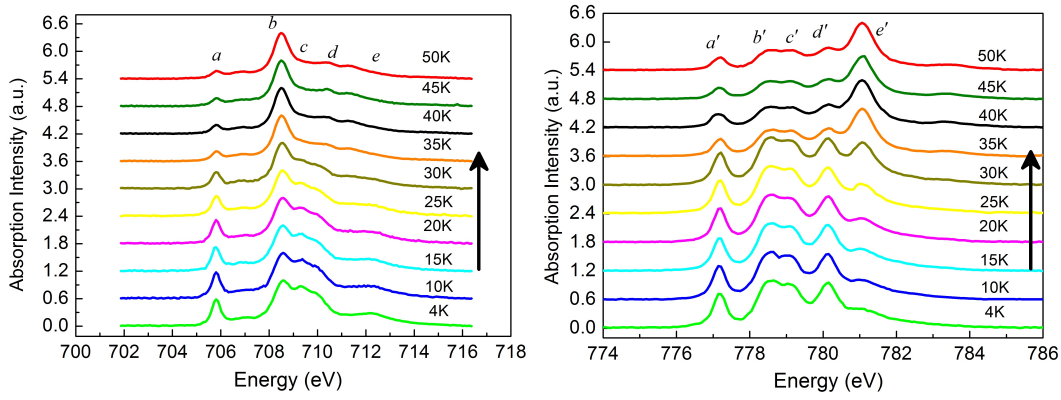

Figure 4.3 – L_3 edge XAS spectra measured for Fe (left) and Co (right), following the relaxation of the light-induced excited state Fe^{III}_{LS}—Co^{II}_{HS} as a function of temperature under $\boldsymbol{B}$ = 2 T.

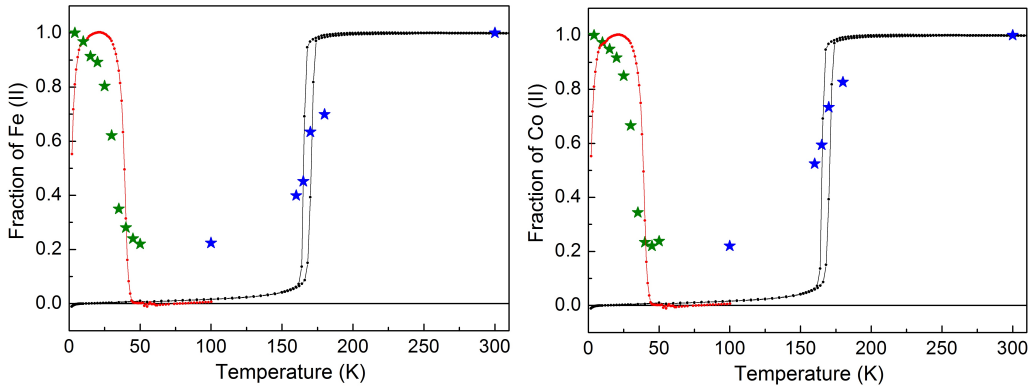

Figure 4.4 – Fraction of paramagnetic ion (green stars), as a function of temperature, extracted from the quantitative analysis of XAS spectra measured at Fe (left) and Co (right) L_3 edge (0.1 K/min). The product of χT vs T, obtained from SQUID measurements (0.4 K/min), is shown in black (thermal-induced relaxation) and red solid line (photo-induced relaxation). The size of the symbol accounts for the error bar on the x and y axis.

A similar series of measurements was performed between 100 K and 300 K for intermediate temperatures equal to 160 K, 165 K, 170 K and 180 K. The percentage of each paramagnetic species was determined from the linear combination of the spectra measured at 100 K and 300 K (Figure 4.4). The error bars on the x-axis ($\leq$ 5 K) and on the y-axis ($\approx$ 5 %) arise respectively from the temperature stabilization of the cold finger and from the relaxation during the recording process.

For comparison the variation of the magnetic susceptibility χT that was measured by SQUID magnetometer is reported in Figure 4.4. The normalized product χT is almost independent of temperature: it is zero for a diamagnetic pair and equals 3 $cm^3.K.mol^{-1}$ for a Fe^{III}_{LS}—Co^{II}_{HS} paramagnetic pair.

4.2.4.3 Reversibility of the electron transfer process

One major point is to check whether the spectral modifications observed with temperature and light irradiation are fully reversible, in order to discard any degradation of the sample that could explain these changes. Starting from the light-induced spin state at 4 K, we have warmed up sample **1** and recorded XAS spectra at 100 K and at 300 K. By doing so, sample **1** has followed a complete temperature cycle: 300 K, 100 K, 4 K and irradiation by a 660 nm laser, 100 K, 300 K. Spectra recorded at 100 K before and after the photomagnetic conversion are almost identical at both the Fe and Co L_3 edges (Supporting Information: Figure 4.8). They bear the signature of Fe^{II}_{LS} and Co^{III}_{LS} ions with small contributions from Fe^{III}_{LS} and Co^{II}_{HS} ions. At 300 K, the two spectra recorded at the beginning of the temperature cycle and at the very end bear the clear signature of Fe^{III}_{LS} and Co^{II}_{HS} ions (Supporting Information: Figure 4.9). This confirms the complete reversibility of the electron transfer process for both the temperature-induced and the light-induced conversion. In other words, there is no sign of any sample degradation under the action of X-rays or the 660 nm laser.

For completeness, the Fe and Co K edges XAS spectra were recorded for sample **1** at 300 K, at 4 K before light irradiation and at 4 K after light irradiation. Since the escape depth for hard x-ray photons at the Fe and Co K edges is larger than 10 μm, the obtained information relates to the bulk of the sample while at the Fe and Co $L_{2,3}$ edges, the escape

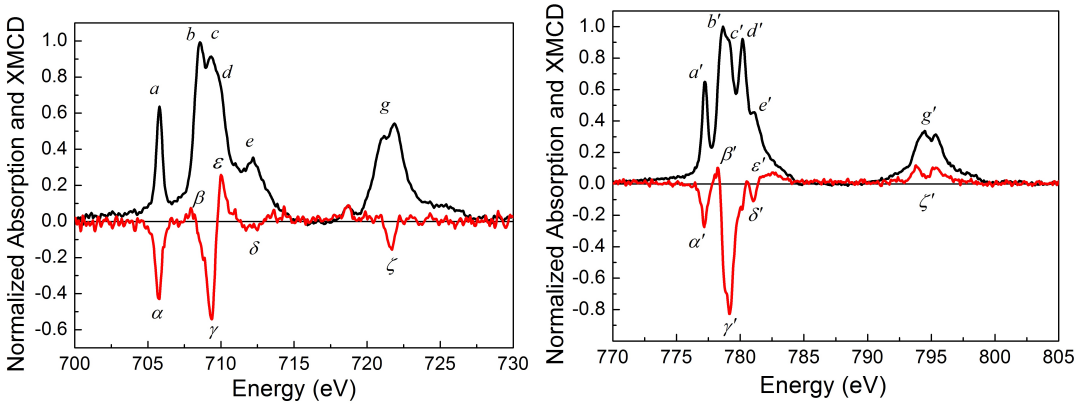

Figure 4.5 – Experimental XAS (black line) and XMCD (red line) at the Fe (left) and Co (right) $L_{2,3}$ edges at $T = 4$ K and $\boldsymbol{B} = 6.5$ T.

depth of the electrons is not larger than 5 nm. The whole set of results is presented in Supporting Information (Figure 4.10, Figure 4.11, Figure 4.12, Figure 4.13) and the K edge data yield conclusions that are very similar to the ones obtained at the Fe and Co $L_{2,3}$ edges.

4.2.4.4 Magnetic properties of the light-induced excited state

XMCD spectra have been recorded at the Fe and Co $L_{2,3}$ edges at 4 K after photoexcitation, in an external magnetic induction of 6.5 T (Figure 4.5). The large intensity of the Fe L_2 edge on the XAS signal is a clear indication that Fe is in a low spin state,[134,135] while the relatively small Co L_2 edge is a sign that Co ions are in a high spin state. XMCD signals at the Fe L_3 and the Co L_3 edges are both negative, which evidences that Fe and Co total magnetic moments point in the same direction at $T = 4$ K and $\boldsymbol{B} = 6.5$ T. In such conditions, there is no indication of an antiferromagnetic coupling between Fe and Co ions.

The XMCD signal at the Fe $L_{2,3}$ edges has three main negative features α, γ, ζ and a moderate positive one, β. Its intensity is not small since the γ feature amounts to 57 % of the maximum of the L_3 edge. Thus, from the shape and intensity of XMCD, one expects a moderate total magnetization where a rather large orbital magnetic moment is likely to overcome the spin magnetic moment. This is confirmed by application of the orbital magneto-optical sum rule, which yields 0.31 $\mu_B \pm 0.1$ for the orbital magnetic moment. The XMCD signal at the Co $L_{2,3}$ edges is characterized by a large negative contribution γ' accompanied by two smaller negative ones α' and δ', while the XMCD signal at the L_2 edge gives a small positive contribution. The intensity of the γ' peak is rather large and amounts to 83 % of the maximum of the Co L_3 edge spectrum. One thus expects a rather large magnetic moment carried by the Co ions with a large contribution from the orbital magnetic moment. Application of the orbital magneto-optical sum rule yields 0.32 $\mu_B \pm 0.1$.

The magnetization curves detected by XMCD independently for Fe and Co ions are shown in Figure 4.6. They have been recorded by setting the monochromator at maximum of L_3 edge XMCD signal for Fe (E = 709.33 eV) and Co (E = 779.18 eV) between +5 T and -5 T. one sees that complete magnetic saturation is not achieved for both Fe and Co. No detectable opening of the magnetization curves is observed. In addition, the shape of

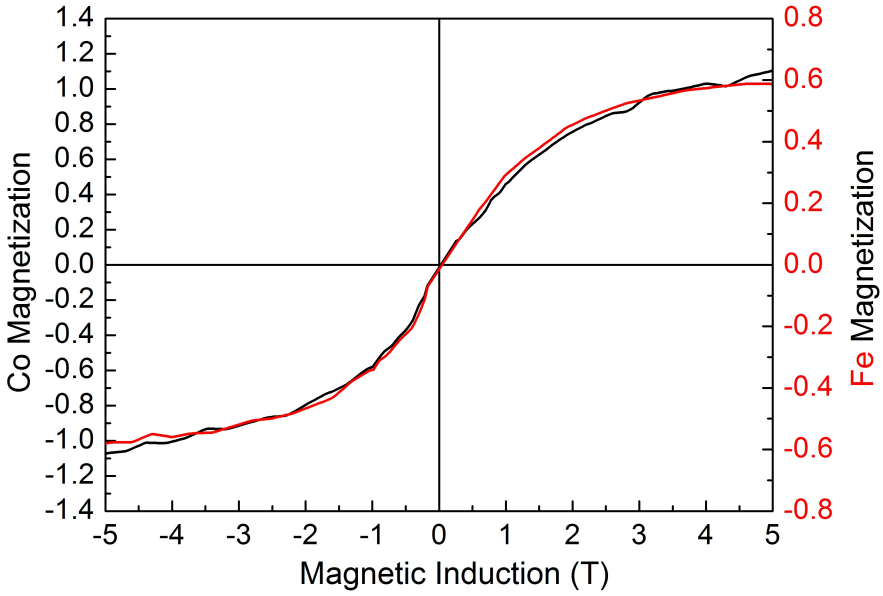

Figure 4.6 – Field dependence of the maximum of XMCD signal at the L_3 edge for Fe (red line) and Co (black line), measured respectively at 709.33 eV and 779.18 eV at $T = 2$ K. Since the largest feature in the XMCD signal is negative for a positive values of $\boldsymbol{B}$, XMCD detected magnetization curves were multiplied by -1 in order to present them with the same convention as for SQUID detected magnetization curves. The XMCD intensity are normalized with respect to XAS as in figure 4.5.

the magnetization curves are very similar for both Fe and Co, so that there is no sign of any antiferromagnetic coupling between both ions at $T = 2$ K. It is not possible from the present set of magnetization curves to determine if the Fe and Co ions are ferromagnetically coupled or if they simply experience a similar magnetization under the action of the external magnetic induction.

4.2.5 Discussion

The present experimental results clearly evidence that the temperature-induced conversion between 300 K and 100 K corresponds to a electron transfer transition between the Fe^{III}_{LS}—Co^{II}_{HS} paramagnetic pair into the Fe^{II}_{LS}—Co^{III}_{LS} diamagnetic pair. At lower temperature, around 4 K, the Fe^{II}_{LS}—Co^{III}_{LS} diamagnetic pair transforms almost completely into the Fe^{III}_{LS}—Co^{II}_{HS} paramagnetic one upon light irradiation. This result is obviously in line with what had been claimed by Koumousi *et al.*[49] on the same system based on SQUID magnetometry data. Nevertheless, we want to stress that the present work reports the first direct evidence of the electronic state of Fe and Co ions at the atomic scale, and this for the different phases involved in the switching mechanism. This conclusion is absolutely unambiguous since the spectral features associated to the $L_{2,3}$ edges XAS spectra of Fe^{II}_{LS}, Fe^{III}_{LS}, Co^{II}_{HS} and Co^{III}_{LS} are well documented in the literature for the experimental spectra as well as for the theoretical spectra calculated in the Ligand Field Multiplet approach.[25,26,32,33,37,126,136] In addition, the features at the K edges support this conclusion although quantitative results are more difficult to extract.

At $T = 100$ K, it has been found that the temperature-induced conversion was not complete. This is regularly observed when temperature- or light-induced conversions are

followed by XAS at $L_{2,3}$ edges. Indeed, depending on the samples Poneti et al. observed between 50 % and 60 % of residual high temperature phase at 100 K,[126,127,137] and Warner et al. observed between 10 % and 55 % of residual depending on the sample thickness.[121] The temperature induced conversion is possible when the environement of the Co ions allows enough flexibility so that the site can accommodate a Co^{II}_{HS} to Co^{III}_{LS} transition.[14,32,33] At the very surface of complex **1** it is likely that the Co coordination sphere undergoes a partial reorganisation that might prevent the temperature-induced electron transfer.

At 300 K and at 4 K after irradiation, sample **1** is built from Fe^{III}_{LS}—Co^{II}_{HS} paramagnetic pairs. From the comparison of both XAS spectra at the Fe $L_{2,3}$ edges, one can conclude that the electronic and local structure of Fe at 300 K is very similar to that at 4 K after irradiation (Figure 4.7). On the contrary, the same comparison for the Co $L_{2,3}$ edges clearly indicates that the two spectra at 300 K and at 4 K are quite different: for the latter, feature **a**' is sharper, the intensities of features **b**' and **c**' are reversed and feature **e**' is larger. These differences cannot originate from an incomplete photomagnetic conversion as can be deduced from the more intense feature **a**'. They might arise either from a temperature dependence of the Co $L_{2,3}$ edges spectra, or from local rearrangements around the Co ions similar to the ones observed for 3-dimensional PBA molecule based magnets.[25,26,32,33] Therefore, XAS spectra were calculated in the Ligand Field Multiplet approach for a Co^{II} ion in the same environment at 4 K and 300 K for same set of parameters (Supporting Information Table 4.1). From Figure 4.16, it is clear that calculations mimic fairly well the differences observed between the experimental Co XAS spectra for the two temperatures. On the basis of the LFM calculations, it can therefore be concluded that the electronic structure of Co^{II}_{HS} ions is the same in the 300 K paramagnetic phase and in the 4 K photo-induced phase. This is in agreement with the K edge XAS and XRD results reported by Sekine *et al.* in the square molecules of FeCo PBA where they confirmed that the electronic structure of the low temperature light-induced state is similar to the one of the high temperature state.[58,59]

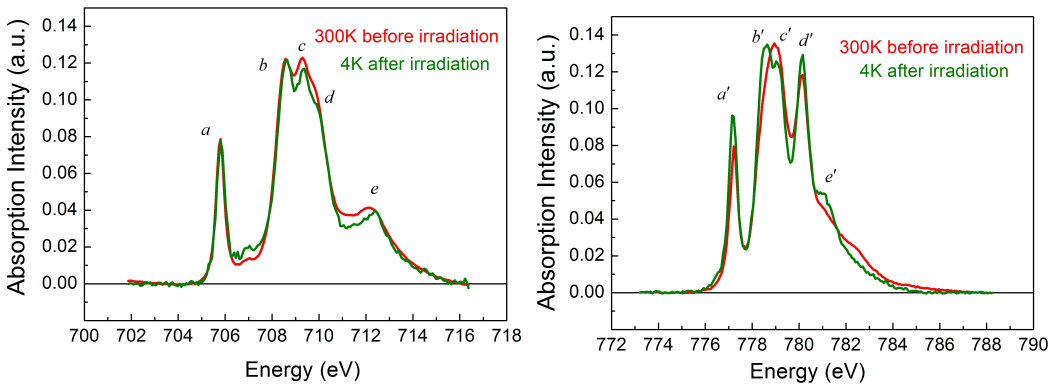

Figure 4.7 – XAS spectra measured at the Fe (left) and Co (right) L_3 edge at 300 K before irradiation (red line) and at 4 K after irradiation (green line).

In Figure 4.6, the XMCD-detected magnetization curves for Fe and Co ions are superimposed. Within the uncertainty on the experimental measurement there is no hint for an antiferromagnetic coupling between Fe^{III}_{LS}—Co^{II}_{HS}, contrary to what is usually sug-

gested.[28,49,51] Since measurements have been performed at 2 K, our results indicate that the exchange coupling constant J between Fe and Co ions is such that $J/k_B < 2$ K.

In order to gain more information, the XAS and XMCD signals from the two precursors (samples **2** and **3**, see experimental section) of sample **1** were recorded at 4 K and in an external magnetic induction of 6.5 T. The Fe $L_{2,3}$ edges for samples **1** and **2** are very similar (Figure 4.14). One observes the same series of spectral features, with mainly peak **a** that is characteristic of Fe^{III}_{LS} and shoulder **e** that is a signature of Fe surrounded by 3 cyanido ligands. The intensity of features **b**, **c** and **d** are rather different as can be expected from the presence of the (NC–Co) bond in sample **1**. The XMCD features are also very similar and almost homothetic for both samples. If one focuses on features **a** in the XAS and α in the XMCD, the ratio α/a is 66 % for sample **1** while it is 70 % for its precursor sample **2**.[82] For samples **1** and **3**, the situation is somewhat different at the Co L_3 edge. Indeed the local organization of Co ions is very different in these compounds, so that both Co XAS spectra are quite different (Figure 4.15). On the opposite, both Co XMCD signals present some similarity but for some intensity ratio at the L_3 edge and rather large differences at the L_2 edge. The general shape is in agreement with what is the expected for a Co^{II}_{HS} ion in 6-fold coordination. One then concludes that at 6.5 T, the magnetization of Fe and Co ions in sample **1** are quite similar to the magnetizations for isolated paramagnetic ions, as it is the case in samples **2** and **3**. This again confirms that if an antiferromagnetic coupling does exist between Fe and Co in the pair **1**, then the coupling constant has to be well below 2 K.

4.2.6 Conclusion

The electronic and magnetic structures of Fe and Co ions in a dinuclear photomagnetic PBA have been measured for the first time in an element selective way. Using a combination of XAS and XMCD spectroscopies supported by LFM calculations, it is proved unambiguously that **(i)** the 300 K phase and the light-induced excited state at 4 K are built from Fe^{III}_{LS}—Co^{II}_{HS} paramagnetic pairs and **(ii)** the 100 K phase is built from Fe^{II}_{LS}—Co^{III}_{LS} diamagnetic pairs. Both paramagnetic phases at 300 K and at 4 K after light irradiation are identical, with no apparent reorganization of the local structure around either Fe or Co. In the paramagnetic pairs at 2 K and under an external magnetic induction of 6.5 T, both Fe and Co ions exhibit a rather large orbital magnetic moments: it is equal to 0.31 μ_B for Fe and 0.32 μ_B for Co. In the case of Fe, the orbital magnetic moment is likely to be larger than the spin magnetic moment as for **FeTp** precursor, i.e. sample **2**.[82] The total magnetic moment of Co is larger than the one of Fe and we do not observe any antiferromagnetic coupling between Fe and Co, indicating that the coupling constant is likely well below 2 K. The light induced excited state is relaxed at 50 K, so that at temperatures below 50 K sample **1** present a bistability that could be driven by an appropriate application of light and temperature. XMCD measurements at very low temperature (below 500 mK)[54] might help further characterizing the sign and magnitude of the magnetic coupling between Fe and Co ions.

Acknowledgements

This work was supported by the Centre National de la Recherche Scientifique (CNRS, France), the Ministère de l'Enseignement Supérieur et de la Recherche (MESR, France), the Aquitaine region, the Institut Universitaire de France (IUF) and partially funded by ANR (ANR-10-BLAN-0712; ANR-09-BLAN-0175; ANR-12-PDOC-0038), and GDR MCM2. The staff from SOLEIL, SLS and ESRF is acknowledged for operating the synchrotron sources and beamlines. We are glad to acknowledge Dr. Armin Kleibert for his technical support on the SIM beamline. We also thank Bernard Muller (IPCMS, Strasbourg) for instrumental developments on the French TBT dilution cryomagnet.

4.3 Supporting Information of Paper II

4.3.1 Reversibility of the electron transfer process

The reversibility of the photo-induced electron transfer process has been checked by measuring XAS spectra at the Fe and Co L_3 edges at 100 K and 300 K, before and after the laser irradiation as shown in Figures 4.8 and 4.9.

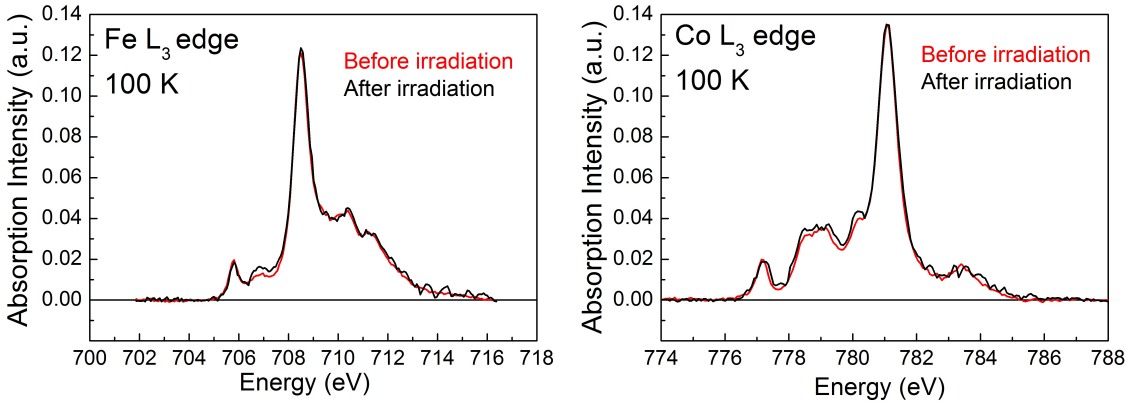

Figure 4.8 – Reversibility of the electron transfer process: XAS at the Fe and Co L_3 edge before (red line) and after irradiation (black line) at 100 K and $\boldsymbol{B} = 2$ T.

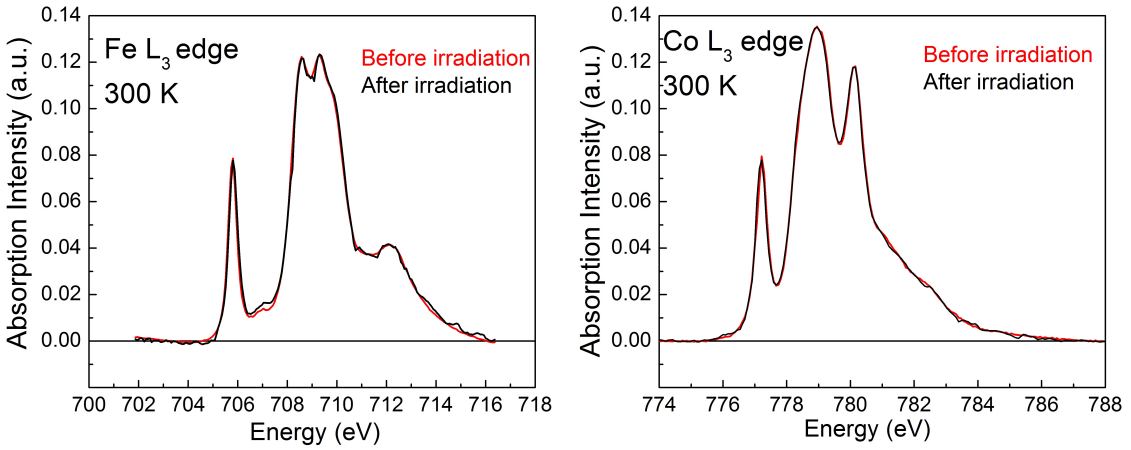

Figure 4.9 – Reversibility of the electon transfer process: XAS at the Fe and Co L_3 edge before (red line) and after irradiation (black line) at 300 K and $\boldsymbol{B} = 2$ T.

4.3.2 Fe and Co XAS spectra at K edges

For completeness we have also recorded the Fe and Co K edges in sample **1** at 300 K and at 4 K, as shown in Figure 4.10. When the temperature is lowered, the main rising edge of both Fe and Co K edges are slightly shifted, to lower energy (≈ 0.8 eV) for Fe, to higher energy (≈ 2.2 eV) for Co. These changes are compatible with a reduction of Fe and an oxidation of Co when the temperature is lowered.

In addition, the features at high energy for the Fe K edge are hardly modified whereas the shape resonances for Co K edge at 7742 eV and 7770 eV are shifted by several electron-Volts to higher energy. This indicates that the local environment around Fe is not much modified while the coordination sphere of Co is strongly shortened, as it is expected for

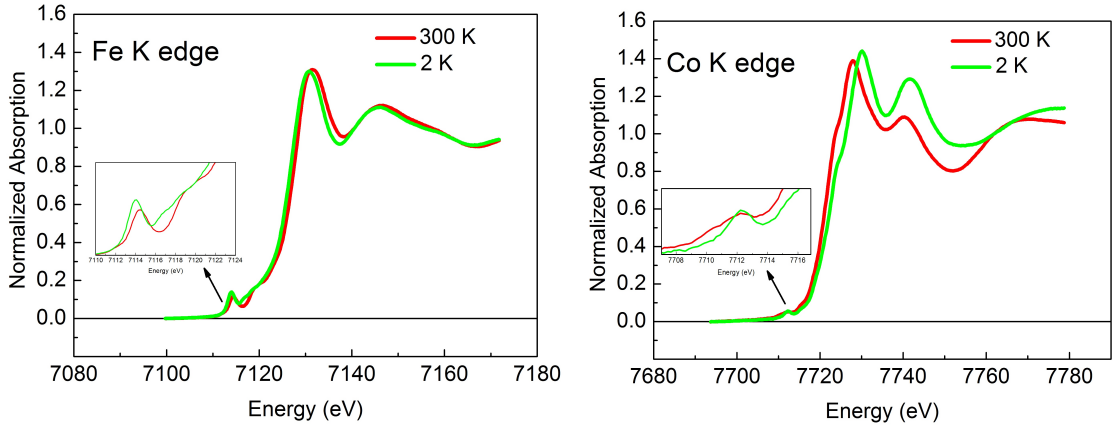

Figure 4.10 – Experimental K edge XAS spectra of Fe (left) and Co (right) at 300 K (red line) and 2 K (green line). The insets display the zoom view in the pre-edge region.

a high spin to low spin conversion. These various features are fully compatible with the expected temperature-induced electron transfer between a high temperature Fe^{III}_{LS} and Co^{II}_{HS} paramagnetic pair and a low temperature Fe^{II}_{LS} and Co^{III}_{LS} diamagnetic pair. A closer look to the pre-edge region confirms the Co^{II}_{HS} to Co^{III}_{LS} conversion. This is best seen by comparison with previously published spectra by Poneti et al.[125] As, well resolved distinct features of pre-edge cannot be compared by spectra reported by Sekine *et al.*[58,59] Only a few reference spectra for Fe K edge have been published with good enough resolution in order to help for the identification of Fe^{III}_{LS} and Fe^{II}_{LS}.[138]

The difference signal between the 300 K and the 2 K spectra is plotted (green solid line) in Figure 4.12 for both Fe and Co K edges. In order to check for light induced photoconversion at 4 K, sample **1** was irradiated for three hours with an intense white light delivered by a tungsten halogen lamp.

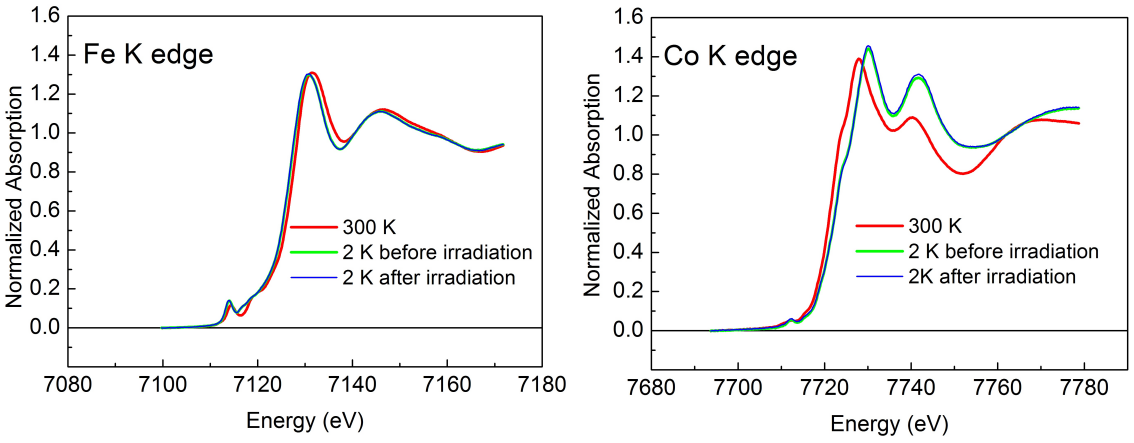

Figure 4.11 – Experimental K edge XAS spectra of Fe (left) and Co (right) at 300 K (red line), 2 K before laser irradiation (green line) and 2 K after laser irradiation (blue line).

The difference between the spectra before and after the white light irradiation is reported in Figure 4.12. The thermal-induced difference signal (green line) comes from the subtraction of XAS spectrum at 300 K and XAS spectrum at 2 K before laser irradiation. The light-induced difference signal (red line) comes from the subtraction of XAS spectrum in light-induced state at 2 K and XAS spectrum at 2 K before light irradiation. The

percentage of the light-induced and thermal-induced electron paramagnetic species have been calculated by taking the peak-to-peak ratio at the difference spectra. One observes that the light-induced transformation has roughly the same shape as the thermal-induced transformation for both Fe and Co K edges. One also notices that the light-induced conversion amounts to around 7 % to 8 % of the thermal-induced conversion, so that we can consider that the present photoconversion induced by the tungsten halogen lamp is not very efficient.

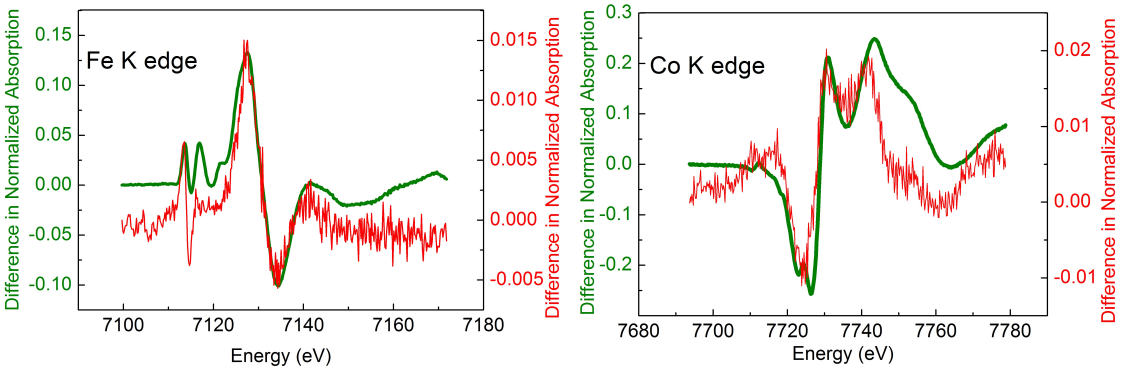

Figure 4.12 – Difference in Normalized Absorption at the Fe (left) and Co (right) K edges after thermal-induced (green line) and light-induced (red line) conversion.

This is most likely due to some simple geometrical factor since the lamp was rather far away (≈1 m) from the sample and the exposition time was 4 times shorter than in Koumousi *et al.*[49]

The reversibility of the electron transfer process after temperature and light-irradiation treatment is complete as can be seen from Figure 4.13.

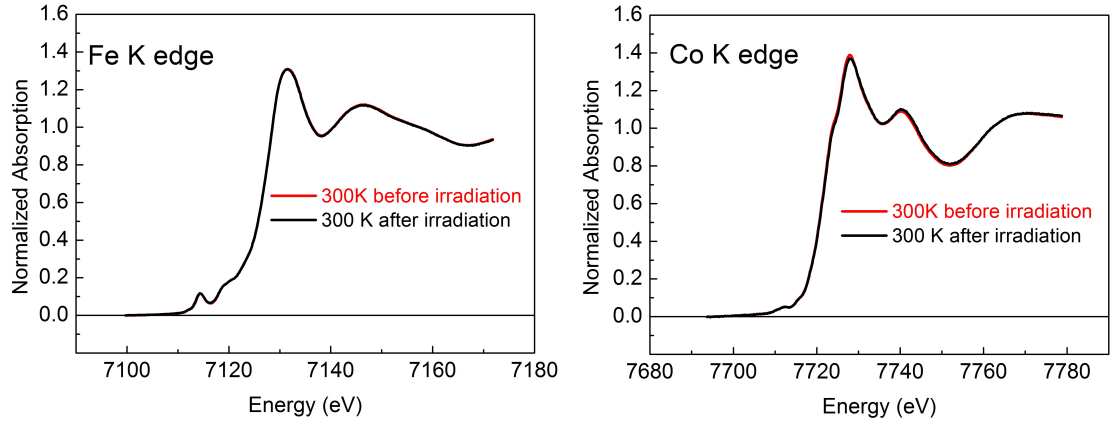

Figure 4.13 – Experimental Fe and Co K edge normalized XAS at 300 K before (red line) and after irradiation (black line).

4.3.3 Comparison of XAS and XMCD for sample 1 with those of the Fe and Co precursors

The comparison of the Fe in sample **1** and **2** (Figure 4.14) and the comparison of Co in sample **1** and **3** (Figure 4.15) is presented in the discussion section.

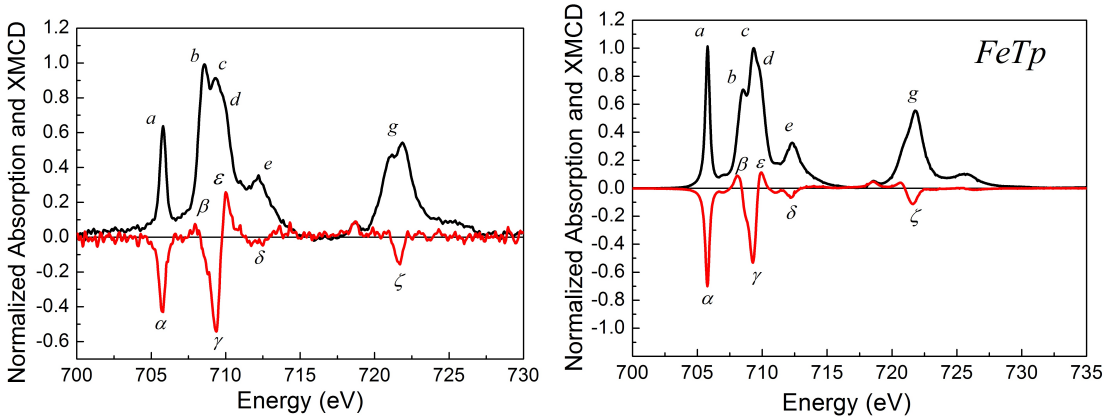

Figure 4.14 – Experimental XAS (black line) and XMCD (red line) spectra at the Fe $L_{2,3}$ edges in sample **1** (left) and sample **2** (right) at $T = 4$ K and $\boldsymbol{B} = 6.5$ T.

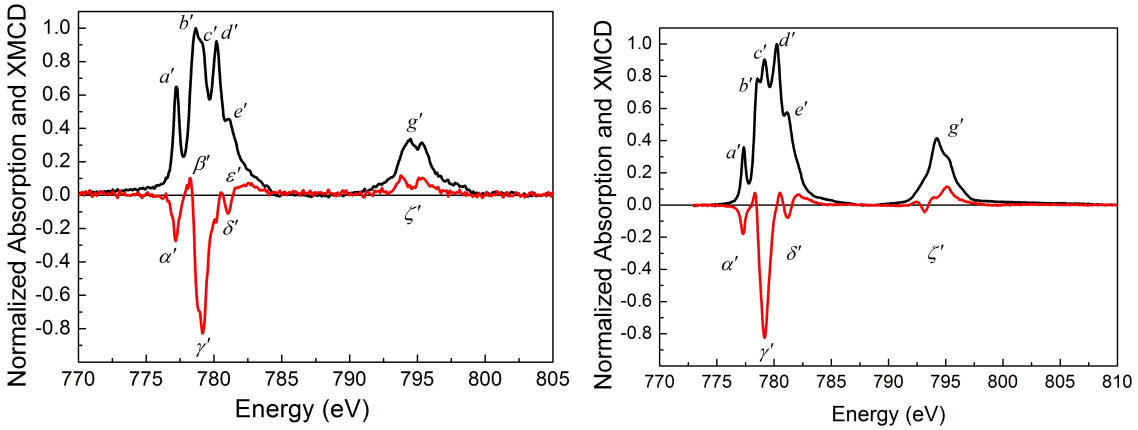

Figure 4.15 – Experimental XAS (black line) and XMCD (red line) spectra at the Co $L_{2,3}$ edges in sample **1** (dinuclear complex, left) and sample **3** (Co precursor of **1**, right) at $T = 4$ K and $\boldsymbol{B} = 6.5$ T.

4.3.4 Comparison of experimental and theoretical Co $L_{2,3}$ edges XAS spectra at 300 K and at 2 K.

The comparison of experimental and theoretical XAS at Co L_3 edge presented in Figure 4.16 is described in discussion section.

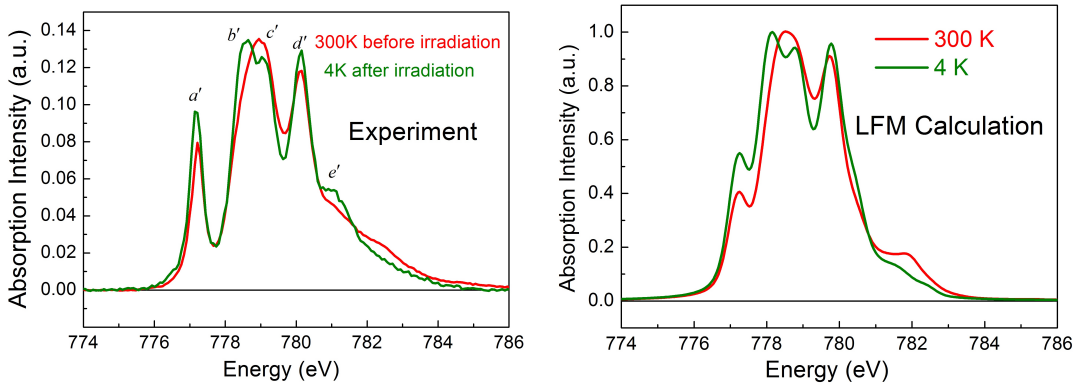

Figure 4.16 – Left: Experimental Co L_3 edge at 300 K before irradiation (red line) and at 4 K after irradiation (green line) (left). Right: Spectra calculated in the Ligand Field Multiplet (LFM) approach.

Table 4.1 – Parameters used in the Ligand Field Multiplet simulations for $\boldsymbol{B}$ = 6.5 T at T = 4 K and 300 K. All energies are given in eV (1 eV = 11605 K), κ is dimensionless. The $3d$ and $2p$ spin-orbit coupling constants are the atomic values: ζ_{3d} = 0.028 eV and ζ_{2p} = 9.750 eV.

$10Dq$	$D\sigma$	$D\tau$	κ
1.0	0.043	0.02	0.7

4.3.5 Linear combination of the XAS spectra

In Figure 4.17 an example is presented to explain how the linear combination is used to get the amount of paramagnetic species at a given temperature. To extract the Co^{II}_{HS} amount at T = 10 K, the selected references for Co^{III}_{LS} and Co^{II}_{HS} are the experimental Co XAS spectra at 4 K after laser irradiation and at 100 K respectively. These reference spectra are considered as the limiting compositional cases corresponding to 100% and 0% Co^{II}_{HS}.

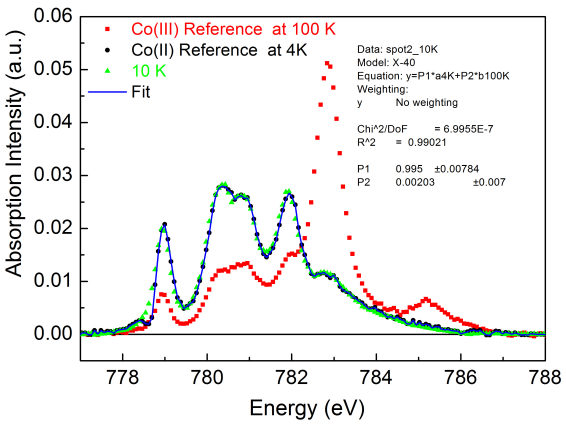

Figure 4.17 – The linear combination (blue line) of the reference XAS spectra for Co^{III}_{LS} at 100 K (red line) and Co^{II}_{HS} at 4 K after laser (black line) for selected Co XAS at T = 10 K to fit (green line).

4.4 XAS and XMCD investigations of complex 2·2DMF at Fe and Co *K* edges

The present XAS and XMCD study at the Fe and Co *K* edges is aimed to follow the thermal- and light-induced electron transfer in **2**·2DMF. Since **2**·2DMF needs to be preserved from desolvation to maintain its properties, it cannot be studied easily under UHV. The sample needs to be inserted in a sealed cell and this can be done for the measurements at the *K* edges but not yet at $L_{2,3}$ edges. XMCD at *K* edges can give information on the Co and Fe magnetic interaction in the photo-induced excited spin state but since the analysis of the *K* edges requires involved theoretical developments, it is usually difficult to extract quantitative magnetic information. The molecular structure of **2**·2DMF is presented in Figure 4.18.[8] In addition, we have carried out a study on the Fe and Co precursors. The XMCD signals from **2**·2DMF and from its Fe precursor display distinct modifications in intensity and shape. The comparison of the amplitude and spectral shape of XMCD signals in precursors and **2**·2DMF complex gives a deeper insight on the magnetic contributions of Fe^{III}_{LS} and Co^{II}_{HS} ions.

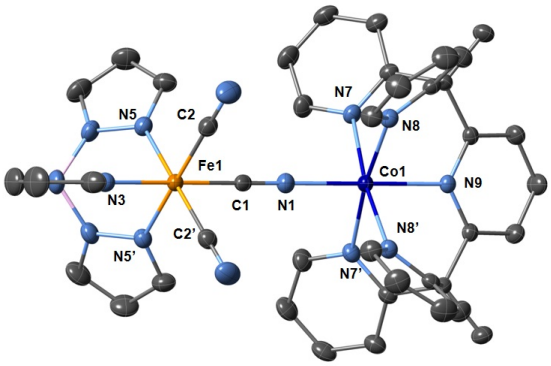

Figure 4.18 – The molecular structure of complex (**2**·2DMF)[(Tp)Fe^{III}(CN)$_3$$Co^{II}$PY5Me$_2$](PF$_6$)·2DMF. All anions, lattice solvents and hydrogen atoms are omitted for clarity. Fe, Co, N, C and B atoms are indicated in orange, dark blue, light blue, grey and pink respectively.

4.4.1 Experimental section

4.4.1.1 Sample preparation

The FeCo PBA dinuclear complex **2**·2DMF (DMF = N,N-dimethylformamide) was synthesized by following the procedure developed by Koumousi *et al.*[8] The compound has been characterized by the standard magnetometric techniques and elemental analyses.[8] The Fe and Co precursors have the chemical formulae (Bu_4N)[TpFe^{III}(CN)$_3$] and [(PY5Me$_2$)Co^{II}(H_2O)](BF_4)$_2$ and are referred in this section as **Fe precursor** and **Co precursor**.

4.4.1.2 XAS and XMCD measurements

Fe and Co *K* edges XANES and XMCD experiments were performed at ID12 beamline at ESRF. The crystals of **2**·2DMF were immersed in NVH oil and protected with kapton foil in the cell represented in Figure 4.19. At the *K* edges the dichroic signal is small and

barely larger than 0.1% of the absorption edge. In 3*d* transition metal ions and in the electric dipole approximation, XMCD signal at *K* edges cannot come from the presence of spin-orbit interaction on the core-hole since it is a 1*s* core-hole. XMCD signal then comes from the spin-orbit coupling acting on the 4*p* levels in the continuum. This spin-orbit coupling is very weak and thus XMCD signals at *K* edges are small compared to XMCD signals at $L_{2,3}$ edges.[138,139] Therefore, ID12 beamline has been carefully optimized for polarization dependent XAS measurements with incident X-rays in the energy range of 2-15 keV. The production of circularly polarized X-rays is achieved by using APPLE-II or HELIOS-II undulators.[129,130,140] The beamline is equipped with a UHV compatible Si(111) double crystal monochromator. The XMCD measurements can be performed with magnetic induction as large as 17 T. The details of the beamline optics and the working end station can be found in the work by Rogalev *et al.*[140] All spectra are collected in the temperature range of 300 K to 2 K. At 2 K, the sample is irradiated by a laser ($\lambda = 940$ nm, P = 5 mW) during 8 hours. In the photo-induced state, XAS and XMCD at Fe and Co *K* edges were recorded.

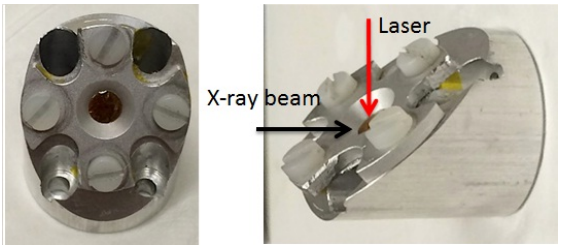

Figure 4.19 – The front (left) and side (right) views of the sample holder where the crystals of **2**·2DMF are placed under the kapton foil.

4.4.1.3 Element-specific XANES study

K edge XANES (X-ray absorption near edge structure) is sensitive to the chemical and crystallographic environment, thus any change induced in the structure due to the light and/or the temperature is manifested in the XANES region. The very first electron-volts in the XANES region of the *K* edge can be related to changes in oxidation state, site symmetry, covalency or the electronic structure of the absorbing ion. It can be noticed that *K* pre-edges and $L_{2,3}$ edges of 3d transition metal ions can give similar information because the features involve transitions to the 3d orbitals. However, $L_{2,3}$ edges have large intensities due to the 2p $\rightarrow$ 3d electric dipole (E1) transitions whereas *K* pre-edges result from quadrupole allowed (E2) 1s $\rightarrow$ 3d and electric dipole allowed 1s $\rightarrow$ 4p contributions which arises from the 4p-3d low symmetry mixing.[96,138,141]

4.4.2 Thermal and Photo-induced electron transfer

In a first step, XANES spectra at 300 K and at 2 K were recorded before irradiation to follow the thermal-induced electron transfer. At 300 K, Fe *K* edge XAS has intense absorption maximum at 7131.7 eV (E1 allowed 1s $\rightarrow$ 4p transitions) and a weak pre-edge feature (E2 allowed 1s $\rightarrow$ 3d transitions) at 7114.5 eV. For Co, the maximum in *K* edge absorption is observed at 7727.8 eV and a pre-edge at 7712.1 eV (fig 4.20). The absorption

edge of Fe displays a broad peak whereas for Co this peak is sharper in comparison. The large intensity of Fe pre-edge feature compared to Co, is due to the easy p–d mixing in ligand field around Fe^{III}_{LS}-sites and to large π back bonding.[138,141]

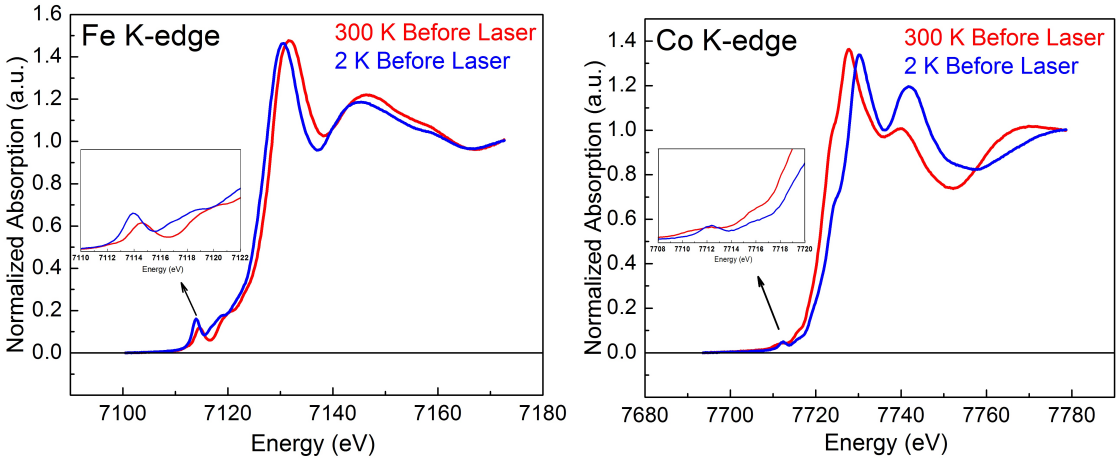

Figure 4.20 – Experimental Fe and Co K edges normalized XAS spectra at 300 K before laser (red line) and 2 K before laser (blue line). The insets display the zoom view of the pre-edge region.

When comparing the Fe and Co K edges at 300 K and 2 K, one observes that the absorption maximum for Fe at 2 K is shifted by ≈1.2 eV to lower energy (7130.5 eV) while the Co K edge at 2 K is shifted by ≈2.4 eV to high energy (7730.2 eV). This shift in the energy of absorption maxima at both edges is characteristic of the change in oxidation state for Fe ions from Fe^{III}_{LS} to Fe^{II}_{LS} and for Co ions from Co^{II}_{HS} to Co^{III}_{LS}.[14,21,30,142] Hence, it confirms the transition from the paramagnetic state to the diamagnetic one due to thermal-induced electron transfer in **2**·2DMF. The XANES part of the Co K edge spectra is also modified during the transitions, for instance, a significant decrease in intensity at the shoulder in the main rising edge at 7724 eV is observed. In the high energy region, the first EXAFS oscillations between 7146.5 eV and 7170 eV are not modified at Fe K edge, whereas, noticeable changes are observed in the shape resonance region in Co K edge XANES spectra between 7740.2 eV and 7770 eV. This is attributed to the change in environment around Co since a change in Co spin state from high spin to low spin significantly shortens the Co coordination sphere.[23,31,143] The change from Fe^{III}_{LS} to Fe^{II}_{LS} does not modify much the distances between Fe and its neighbors so that the first shape resonance is only slightly modified. These structural modifications have been confirmed by X-ray diffraction measurements in PBA systems.[23]

At 2 K, we irradiated the sample with λ = 940 nm laser (P = 5 mW) for 8 hours and the XAS spectra were recorded at Fe and Co K edges (Fig 4.21). Both pre-edge regions and XANES regions from the K edges recorded at 300 K and at 2 K after laser irradiation superpose nicely. This confirms that the Fe ions have the same oxidation states at 300 K and in the paramagnetic metastable state at 2 K with quite similar environments.[21] The same is also true for Co ions. For comparison of thermal and light-induced electron transfer, we have plotted Fe and Co K edge XANES at 300 K, at 2 K before irradiation and at 2 K after irradiation in Figure 4.22. In a next step, we have warmed the sample back to 300 K to check for the reversibility of the electron transfer process. Figure 4.23

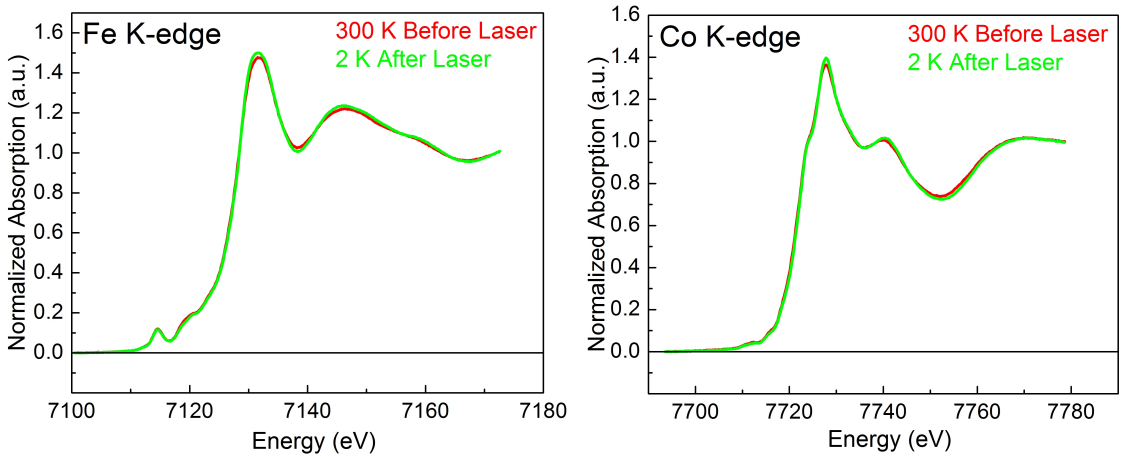

Figure 4.21 – Experimental Fe and Co K edge normalized XAS spectra at 300 K before laser (red line) and at 2 K after laser (green line).

compares the Fe and Co K edge XANES spectra at 300 K before and after light irradiation. The spectra superimpose completely, thus it confirms that the electron transfer process is indeed completely reversible.

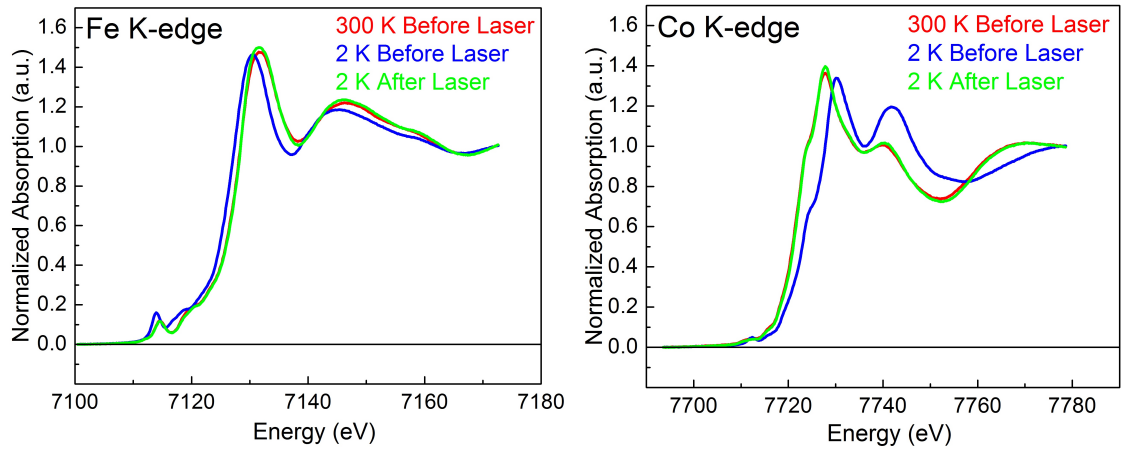

Figure 4.22 – Experimental Fe and Co K edge normalized XAS spectra at 300 K before laser (red line), at 2 K before laser (blue line) and at 2 K after laser (green line).

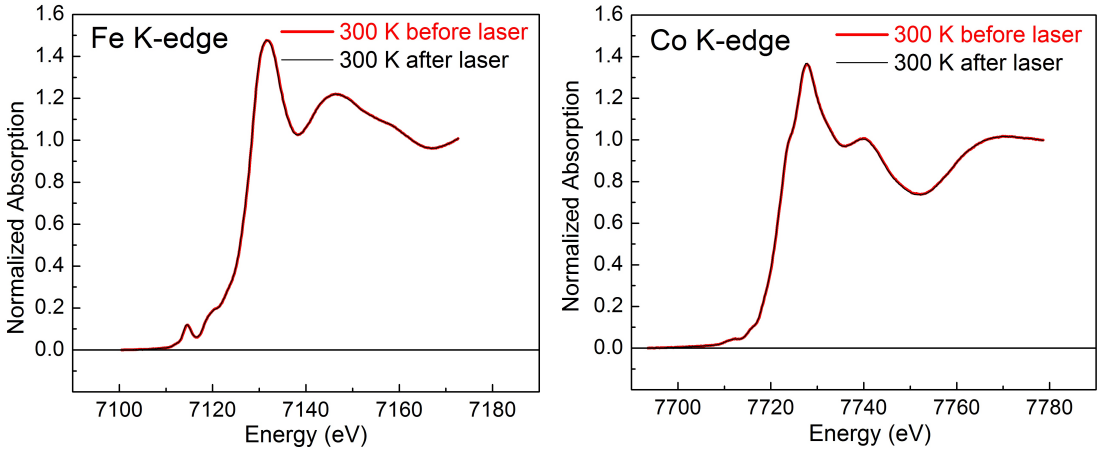

Figure 4.23 – Experimental Fe and Co K edge normalized XAS spectra at 300 K before laser (red line) and after laser (black line).

4.4.3 XMCD at Fe and Co K edges

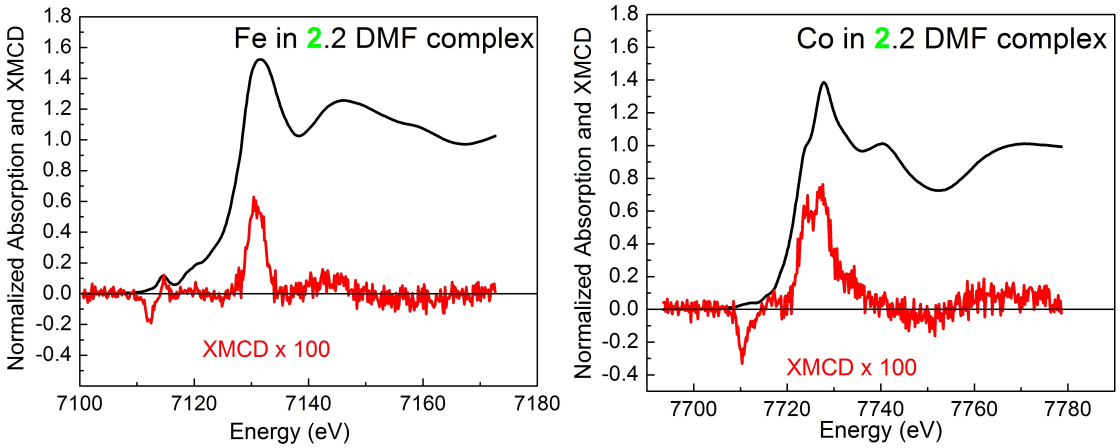

Figure 4.24 – Experimental Fe and Co K edge normalized XAS spectra (black line) and XMCD signals (red line) at 2 K after white light irradiation under $\boldsymbol{B}$ = 17 T.

The normalized XMCD spectra display characteristic peak structures, at the absorption edge of both ions, located at 7130 eV and 7730 eV respectively (figure 4.24). The Fe XMCD signal contains two components at the pre-edge with a derivative-like shape and one component at the main rising edge. The Co XMCD signal has only one component at the pre-edge and one component at the main rising edge. From the previous analysis by Champion *et al*. one could say that the Fe and Co magnetic moments points in the same direction with respect to the magnetic induction.[51] The positive K edge XMCD peak for Fe can be attributed to the magnetization of the Fe $4p$ levels but not much can be said about the Fe $3d$ levels.[51]

4.4.4 XMCD detected magnetization curves at Fe and Co K edges

In a next step, XMCD detected magnetization curves are recorded at 2 K after laser irradiation as a function of magnetic induction by setting the monochromator at E = 7727 eV and E = 7131 eV for Co and Fe respectively.

Figure 4.25 shows the corresponding magnetization curves. Both Fe and Co XMCD magnetization signals have similar shape and can be superimposed. The magnetization does not seem to be fully saturated at 17 T. Interestingly if the Fe and Co XMCD features at 7131 eV and 7727 eV can be said to be proportional to the $3d$ magnetizations of Fe and Co, Figure 4.25 would tend to prove that there is no antiferromagnetic coupling between Fe and Co at 2 K. Whether there is a ferromagnetic coupling between Fe and Co ions or whether the two paramagnetic ions are similarly polarized by the magnetic induction remains still a matter of debate that cannot be solved by the present set of measurements.

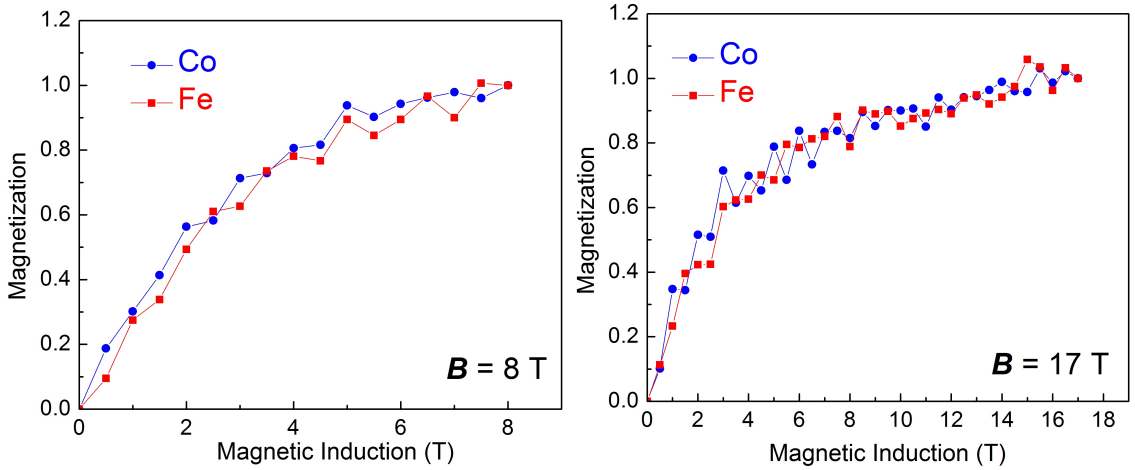

Figure 4.25 – Experimental Fe (red line) and Co (blue line) K edge normalized magnetization curves at E = 7131 eV and E = 7727 eV respectively recorded at 2 K after irradiation under $\boldsymbol{B}$ = 8 T (left) and $\boldsymbol{B}$ = 17 T (right).

4.4.5 Fe and Co Precursors of 2·2DMF dinuclear complex

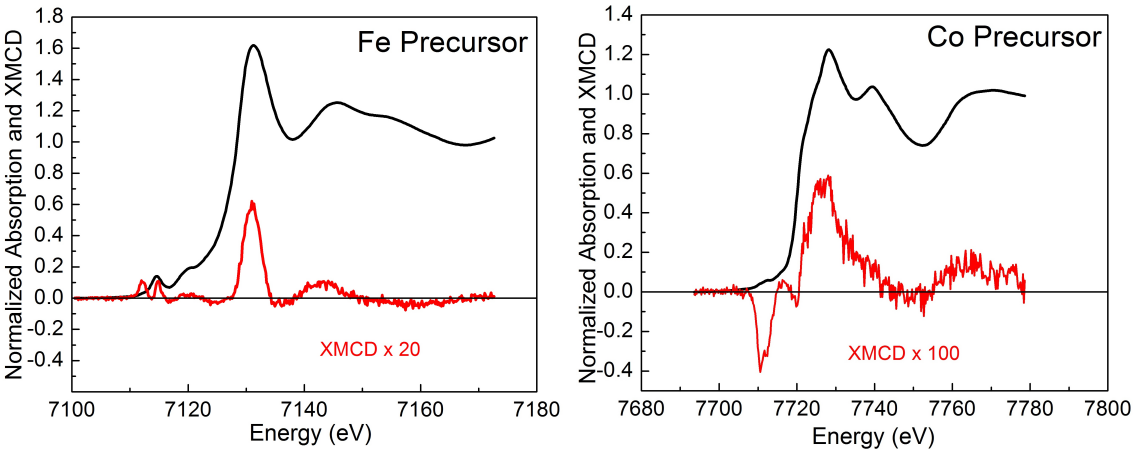

Figure 4.26 – Experimental Fe (left) and Co K edge (right) normalized XAS (black line) and XMCD (red line) spectra for precursors at 2 K.

The XAS and XMCD spectra recorded for Fe and Co precursors at 2 K are displayed in Figure 4.26. The XAS spectra show the absorption maxima at 7131.1 eV and 7728 eV for Fe and Co respectively. The pre-edge features are at the energy 7114.5 eV and 7711.6 eV for Fe and Co K edges respectively. One can observe that the intensity of the Fe XMCD signal is 5 times larger compared to the XMCD signal of Fe in complex **2**·2DMF. Another main difference is the shape of the XMCD at the Fe pre-edge. For complex **2**·2DMF it has a derivative like shape whereas it is a two lobbed positive signal for the Fe precursor. At the Co K edge, the XMCD signals from both the Co precursor and **2**·2DMF are similar in intensity and shape except for a slight reduction of the XMCD signal on the pre-edge of **2**·2DMF. The XAS and XMCD signals from complex **2**·2DMF and its precursors are plotted in Figures 4.27 and 4.28.

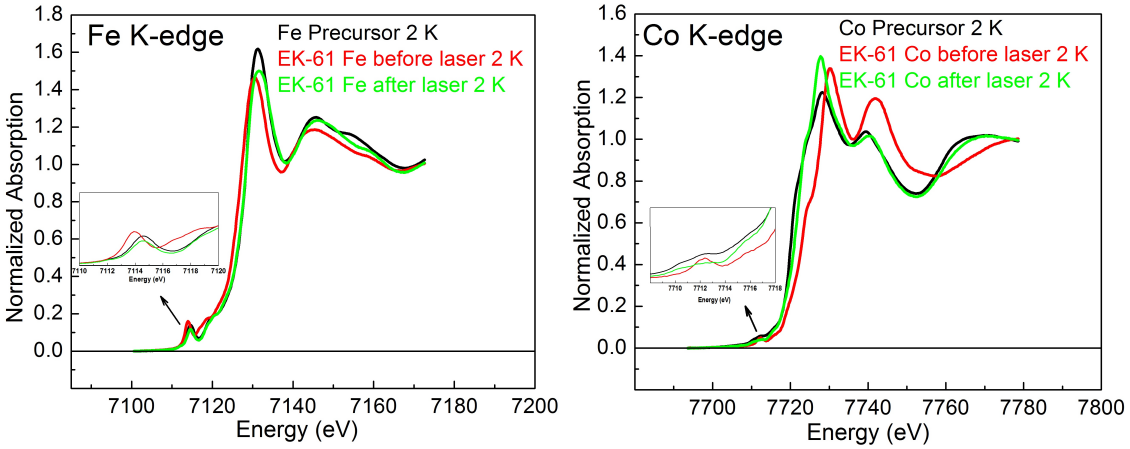

Figure 4.27 – Comparison of experimental Fe (left) and Co K edge (right) normalized XAS (black line) spectra for precursors at 2 K (black) and 2.2·DMF dinuclear complex at 2 K before irradiation (red line) and after irradiation at 2 K (green line). The insets display the zoom view of the pre-edge region.

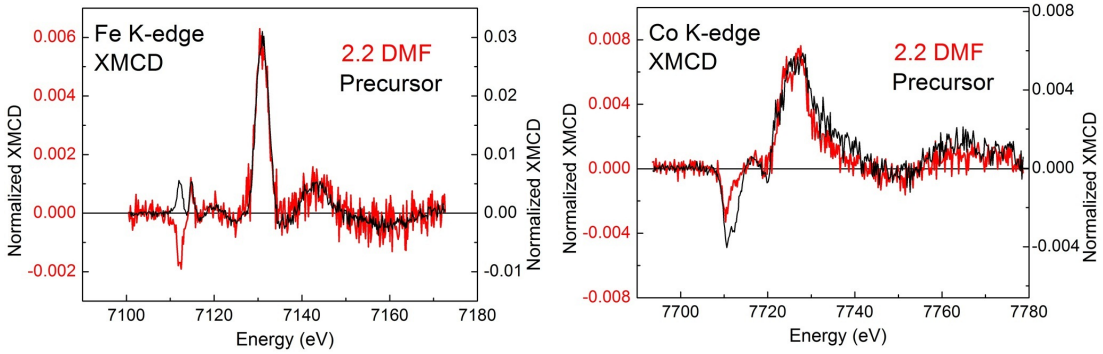

Figure 4.28 – Comparison of the normalized XMCD spectra at the K edge of Fe (left) and Co (right) for **2**.2DMF dinuclear complex (red line) and corresponding precursors (black line) at $T = 2$ K after irradiation under $\boldsymbol{B} = 17$ T.

4.4.6 Thermal- and light-induced transitions in 2·2DMF complex followed by XAS, XMCD and SQUID magnetometry

The thermal-induced electron transfer and the relaxation of the photo-induced metastable state have been recorded from XAS as a function of temperature and are presented for Co in Figure 4.29 and for Fe in Figure 4.30. To perform such measurements, the monochromator is set at 7114 eV for Fe K edge (i.e. the pre-edge feature) and at 7726 eV for Co K edge (i.e. the maximum of the main rising edge). The XAS measurements are compared with the SQUID measurements where the transitions were followed by the variations of the magnetic susceptibility. Both XAS and SQUID provide rather similar behaviors with noticeable differences for the thermal-induced transition. Both Fe and Co K edges show a transition at a temperature 5 K lower than the one found from SQUID (≈90 K). The thermal hysteresis measured by XAS is also slightly wider compared to SQUID and this might be due to the slightly different sweeping rate and to different thermalization rates for XAS measurements. The relaxation of the photo-induced metastable state measured with XAS and SQUID are quite similar with a relaxation temperature close to ≈ 50 K. The relaxation temperature is defined as the temperature for which more than 95% of paramagnetic pairs have been converted to diamagnetic ones.

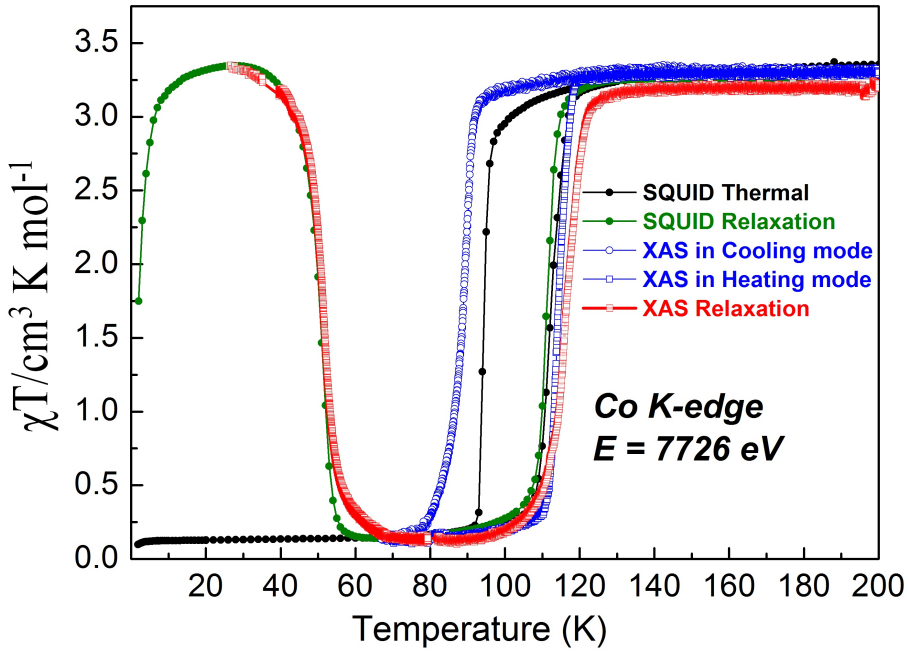

Figure 4.29 – Comparison of the results obtained from SQUID magnetometry and from XAS spectra recorded at the maximum of the Co K edge difference at 7726 eV: χT versus T plots for **2**·2DMF (SQUID) from 200 to 1.8 K at 0.1 T in cooling mode with 0.3 K/min (in black) and from 1.8 K to 200 K (in green) at 1 T and 0.8 K/min in heating mode after laser irradiation (λ = 940 nm) at 10 K; thermal dependence of the normalized XAS data in Co K edge (E = 7726 eV) in cooling mode from 200 to 70 K at 2.8 K/min (blue circles), in heating mode from 70 K to 200 K at 1.9 K/min (blue squares), relaxation after laser irradiation (in red) in heating mode from 26 to 80 K (0.23 K/min) and from 80 to 200 K at (4.7 K/min). The SQUID data are taken from the thesis by E.S. Koumousi.[8]

4.5 Summary of Chapter 4

In this chapter we have presented XMCD results on two photomagnetic Fe/Co dinuclear complexes, **1** and **2**·2DMF, which exhibit thermal- and light-induced electron transfer properties. This is the first XAS and XMCD study which reports on the metal-to-metal electron transfer between Fe and Co in photo-induced state in solid state as well as in solution. The reversibility of electron transfer as detected by XAS has been confirmed for both complexes. The study of complex **1** has been performed at the Fe and Co $L_{2,3}$ and provided information on the orbit and spin magnetic moments carried by the 3d electrons. The study of complex **2**·2DMF has been performed at Fe and Co K edges for which only qualitative results can be obtained. For both complexes, one could not observe any antiferromagnetic coupling between Fe and Co at 2 K in the photomagnetic state. From XMCD detected magnetization curves at $L_{2,3}$ edges for **1** and K edges for **2**·2DMF both magnetization for Fe and Co ions superimpose rather nicely. Whether the Fe and Co ions are ferromagnetically coupled or not could not be determined from our measurements. These results have to be compared with those obtained by Koumousi *et al.*[8,49] From Champion *et al.*, a fingerprint analysis of the XMCD signals at Fe and Co K edges had been performed.[51] The comparison of the XMCD signal at the Fe K edge from complex **2**·2DMF and from the Fe precursor clearly indicates how it is difficult to extract the magnetization of the 3d shell from the XMCD signals. Although the theoretical

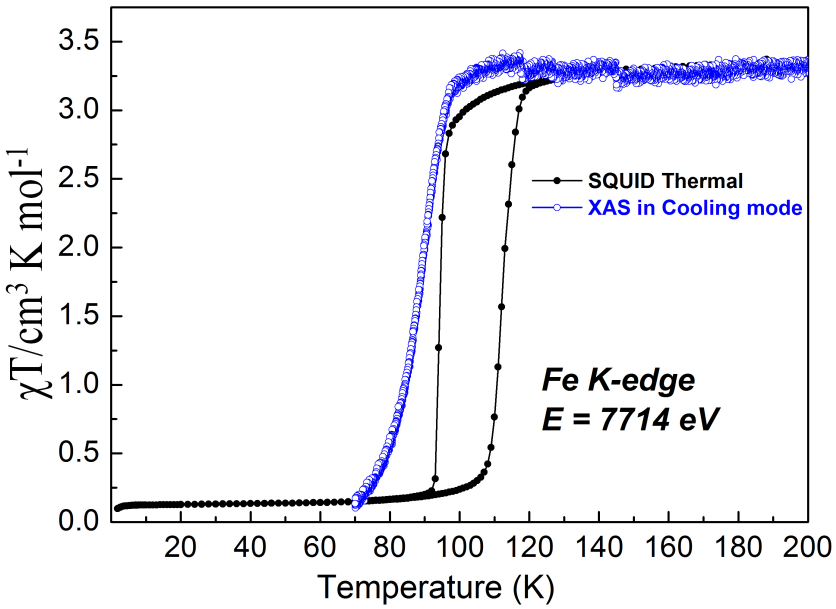

Figure 4.30 – Comparison of the SQUID results with the XAS recorded at the maximum of the Fe K edge difference at 7714 eV: χT versus T plots for **2**·2DMF (SQUID) from 200 to 1.8 K at 0.1 T in cooling and heating mode with 0.3 K/min (in black), thermal dependence of the normalized XAS data in Fe K edge (E = 7714 eV) in cooling mode from 200 to 70 K at 2.8 K/min (blue circles). The SQUID data are taken from the thesis by E.S. Koumousi. [8]

framework for the interpretation of the XMCD signals at $L_{2,3}$ edges is well mastered within the Ligand Field Multiplet approach developed by Theo Thole,[125,141] the theoretical framework for the XMCD at K edges is still in its infancy and heavy developments are still required.

Chapter 5

Probing the Magnetic interaction in tridimensional Fe/Co Prussian Blue Analogues

Contents

5.1 Introduction

After the first example of photo-induced magnetization reported by Sato *et al.*[6] in Fe/Co PBA, there has been a great deal of efforts to understand photomagnetism as can be seen from the recent review by Aguilà and coauthors.[9] However, some aspects remain elusive in the understanding of the photomagnetism in these systems. One of the most important questions concerning the nature of the magnetic interaction between the metal centers in Prussian Blue analogues is not fully answered, i.e. whether the Fe–Co interaction is ferromagnetic or antiferromagnetic and how does this interaction depend on the structure of the Fe/Co PBA. To bring information on this question, Fe/Co based PBA have been explored by various techniques[9] such as for instance SQUID magnetometry,[7,18,28] X-ray diffraction,[142,143] Neutron diffraction,[144] and XMCD.[51,57,59,68,136] The ground state is composed of diamagnetic Fe^{II}_{LS}–CN–Co^{III}_{LS} species which are converted into paramagnetic Fe^{III}_{LS}–CN–Co^{II}_{HS} ones upon irradiation because of a metal-to-metal electron transfer. The conventional characterization of the photo-induced state is not possible by $\chi_M T$ because (*i*) the irradiation of the sample is not necessarily complete and the mass of the converted phase is unknown and (*ii*) the thermal relaxation of the photo-induced state at low temperatures imposes a too limited range of temperature for the analysis of the $\chi_M T$ curves.

The XMCD technique is capable of tracking the exact orientation of the magnetization of the absorbing atom with respect to the X-ray propagation vector. The local orientation of magnetization of Fe and Co ions in two tridimensional Fe/Co PBA ($Rb_{1.8}Co_4[Fe(CN)_6]_{3.3}\cdot 13H_2O$ and $K_{0.1}Co_4[Fe(CN)_6]_{2.7}\cdot 18H_2O$) has experimentally been confirmed by Champion *et al.* thanks to XMCD at Co and Fe K edges.[51] They reached the conclusion that Fe and Co ions were coupled antiferromagnetically. Unfortunately, the conclusion is based on several assumptions that have never been fully ascertained: (*i*) the XMCD signals recorded by Champion *et al*. completely miss the pre-edge features that are smeared into the noise although they are the only ones to be safely considered as being proportional to the Fe or Co magnetizations, (*ii*) the main XMCD feature observed by Champion *et al*. gives information on the $4p$ orbital magnetic moment and whether the $4p$ orbital magnetic moment is proportional or at least oriented in the same direction as the $3d$ magnetic moment is likely although never demonstrated. In addition to XMCD, Neutron scattering technique has been employed to extract information about the magnetic structure and the magnetic moments associated to the different crystallographic positions. Pajerowski *et al.*[144] reported the parallel alignment of Co and Fe magnetic moments in a thermally quenched magnetic state of a Fe/Co PBA coordination polymer $K_\alpha Co[Fe(CN)_6]_\beta\cdot nD_2O$. They observed that at 4 T and 1 T the Co sites contribute to most of the magnetization. Interestingly, this result is contrary to the K edge XMCD results by Champion *et al*. where an antiparallel alignment of the magnetic moments has been observed for an external induction of 1 T.[51]

To our knowledge, the antiferromagnetic interaction in the photo-induced state of PBA has never been observed by XMCD at $L_{2,3}$ edges. This motivated us to perform XMCD in the tridimensional PBA $Rb_2Co_4[Fe(CN)_6]_{3.3}\cdot 11H_2O$ to check for antiferromagnetic or ferromagnetic interactions between Fe and Co ions. The details of the XMCD investigations are presented as a paper in next section. The present work has been performed in collaboration with Prof. Anne Bleuzen and her team from ICMMO who synthesized the samples and recorded SQUID magnetometric data.

5.2 Paper III: XAS and XMCD at $L_{2,3}$ edges of Fe and Co in RbCoFe PBA

Status: To be submitted

Evidence of Antiferromagnetic interaction in $Rb_2Co_4[Fe(CN)_6]_{3.3}\cdot 11H_2O$ Prussian Blue Analogue by XMCD at $L_{2,3}$ edges

Sadaf Fatima Jafri*[1], Robinson Moulin[2], Marie-Anne Arrio[1], Amélie Juhin[1], Amélie Bordage[2], Anne Bleuzen[2], Edwige Otero[5], Christophe Cartier dit Moulin[3,4], and Philippe Sainctavit†[1,5]

[1]Institut de Minéralogie, de Physique des Matériaux et de Cosmochimie, UMR7590, CNRS, UPMC, IRD, MNHN, 75252 Paris Cedex 05, France
[2]Institut de Chimie Moléculaire et des Matériaux d'Orsay, Université Paris-Sud 11, UMR 8182, 91405 Orsay cedex, France.
[3]CNRS, UMR 8232, Institut Parisien de Chimie Moléculaire, F-75005, Paris, France.
[4]Sorbonne Université, UPMC Univ Paris 06, UMR 8232, IPCM, F-75005, Paris, France.
[5]Synchrotron SOLEIL, L'Orme des Merisiers Saint-Aubin, France

Abstract

We report the experimental observation of the magnetic coupling between Fe and Co in the photo-induced state of the tridimensional $Rb_2Co_4[Fe(CN)_6]_{3.3}\cdot 11H_2O$ Prussian Blue analogue by X-ray Magnetic Circular Dichroism at Fe and Co $L_{2,3}$ edges. At 2 K, we can separate between a surface contribution where Fe and Co are not coupled and a bulk one where Fe and Co are antiferromagnetically coupled.

5.2.1 Introduction

Fe/Co Prussian blue Analogues (PBAs) are well-known for their bi-stable physical properties tuned by external stimuli.[9,86] The discovery of photo-induced magnetization in tridimensional $K_{0.2}Co_{1.4}[Fe(CN)_6]\cdot 6.9H_2O$ PBA by Sato *et al.*[6] directed the research towards the rational design of PBA magnets exhibiting externally controlled reversible magnetization. Several Fe/Co PBA such as $A_xCo_y[Fe(CN)_6]_z\cdot nH_2O$ with z=(x+8)/3 if y=4 (A: K^+, Rb^+, Na^+, Cs^+) have been synthesized and investigated to understand thermal- and photo-induced magnetic transitions.[7,9,14,15,18,28,145] Bleuzen and co-workers performed a systematic study on series of Fe/Co Prussian blue analogues including RbCoFe PBAs to characterize and control the electron transfer mechanism and associated magnetic properties.[14,15,22,24,145,146] These fascinating photomagnetic properties of the Fe/Co Prussian Blue family were found to depend upon the nature and amount of alkali cations inserted in the structure.[15,22] RbCoFe PBAs with different stoichiometries have been

studied extensively to explore the photo-induced metastable state.[7,28] This compound displays a large photomagnetic effect.[33] The change in local magnetization is crucial to understand the response of the molecular paramagnetic species to external stimulus. Neverthless, one pertinent question about the nature of the magnetic coupling between Fe and Co in the photo-induced state of Rb_2CoFe PBA has remained puzzling. It was shown that in the Rb_2CoFe PBA, the diamagnetic to ferrimagnetic transition is observed after irradiation with a Curie temperature $T_c \approx 21$ K.[28] In Fe/Co PBAs, SQUID measurements[7,18,28] indicated an antiferromagnetic order below T_c. In mixed valence manganese PBA neutron diffraction study shows antiferromagnetic arrangements of the magnetic moments.[147] However, for Fe/Co cyanide coordination polymer, the parallel alignment of Co and Fe has also been reported.[144] Following these magnetic observations in PBAs, the ferrimagnetic nature of photo-induced state is attributed to the “antiferromagnetic" coupling between Fe and Co ions. XMCD is an excellent tool to solve this question, since it can directly probe the nature of the magnetic interaction thanks to its atomic selectivity. The “direct" evidence of an antiferromagnetic coupling in photo-induced state of RbCoFe PBA is reported by Champion *et al.*[51] which is in line with SQUID measurements on several PBA systems.[28] In $K_{0.1}Co_4[Fe(CN)_6]_{2.7}\cdot 18H_2O$ and $Rb_{1.8}Co_4[Fe(CN)_6]_{3.3}\cdot 13H_2O$, K edge, XMCD measurements have successfully confirmed the antiferromagnetic nature of the exchange interaction between the magnetic moments of Co^{II}_{HS} and Fe^{III}_{LS} ions which results in a ferrimagnetic photo-induced metastable state.[51] However, this antiparallel alignment of Fe and Co magnetic moments has never been observed so far at $L_{2,3}$ edges in tridimensional Fe/Co PBA and their associated nanostructures.[57,148] This has galvanized our efforts to look for the reversal of the local magnetization in tridimensional Fe/Co PBA by recording XMCD at $L_{2,3}$ edges.

We report here the XMCD results at the Fe and Co $L_{2,3}$ edges of tridimensional $Rb_2Co_4[Fe(CN)_6]_{3.3}\cdot 11H_2O$ PBA in the photo-induced state. These results have unearthed significant information on the nature of the magnetic interaction between both metallic ions. Ligand Field multiplet (LFM) calculations have been further employed to calculate the electronic structure of the Fe and Co ions and to quantify the amount of paramagnetic and diamagnetic Fe–Co pairs in the photo-induced metastable phase.

5.2.2 Experimental Section

The synthesis of $Rb_2Co_4[Fe(CN)_6]_{3.3}\cdot 11H_2O$, referred to as sample **1** in the following, has been performed following the procedure reported by Cafun *et al.*[33] Sample **1** was dropcasted in milli-Q water on a silicon wafer which was mounted on a standard copper sample holder used for low temperature measurements. XAS and XMCD signals at Fe and Co $L_{2,3}$ edges were measured on DEIMOS beamline at SOLEIL synchrotron (France).[90] There are two undulators, working as the photon source, namely an Apple-II helical undulator and an EMPHU undulator with different functions. The Apple-II helical undulator delivers a flux of circularly and linearly polarized X-rays for X-ray absorption, X-ray circular and linear dichroism measurements in the energy range 350–2500 eV. The EMPHU undulator is built with electromagnets and permanent magnets tailored to deliver

circularly polarized X-rays with a fast switching of the polarization state of the incoming X-rays. The fast switching of polarization between 1 Hz and 5 Hz makes it possible to record XMCD signals by switching the polarization at each energy point of a spectrum. The main end station at DEIMOS beamline consists of the cryogenic magnet CroMag which can provide a ± 7 T magnetic induction along the incoming X-ray beam and a ± 2 T magnetic induction perpendicular to the beam. The sample is attached to a variable temperature insert that controls the sample temperature between 1.5 K and 370 K. For the present study, all spectra are recorded in the total electron yield mode under UHV conditions. Sample **1** was first measured at Fe and Co $L_{2,3}$ edges at 200 K where it is believed to be in the diamagnetic state. It is then cooled down to 2 K with no intermediate temperature measurements since no thermally induced electron transfer is expected. At 2 K, sample **1** has been irradiated with laser (λ = 635 nm) for 5 hours. During the XAS and XMCD measurements, laser is switched off. XMCD signals at Fe and Co $L_{2,3}$ edges were then recorded after light induced excited spin state trapping (LIESST). To compensate for possible errors induced by spurious signals, XMCD signal was measured by taking the difference of two XAS spectra recorded for left and right polarized X-rays with the propagation vector parallel or antiparallel to the direction of the external magnetic induction $\boldsymbol{B}$. By definition, the XMCD signal is given by $\sigma_{\mathrm{XMCD}} = \sigma^- - \sigma^+$ where $\sigma^- = [\sigma_L(B^-) + \sigma_R(B^+)]/2$ and $\sigma^+ = [\sigma_L(B^+) + \sigma_R(B^-)]/2$.[131] σ_L (σ_R) is the cross-section with left (right) polarized X-rays, and B^+ (B^-) the magnetic induction parallel (antiparallel) to the X-ray propagation vector. With these definitions, a negative XMCD signal at the L_3 edge of 3*d* metals corresponds to a magnetic moment pointing in the same direction as the external magnetic induction. The background is subtracted using two arctangent functions that model the $2p_{3/2} \rightarrow$ continuum and $2p_{1/2} \rightarrow$ continuum transitions following the method described by Chen *et al.*[91]

XMCD signals for Fe and Co in the photo-induced state at 2 K were also recorded at various magnetic induction values to get a deeper understanding of the contributions to the total XMCD signal. To take advantage of the sensitivity of the dichroic measurements by EMPHU, the XMCD detected magnetization curves have been measured as a function of the applied magnetic induction to check for the possible antiferromagnetic coupling between Fe and Co. For this, one needs to set the monochromator at a given energy where the XMCD signal is maximum in absolute value. For Fe the monochromator is set at 705.6 eV and for Co it is set at 777.3 eV. The applied induction is then varied while the circular polarization delivered by the EMPHU is switched at 1 Hz to record the variation of the maximum of the L_3 edge XMCD signal for each absorbing ion. Such XMCD detected magnetization curves have been recorded for temperatures ranging between 2 K and 30 K.

In addition, soft X-ray induced electron transfer has been studied by measuring the XAS signals at 200 K and at 2 K before laser irradiation (see supporting information). During the measurements, we carefully checked that the sample **1** remains (i) free from radiation damage from the X-ray beam (ii) with no degradation related to vacuum environment (iii) stable in temperature (as it goes several heating and cooling cycles). The reversibility of photo-induced electron transfer process has been checked by warming the sample back to

200 K and XAS spectra are compared with those at the beginning of the experiment. In a last step, we have recorded the XAS and XMCD signals at Fe $L_{2,3}$ edges of $K_3[Fe(CN)_6]$ precursor which is referred as sample **2** and a comparison is made between sample **1** and **2** at Fe $L_{2,3}$ edges to obtain complementary information.

5.2.3 Results and Discussion

5.2.3.1 Light-induced metal-to-metal electron transfer

The electronic states of the diamagnetic Fe^{II}_{LS} or Co^{III}_{LS} ions and the paramagnetic Fe^{III}_{LS} or Co^{II}_{HS} ions can be easily detected by recording the XAS spectra at $L_{2,3}$ edges.[25,26,33,82] We then recorded Fe and Co $L_{2,3}$ edges at 200 K where the two ions are in a diamagnetic state and at 2 K after laser irradiation (Figure 5.1) where part of the diamagnetic ions transform into paramagnetic ones. At 200 K, the ground state for Fe is a mixture of Fe^{II}_{LS} and Fe^{III}_{LS} and similarly the ground state for Co is a mixture of Co^{III}_{LS} and Co^{II}_{HS}. Such mixed states for Fe and Co have already been reported elsewhere.[26,32,33,37] We have reference spectra for pure Fe^{III}_{LS}, Fe^{II}_{LS}, Co^{III}_{LS} and Co^{II}_{HS} from which we can by linear combination estimate the decomposition into paramagnetic and diamagnetic species (see S.I. Section 5.3.7). At 200 K, we find that Fe ions are ≈40 % Fe^{III}_{LS} and ≈60 % Fe^{II}_{LS} whereas Co ions are ≈34 % Co^{III}_{LS} and ≈66 % of Co^{II}_{HS} (see S.I. for linear combinations). The information obtained for Fe is fully compatible with the one obtained for Co if one considers errors close to ±5 % during the fitting process. After laser irradiation (λ = 635 nm) at 2 K, between half and two thirds of the diamagnetic ions transform into paramagnetic ones. At 2 K, the linear combination fit yields ≈70 % Fe^{III}_{LS} and ≈88 % Co^{II}_{HS}. Although the observed conversion is not complete, one can notice that peak **a** of the Fe L_3 edge is larger than the one reported by Cartier dit Moulin et al.[26] We attribute this difference to a larger conversion rate in the present measurements.

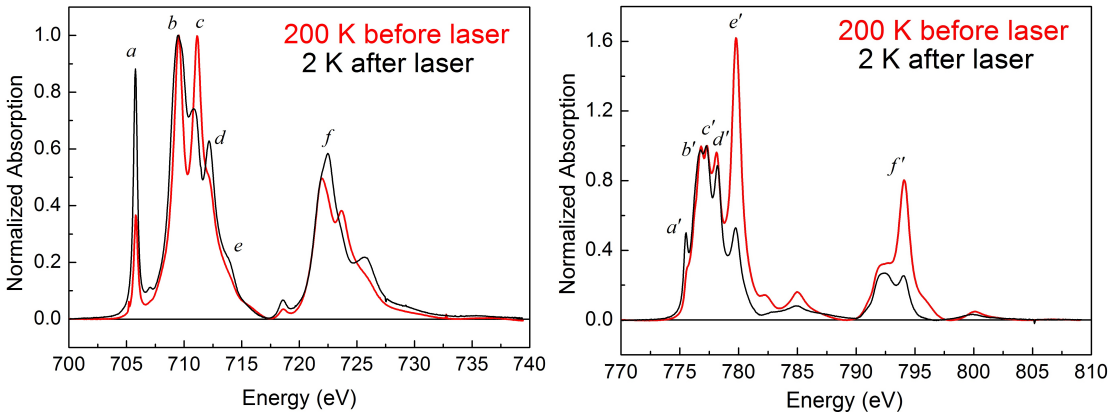

Figure 5.1 – Experimental XAS spectra at Fe (left) and Co (right) $L_{2,3}$ edges before laser irradiation at 200 K (red line) and after 5 hours laser irradiation at 2 K (black line).

Reversibility of the electron transfer process has been checked by recording Fe and Co $L_{2,3}$ edges at 200 K before and after laser irradiation (Figure 5.8 Supporting Information). The diamagnetic Fe^{II}_{LS} and Co^{III}_{LS} species are recovered although a minor percentage ($\leq$ 5 %) of additional Co^{II}_{HS} species is present which did not undergo the transition from $Co^{II}_{HS} \rightarrow Co^{III}_{LS}$ when the temperature was raised to 200 K.

5.2.3.2 Probing the Fe-Co magnetic interaction after Photo-excitation

The electronic and magnetic ground state of Fe and Co is probed by measuring the XMCD signals in photo-induced state at $L_{2,3}$ edges at 2 K and in a 6.5 T external magnetic induction (Figure 5.2) . The intensity of the maximum of the L_3 edge XMCD signal for Co (γ'/C' $\approx$ 100 %) is large and approximately 9 times larger than the XMCD signal at the Fe L_3 edge (γ/B = 11.1 %). From the comparison with theoretical XMCD signals calculated by LFM (see S.I) and the experimental XMCD signal for isolated paramagnetic Co^{II} ions, one finds that the magnetic moment of the Co ions are likely all oriented parallel to the external magnetic induction. The same comparison for Fe shows that the Fe ions are only partially magnetized (see S.I. and Jafri *et al.*[148]). In addition, the shape of the XMCD signal at the Fe $L_{2,3}$ edges is quite different from the one observed for potassium hexacyanidoferrate(III) precursor (see Fig. 5.14 in Supporting Information). In the case of Rb_2CoFe, one observes two peaks (β,γ) around 710 eV, whereas there is only one for potassium hexacyanidoferrate(III). Peak ϵ is as large as peak α whereas it is three times smaller for potassium hexacyanidoferrate(III). One simple way to interpret the reduced intensity and the additional features is to consider that there are two sites for Fe ions with one site, labelled site **a** where Fe ions are polarized parallel to the external magnetic induction and another one, labelled site **b** where the Fe ions are magnetized antiparallel to the external magnetic induction. In the two sites, Fe is clearly in the Fe^{III}_{LS} configuration but with slightly different environments and crystal fields so that β and γ features do not superimpose. At 6.5 T and 2 K, the magnetization from site **a** is larger than the one from site **b** as can be guessed from the mainly negative signal at the L_3 edge. To get more information on these possible two sites, we have recorded the XMCD detected magnetization curves for Fe and Co.

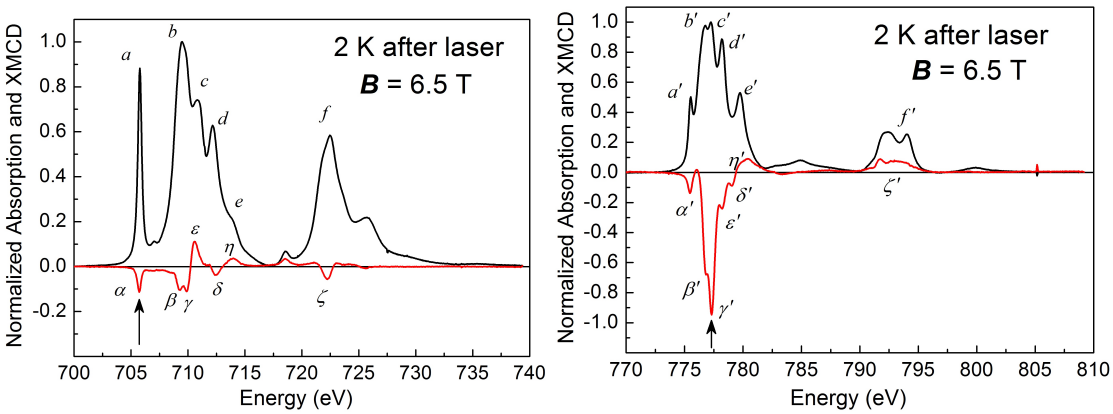

Figure 5.2 – Experimental XAS (black line) and XMCD (red line) spectra at Fe (left) and Co (right) $L_{2,3}$ edges at 2 K after a 5 hours laser irradiation.

5.2.3.3 Induction dependent XMCD investigation

In order to record the element specific magnetization curve for Co, the energy of the X-rays have been set to 777.3 eV and the external magnetic induction is switched between +6.5 T and −6.5 T. The Co magnetization curve at 2 K is reported in Fig. 5.3. One observes a sharp rise of the magnetization in the first 500 mT to which a linear increase

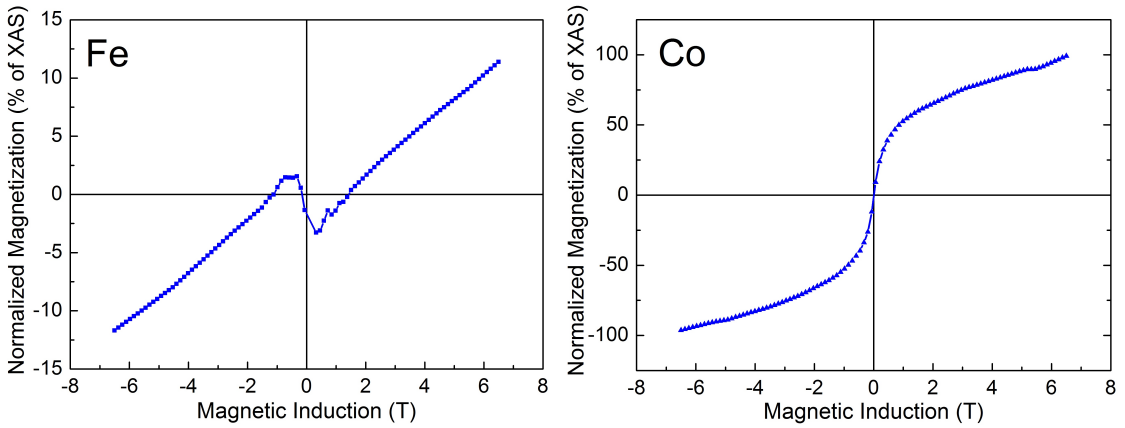

Figure 5.3 – XMCD detected magnetization curve for Fe ion (left) and Co ion at 2 K (right) recorded at E = 705.7 eV and E = 777.3 eV respectively.

of magnetization is superimposed. The variation of the Co magnetization is monotonous indicating that the Co ions are always magnetized parallel to the external magnetic induction but Co magnetization seems difficult to saturate in inductions as large as 6.5 T. On the contrary, the magnetization curve for Fe measured at 705.7 eV is much different. Between 1.5 T and 6.5 T, one observes a linear variation of the magnetization parallel to the external magnetic induction and between −1.5 T and +1.5 T, there is a clear inversion of the magnetization, i.e. the Fe magnetization is antiparallel to the external magnetic induction. Hence, the direct observation of the element specific magnetization curves show without ambiguity that between −1.5 T and +1.5 T, Fe and Co ions are coupled antiferromagnetically with the Co magnetic moment being larger than the Fe one. From Fig.5.3, we can suppose that sample **1** is built from one antiferromagnetic phase where Fe and Co are coupled antiparallel and extra phases where Fe and Co are not coupled and behave just like paramagnetic ions. Whether we have only one paramagnetic phase containing both Fe and Co or whether we have two paramagnetic phases, one for each ion, is not clear at this point. Interestingly, at $\boldsymbol{B}$ = +0.45 T where the Fe L_3 edge XMCD signal displays a negative maximum (−3 %), Co magnetization (+39 %) is ≈ 13 times larger than the one for Fe.

From the literature, the Curie temperature of **1** is 21 K so that we expect that the signature of the antiferromagnetic phase will change if the temperature is raised from 2 K up to 30 K. Obviously, the signature from the paramagnetic phase will also change with increasing temperature. We have recorded Fe and Co XMCD detected magnetization curves at T = 2 K, 4 K, 10 K, 20 K and 30 K (Figure 5.4). As we approach the Curie temperature, the signature of the antiferromagnetic phase (i.e. the non-monotonous behavior of the Fe magnetization curve) tends to disappear. At 30 K the magnetization curve is almost a straight line with no accident in the region between ±1.5 T. In Fig. 5.4, we have reported the slope of the magnetization curves at $\boldsymbol{B}$ = 0 T as a function of the temperature. For Co, the slope of the magnetization curves remain positive for all temperature values and decreases when temperature is increased. The slope of Fe magnetization is negative and it decreases in absolute values when the temperature increases from 2 K to 30 K. Around 15 K, the slope changes sign and becomes positive. This means that the contribution

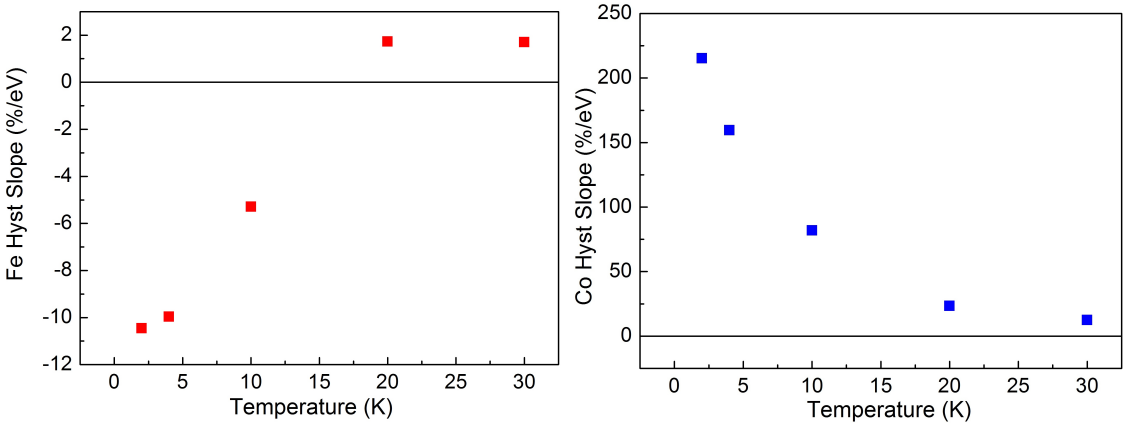

Figure 5.4 – Slope at $\boldsymbol{B} = 0$ T for the Fe and Co magnetization curves as a function of temperature.

from the antiferromagnetic phase is no more dominating over the contribution from the Fe bearing paramagnetic phase. This series of measurement prove that the antiferromagnetic phase is indeed the ordered phase measured by SQUID.

From the observation of Figure 5.3, one obviously observes different regimes where the antiferromagnetic phase is either dominating or dominated by the paramagnetic phase. To get more information, we have recorded the XMCD signal at the Fe $L_{2,3}$ edges for the three external magnetic inductions $\boldsymbol{B}_1 = 6.5$ T where the Fe magnetization is parallel to the external magnetic induction, $\boldsymbol{B}_2 = 1.5$ T where the magnetization is almost zero, and $\boldsymbol{B}_3 = 0.45$ T where the magnetization is antiparallel to the external magnetic induction. We did the same at Co $L_{2,3}$ edges but since the Co magnetic moment is always parallel to the external magnetic induction, there is no easy way to separate the contributions from the antiferromagnetic phase or from the Co bearing paramagnetic phase. The various XMCD signals at Fe and Co $L_{2,3}$ edges are reported in Figure 5.5. All the Fe XMCD signals have been normalized to the maximum of the XAS spectrum. For Co XMCD signals the extra multiplicative coefficient is 2.5 for $\boldsymbol{B}_3$. Interestingly one sees that both Co XMCD signals for $\boldsymbol{B}_1$ and $\boldsymbol{B}_3$ have almost exactly the same shape. This indicates that the Co ions are in very similar environments whether they are present in the antiferromagnetic phase or in the Co bearing paramagnetic phase and that the Co magnetization is always parallel to the external magnetic induction for both phases. On the contrary one observes that the shape of the Fe XMCD signals varies quite a lot with the intensity of the induction. This further confirms that Fe ions are present in at least two different phases, the antiferromagnetic one and the paramagnetic one, and for which the crystal field parameters are substantially different. The two peaks β and γ are signatures of the two phases.

One can notice that the intensity of the γ feature decreases much with the induction since the ratio β/γ are approximately 1:2:4 for $\boldsymbol{B}_1$:$\boldsymbol{B}_2$:$\boldsymbol{B}_3$ respectively. This further confirms that peak γ is a signature of the antiferromagnetic phase and peak β is a signature of the Fe bearing paramagnetic phase. More information can be gained on the antiferromagnetic phase from linear combinations of Fe XMCD signals at 6.5 T and 0.45 T. The β peak comes from the Fe bearing paramagnetic phase, so that if both XMCD signals are rescaled for the β features to superimpose, the difference between the two rescaled XMCD signals should give an approximate XMCD signal for the antiferromagnetic phase (Fig.5.6). Figure 5.7

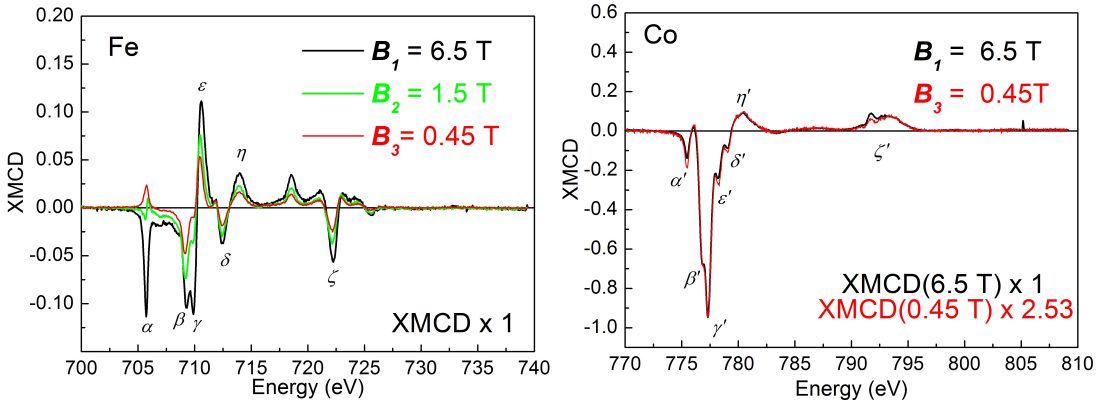

Figure 5.5 – XMCD signals at Fe $L_{2,3}$ edges recorded at $\boldsymbol{B}$ = 6.5 T (black line), 1.5 T (green line), 0.45 T (red line) at T = 2 K (left panel). For comparison, Co XMCD signals at $\boldsymbol{B}$ = 0.45 T and $\boldsymbol{B}$ = 6.5 T. The signal at 0.45 T is normalized so that γ' peak superimposes with γ' peak at 6.5 T (right panel).

shows that the difference spectrum is very much alike the XMCD signal for pure potassium hexacyanidoferrate(III), i.e. sample **2**.

From what precedes, we know that the Co sites in the antiferromagnetic phase and in the paramagnetic one are both very similar. For Fe^{III} ions, the Fe^{III} site in the antiferromagnetic phase is much alike the Fe^{III} site in potassium hexacyanidoferrate(III) and the Fe^{III} site in the paramagnetic phase would be similar to the one for a strongly distorted site such as **FeTp**. The easiest way to accommodate for the two phases is to consider that the bulk of the tridimensional PBA is indeed the antiferromagnetic phase whereas the paramagnetic phases comes from the Fe^{III} and Co^{II} ions at the surface of the PBA grains for which the crystallographic and the magnetic disorder would destroy the antiferromagnetic interactions.

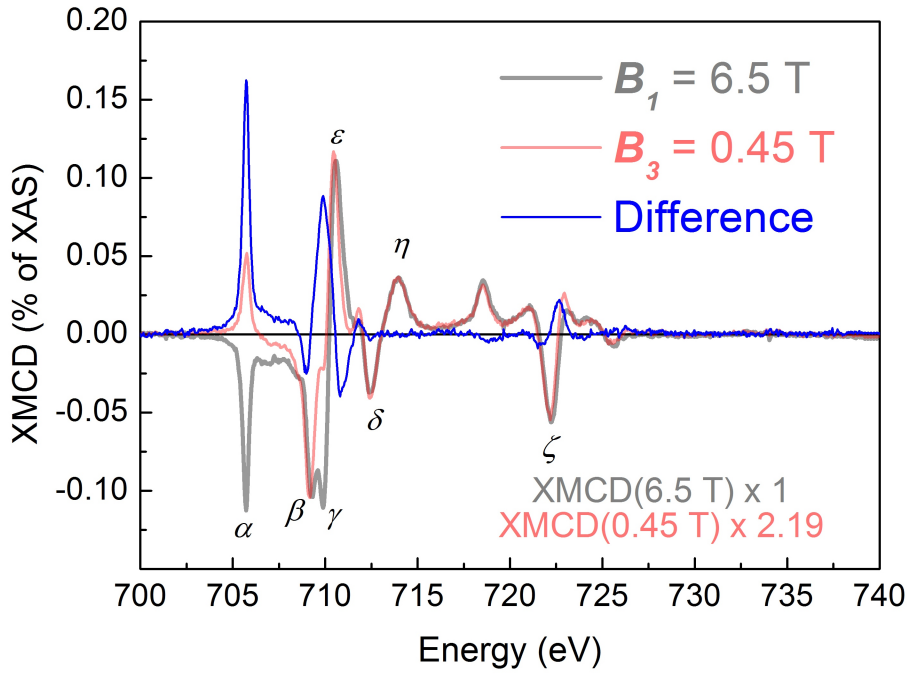

Figure 5.6 – Difference of two XMCD signals at Fe $L_{2,3}$ edges (blue line) recorded at $\boldsymbol{B}$ = 6.5 T and 0.45 T. The XMCD signal at $\boldsymbol{B}$ = 0.45 T is normalized so that peak β superimpose with the one from the XMCD signal at $\boldsymbol{B}$ = 6.5 T.

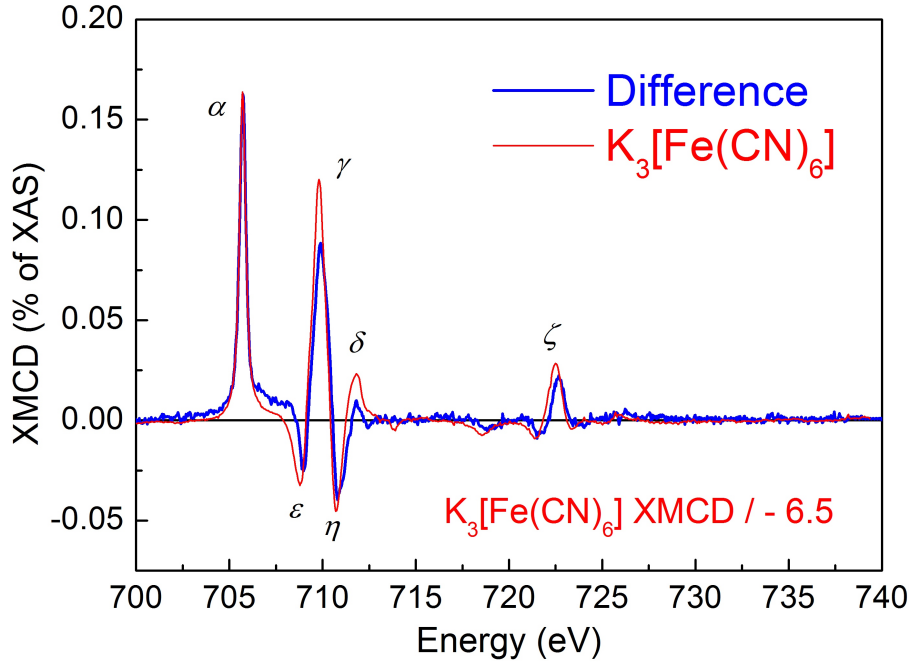

Figure 5.7 – Signal difference from Fig.5.6 (blue line) and XMCD signal at Fe $L_{2,3}$ edges for potassium hexacyanidoferrate(III) recorded at $\boldsymbol{B}$ = 6.5 T divided by a factor of -6.5 (red line).

All spectra are recorded in total electron yield mode (TEY) where all electrons emitted from the samples are registered independent of their energy. These photoelectrons are created in proximity to the surface thus limiting the probing depth to the first five nanometers. The most simple model for the intensity of photoelectrons measured in TEY is governed by an attenuation length λ the value of which is quite uncertain. If λ is arbitrarily set to 1 nm then the first nanometer would contribute to 65 % of the whole XAS signal. If λ = 2 nm then the first nanometer would contribute to 43 % of of the XAS signal.

The previous depth analysis is fully consistent with our interpretation of contribution from the different sites. One contribution is coming from the bulk and the other is coming from the very surface.

5.2.4 Conclusion

The main conclusion from the present piece of work is that it has been possible to prove at the atomic level the existence of an antiferromagnetic interaction between Fe ions and Co ions in $Rb_2Co_4[Fe(CN)_6]_{3.3}\cdot 11H_2O$. From SQUID measurements and by comparison with non photomagnetic systems, the existence of such an interaction was considered as almost certain but this is the first time to our knowledge that such an antiferromagnetic coupling is confirmed by both experimental and theoretical XMCD signatures from both Fe and Co edges. The conclusion is very robust as can be seen from the large difference in XMCD intensity between Fe and Co ions, the negative slope of the magnetization at Fe $L_{2,3}$ edges and the exact shape of the XMCD signal at the Fe $L_{2,3}$ edges that perfectly mimics the one for potassium hexacyanidoferrate(III) but for a reversed magnetization with respect to the external magnetic induction. In addition, it is found that the Fe–Co pairs at the surface of the PBA grains do not experience the same antiferromagnetic interaction

because of geometric disorder and a lack of magnetic neighbors. This raises the question of the nature of the magnetic interaction in photomagnetic molecular Fe/Co PBA such as the cube,[43] the square,[11,45,46,118,120,149] or the dinuclear[49,119] complexes that have been recently synthesized.

Acknowledgement

This work was supported by the Centre National de la Recherche Scientifique (CNRS, France), the Ministère de l'Enseignement Supérieur et de la Recherche (MESR, France), and the GdR MCM2. We are thankful to SOLEIL staff for running the machines.

5.3 Supporting Information of Paper III

5.3.1 Reversibility of electron transfer process

The reversibility of light-induced electron transfer is confirmed by recording XAS spectra at $T = 200$ K before and after laser irradiation (Figure 5.8).

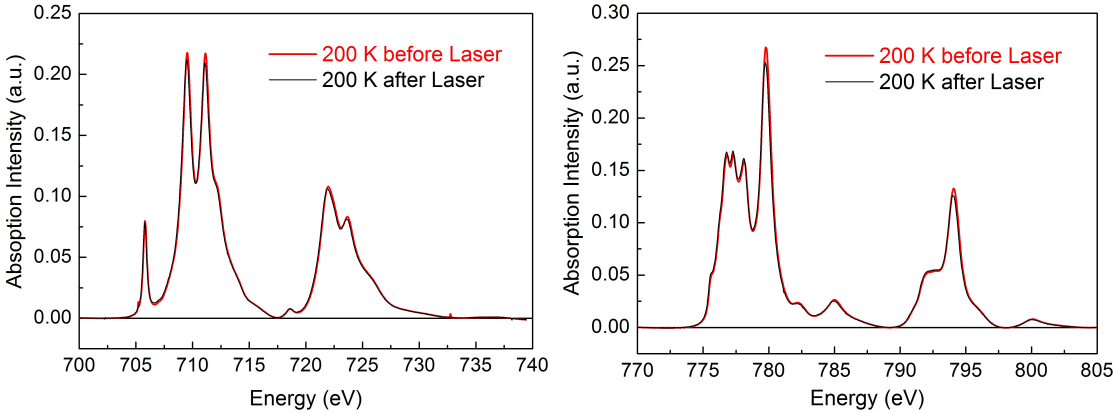

Figure 5.8 – Experimental XAS spectra at Fe (left) and Co (right) $L_{2,3}$ edges at 200 K before irradiation (red line) and after irradiation at 2 K and warming up back at 200 K (black line).

5.3.2 X-ray induced metal-to-metal electron transfer

To follow the X-ray induced electron transfer, XAS spectra at Fe and Co $L_{2,3}$ edges are recorded at 200 K and 2 K before irradiation. At 200 K, the ground state is a mixture of Fe^{II}_{LS}, Co^{III}_{LS} and Fe^{III}_{LS}, Co^{II}_{HS} species[26]. From figure 5.9, one observes that characteristic features for Fe^{II}_{LS} (**b** and **c**) and for Co^{III}_{LS} peak (**e'**) are the dominant features.[9,25,26,33,37] Upon cooling down to 2 K, no thermal-induced electron transfer is expected in this Fe/Co PBA.[22,33] Under X-ray beam at 2 K, a partial electron transfer between Fe and Co transforms Fe^{II}_{LS} into Fe^{III}_{LS} and Co^{III}_{LS} into Co^{II}_{HS}. This conversion is manifested by an intensity of increase in Fe^{III}_{LS} signature (peak **a**) and the corresponding decrease in Co^{III}_{LS} signature (peak **e'**).

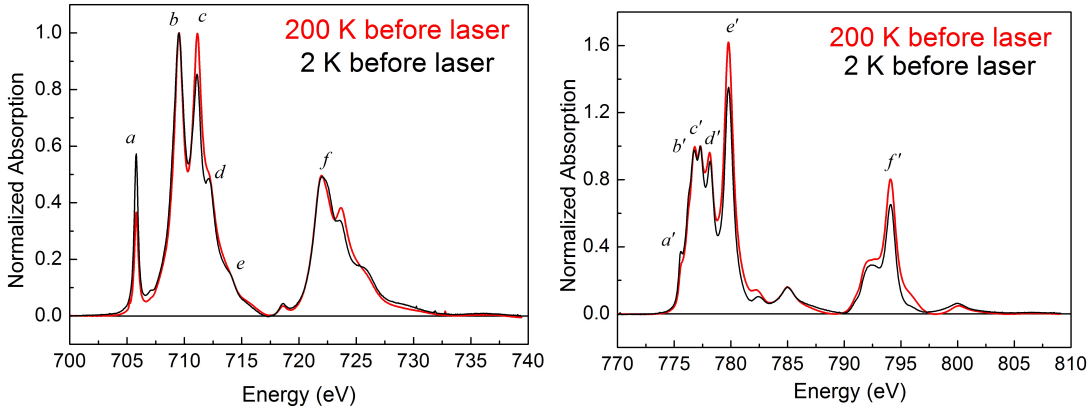

Figure 5.9 – Experimental XAS spectra at Fe (left) and Co (right) $L_{2,3}$ edges at 200 K (red line) and at 2 K before laser irradiation (black line).

5.3.3 X-ray induced vs light-induced electron transfer

Figure 5.10 shows the Fe and Co $L_{2,3}$ XAS spectra in the X-ray induced and the light-induced paramagnetic state. The X-ray induced metal-to-metal electron transfer results from the measurement at 2 K of the Fe and Co $L_{2,3}$ edges before laser irradiation. The light-induced metal-to-metal electron transfer results from laser irradiation during 5 hours. For comparison, the XAS spectra at 200 K, at 2 K in the X-ray induced magnetic phase, and at 2 K in the laser induced magnetic phase are plotted together. After X-ray irradiation and after laser irradiation, the intensity of the characteristic features for Fe^{III}_{LS} (peak **a**) increases as a signature of the metal-to-metal electron transfer. The ratios of peaks **a**/**b** are 0.37, 0.58, 0.88 at 200 K and at 2 K before and after laser respectively. For the Co $L_{2,3}$ edges, the ratio **e**'/**c**' are 1.62, 1.35, 0.53 at 200 K, at 2 K before and after laser irradiation respectively, indicating a decrease of the number of Co^{III}_{LS} ions.

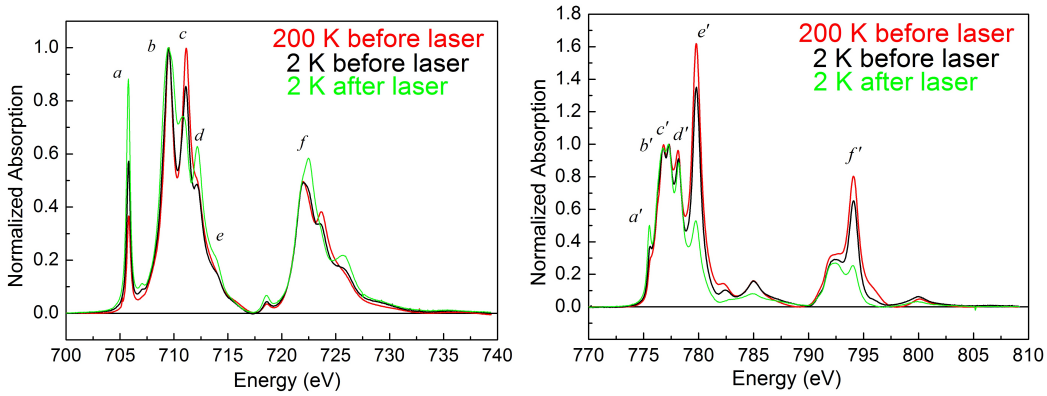

Figure 5.10 – Experimental XAS and XMCD spectra at Fe (left) and Co (right) $L_{2,3}$ edges at 200 K before irradiation (red line), 2 K before laser irradiation (black line) and after 5 hours laser irradiation (green line).

We have compared the electron transfer process induced by X-ray and light irradiation and extracted the fraction of Fe^{II}_{LS}, Fe^{III}_{LS}, Co^{III}_{LS} and Co^{II}_{HS} at 200 K, at 2 K under X-ray irradiation and at 2 K after 5 hours laser. At 200 K, 40 % of the Fe ions are Fe^{III}_{LS} paramagnetic ions. At the end of X-ray irradiation, one measures 52 % of Fe^{III}_{LS} so that only ≈20 % of the existing Fe^{II}_{LS} have been converted. For laser irradiation, we have shined sample **1** for different time durations from 15 minutes up to 5 hours and we have found that the converted sample contained ≈70 % of Fe^{III}_{LS} ions (Fig 5.11). For Co ions the same type of analysis can be made. The percentage of Co^{II}_{HS} has been reported in Fig.5.12. We attribute the difference between the concentrations of and Fe^{II}_{LS} and Co^{II}_{HS} to the existence of the surface paramagnetic phase for which the stoichiometric ratio might be different from the bulk value for sample **1**.

Figure 5.13 shows the effect of laser irradiation when sample **1** is irradiated for different time intervals.

5.3.4 Fe XMCD signals and magnetization curves in sample 1 vs sample 2 (Potassium hexacyanidoferrate(III))

Figure 5.14 shows the experimental XAS and XMCD spectra at Fe $L_{2,3}$ edges of sample **1** and for potassium hexacyanidoferrate(III) (sample **2**). One can see that the shape and

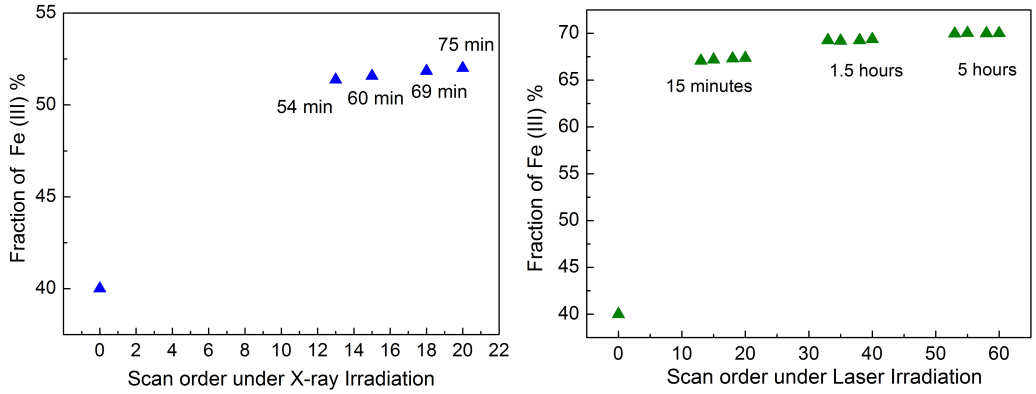

Figure 5.11 – The Fe^{II}_{LS} fraction as a function of number of scans under X-ray (left) and laser irradiation (right) respectively. The sample was irradiated with laser for time interval = 15 min, 1.5 hours and 5 hours.

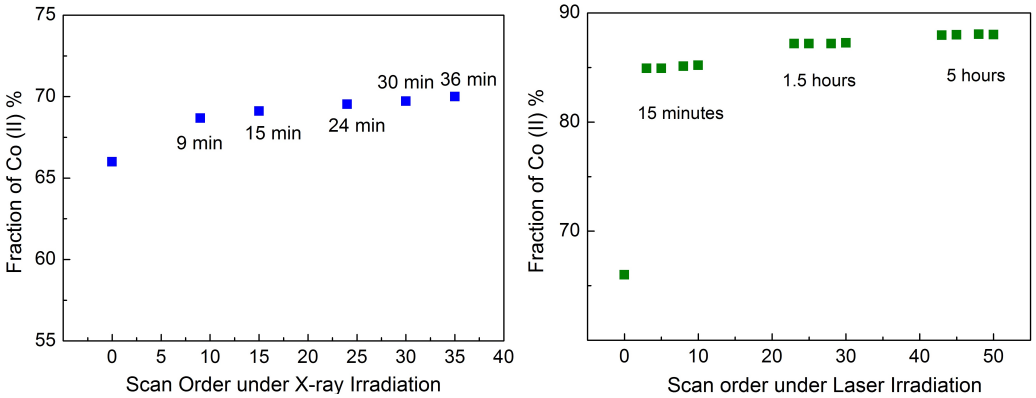

Figure 5.12 – The Co^{III}_{LS} fraction as a function of number of scans under X-ray (left) and laser irradiation (right) respectively. The sample was irradiated with laser for time = 15 min, 1.5 hours and 5 hours.

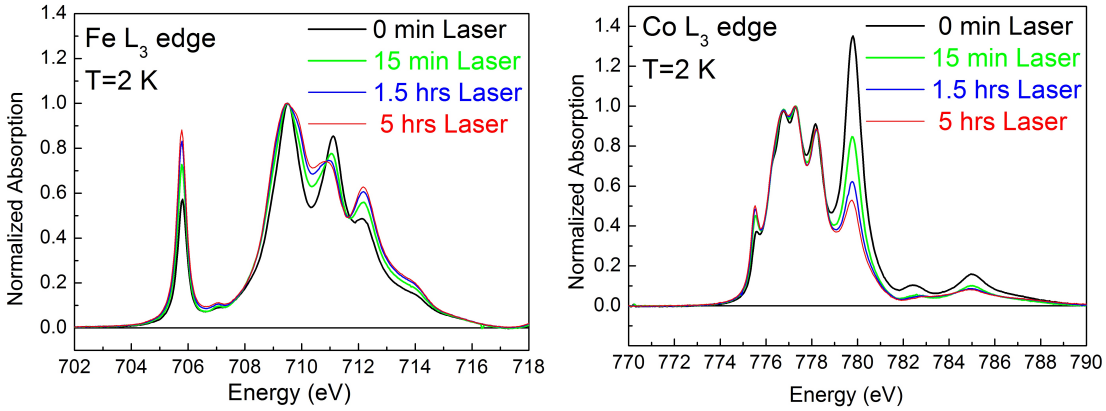

Figure 5.13 – Experimental XAS spectra at Fe (left) and Co (right) L_3 edge (zoom) at 2 K after laser irradiation for time t = 15 min (green line), t = 1.5 hours (blue line) t = 5 hours (red line).

intensity of the XAS spectra and XMCD signals are quite different. At the L_3 edge, the XMCD ratio (α/**a**) is ≈13 % for sample **1** and 80 % for sample **2**. The XMCD signal at 710 eV is split into two features β and γ in sample **1** which is attributed to the presence of two Fe^{III}_{LS} sites. The ratio (γ/**a**) is 12.6 % in sample **1** and 59 % in sample **2**. The reduced intensity of the XMCD features is an indication that some of the Fe^{III}_{LS} ions are pointing in a direction antiparallel to the external magnetic induction as it would be the case for Fe

ions antiferromagnetically coupled to Co^{II}_{HS} ions.

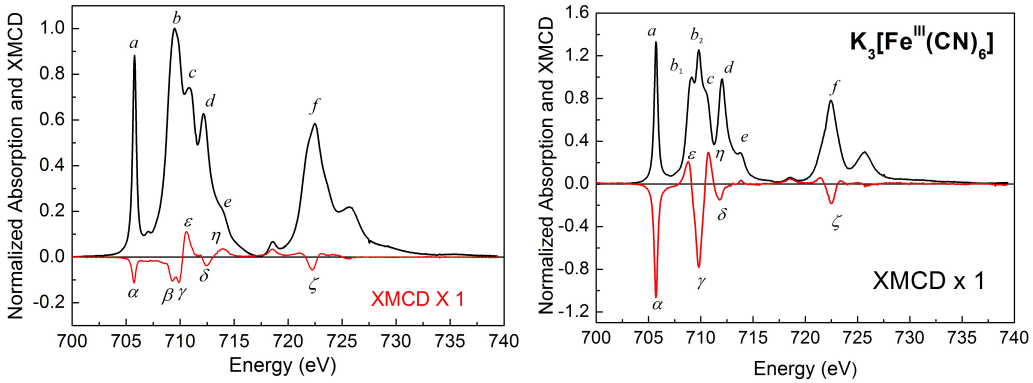

Figure 5.14 – Experimental XAS spectra (black line) and XMCD signals (red line) at Fe $L_{2,3}$ edges of sample **1** (left) and its potassium hexacyanidoferrate(III) precursor $K_3[Fe^{III}(CN)_6]$ (right) at 2 K, B = 6.5 T.

Figure 5.15 reports the XMCD detected magnetization curves of Fe as a function of the external magnetic induction at $T = 2$ K in sample **1** and **2**. The magnetization curve of the potassium hexacyanidoferrate(III) follows the direction of external magnetic induction as it is expected for isolated paramagnetic ions. On the contrary, the XMCD signal in sample **1** clearly indicates that the Fe magnetization is antiparallel to the external magnetic induction between -1.5 T and 1.5 T.

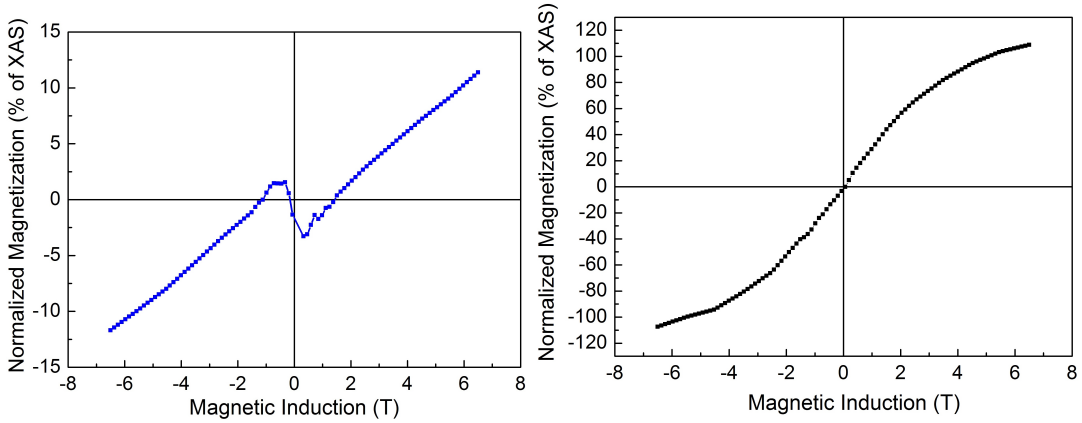

Figure 5.15 – Induction dependence of the maximum of the XMCD signal at the Fe L_3 edge (Energy = 705.7 eV) induction at 2 K in RbCoFe sample **1** (left panel) and in potassium hexacyanidoferrate(III) sample **2** (right panel).

5.3.5 XMCD detected magnetization curves for Fe and Co in sample 1

The XMCD detected magnetization curves of Fe in sample **1** as function of external induction recorded for $T = 2$ K, 10 K, 20 K, 30 K are given in Figure 5.16. As the temperature reaches the Curie temperature ($T_c = 21$ K), the system tends to loose the ferrimagnetic order and at 30 K the magnetization of Fe and Co ions are both aligned parallel to the external magnetic induction as expected for non coupled paramagnetic ions.

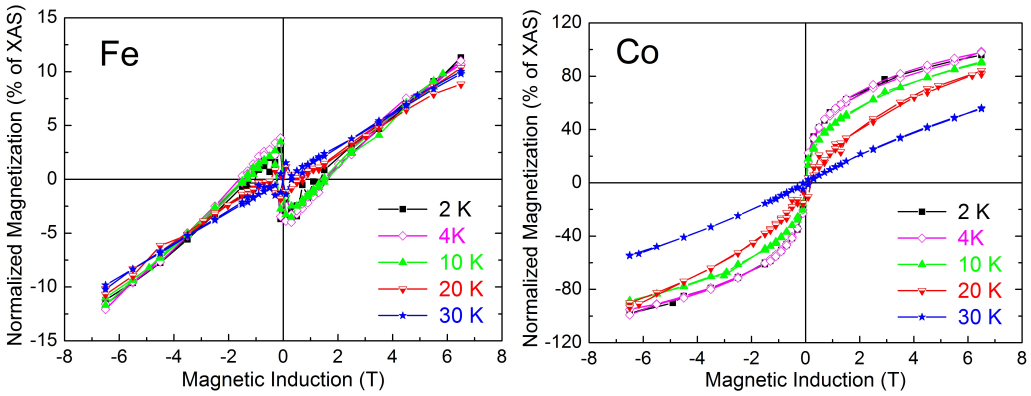

Figure 5.16 – XMCD detected magnetization curves at Fe L_3 edge, E = 705.7 eV (left panel) and Co L_3 edge, E = 777.3 eV (right panel) at 2 K (black line), 4 K (pink line), 10 K (green line), 20 K (red line) and 30 K (blue line).

5.3.6 LFM calculations of Co $L_{2,3}$ edges

The Co^{II} XAS spectra and XMCD signals are simulated by Ligand Field Multiplet Calculations in D_{4h} symmetry with Dt = 0.02 eV, Ds = 0.043 eV, 10Dq = 1.23 eV and $\kappa = 0.7$.

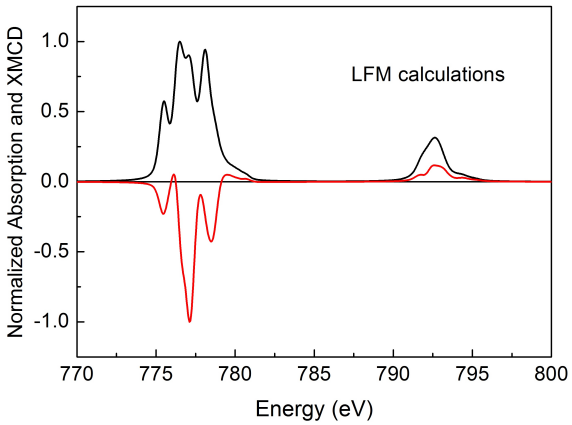

Figure 5.17 – Theoretical XAS and XMCD spectra at $L_{2,3}$ edges for Co obtained for Dt = 0.02 eV, Ds = 0.043 eV and 10Dq = 1.23 eV in D_{4h} symmetry at $T = 2$ K with $\boldsymbol{B} = 6.5$ T.

5.3.7 Linear combinations

The reference spectra of pure Co^{II}_{HS}, Co^{III}_{LS} and Fe^{II}_{LS}, Fe^{III}_{LS} used for linear combination are presented in Figure 5.18 and Figure 5.19 respectively. The Co^{II}_{HS}, Co^{III}_{LS} references are simulated using LFM calculations whereas Fe^{II}_{LS}, Fe^{III}_{LS} XAS spectra are the experimental cross-sections for $K_4[Fe(CN)_6]$ and $K_3[Fe(CN)_6]$ at $T = 2$ K and $\boldsymbol{B} = 6.5$ T. The Co^{II} XAS spectra and XMCD signals are simulated by Ligand Field Multiplet Calculations in D_{4h} symmetry with Dt = 0.02 eV, Ds = 0.043 eV, 10Dq = 1.23 eV and $\kappa = 0.7$. For the Co^{III}, the LFM parameters for O_h symmetry are Dt = 0 eV, Ds =0 eV, 10Dq = 2.5 eV and $\kappa = 0.7$.

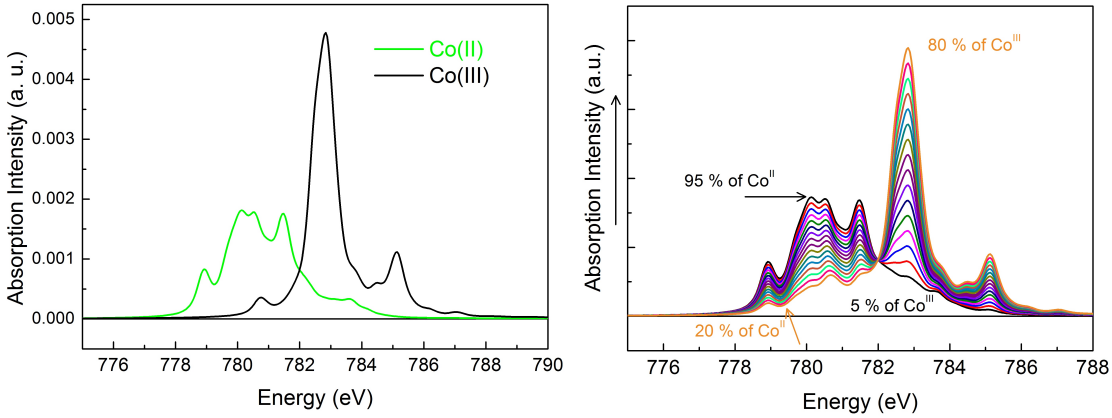

Figure 5.18 – Theoretical XAS spectra at $L_{2,3}$ edges for Co (left) and the linear combination (right).

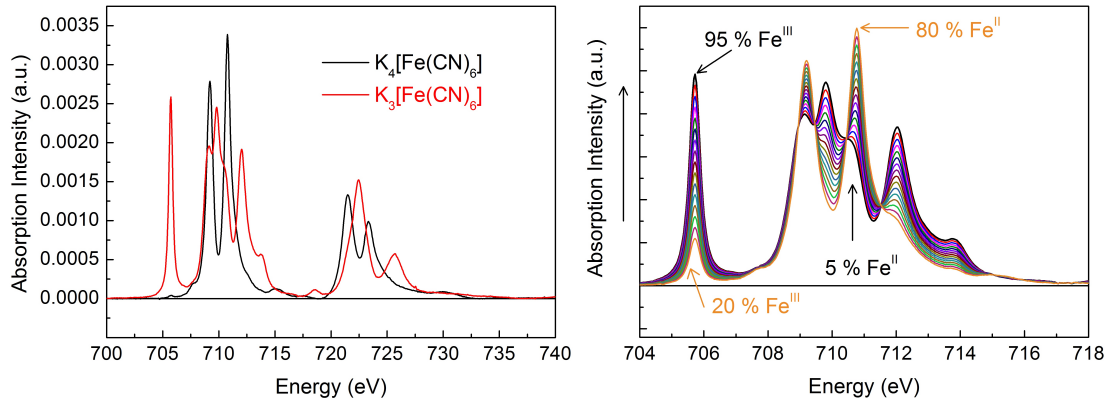

Figure 5.19 – Experimental XAS spectra at Fe $L_{2,3}$ edges of $K_3[Fe(CN)_6]$ and $K_2[Fe(CN)_6]$ used for the linear combination (left) and the linear combinations (right).

5.4 Summary of Chapter 5

In this chapter, we have proved the existence of an antiferromagnetic coupling between Fe and Co ions in $Rb_2Co_4[Fe(CN)_6]_{3.3}\cdot 11H_2O$ (sample **1**) when the sample is in its light-induced metastable state below 15 K. This finding has mainly been obtained from the XMCD signal recorded at the Fe $L_{2,3}$ edges and also by comparison with the Co XMCD signal. The antiferromagnetic coupling is strongly supported by the following:

(*i*) the intensity of the Fe XMCD signals is 9 times smaller than the Co one,

(*ii*) the XMCD detected magnetization curve for Fe proves that the magnetization of a majority of Fe ions is aligned antiparallel to the external magnetic induction when the magnetic induction is such that $-1.5\ T \leq \boldsymbol{B} \leq +1.5\ T$,

(*iii*) the shape of the XMCD signal for the antiferromagnetically coupled Fe^{III} ions is identical to the one for potassium hexacyanidoferrate(III) except for the direction of magnetization.

Our findings confirm the previously reported data by Champion *et al.* at the Fe and Co K edges for similar tridimensional systems for which the analysis was far from obvious.[51] Whether this result found for a tridimensional PBA still holds for the Fe/Co molecular complexes such as the dimers, the squares or the cubes cannot be inferred from the present results. At least, it can be said that there is no antiferromagnetic coupling at 2 K in the

Fe/Co dinuclear complex $[(Tp)Fe^{III}(CN)_3Co^{II}PY5Me_2](PF_6)\cdot 2DMF$ as it has been found from our XMCD data at the Fe and Co K edges in paragraph 4.4.

Conclusion and Perspective

This thesis was dedicated to the investigation of photo-switchable Fe/Co Prussian Blue Analogues and their corresponding precursors. The presence of magneto-optical bistabilities make these molecular complexes potential candidate for energy efficient, photo-switchable molecule-based information storage. For the technological interests, the manipulation of physical properties requires the investigation of these materials by state-of-the-art techniques. The present study on Fe/Co PBA has brought new insights towards the understanding of photomagnetic properties of these systems through experimental XMCD measurements enlightened when possible by a theoretical description within the LFM theory.

After the review of literature I had many questions and problems at hand that were not fully answered.

1) To what extent reducing the dimensionality of magnetic materials can affect their physical properties?

2) Can the building block precursors preserve their individual magnetic properties in an associated molecular system? If yes then to what extent the properties of PBAs are altered?

3) What is the role of magnetic anisotropy in low dimensional magnetic molecular systems? How the external perturbations, for instance laser irradiation vs X-ray irradiation, can change the magnetic interaction between the metallic ions?

4) What is the magnetic interaction between Fe and Co ions in the photo-induced state of Fe/Co PBA?

To answer these questions, a detailed experimental and theoretical study was performed on molecular complexes which include Fe-bearing precursors of photomagnetic Prussian Blue Analogues, two photomagnetic dinuclear complexes, and a tridimensional RbCoFe PBA.

LFM calculations in FeTp precursor revealed a large value of orbit magnetic moment. This value was in contradiction with that measured from SQUID magnetometry. To account for this difference, angular dependence of orbit and spin magnetic was checked and a strong anisotropy in the low spin Fe^{III} FeTp precursor was confirmed. In addition, a methodological approach was developed to investigate the origin of spin sum rules failure which can be extended to other systems where the application of spin sum rules is under question.

In a next step, two Fe/Co photomagnetic dinuclear complexes were studied. The two dinuclear complexes have **FeTp** precursor as one of the building blocks. The first dinuclear complex referred as **1** exhibited thermal- and light-induced electron transfer properties in solid state, confirmed by XMCD at K and $L_{2,3}$ edges. At 2 K no signature of antiferromagnetic coupling is observed between Fe and Co ions in photo-induced state. From the XMCD detected magnetization curves, the Fe and Co magnetic moments were found to be aligned parallel to the external magnetic induction and no opening of the curve was observed. The second dinuclear complex namely **2**·2DMF preserved the electron transfer properties in presence of solvent molecules. In this complex, XMCD measured at the Fe and Co K edges confirmed the thermal- and light-induced electron transfer. Both complexes were found to display bistability below 50 K.

At $L_{2,3}$ edges, measurements of XAS and XMCD spectra for the photomagnetic electron transfer systems need special conditions. To obtain the good data, damaging of sample under X-ray irradiation can be avoided only working with low flux of incoming X-rays. Based on these precautions, a systematic experimental investigation in tridimensional RbCoFe PBA confirmed the antiferromagnetic interaction between Fe and Co at $L_{2,3}$ edges that had been previously alleged. The XMCD technique is proved to be an excellent technique that can separate the antiferromagnetic coupled Fe-Co from other surface contributions.

Concerning the questions that were not fully answered and that would require further investigations, I would suggest the possible strategy.

1) What is the nature of coupling in dinuclear PBA molecules?

For this, the antiferromagnetic coupling should be checked in sub-kelvin temperature range. Further developments in the experimental set-up at $L_{2,3}$ edges requires a cell specifically designed for the study of solutions under UHV conditions. The liquid cell is in development by Niéli DAFFE a Ph.D. student in our group. The **2**·2DMF dinuclear complex which exhibits electron transfer in presence of solvent molecules could be studied by XMCD at $L_{2,3}$ edges under UHV conditions. In addition, comparison of the XMCD signals of the two dinuclear complexes at 400 mK using French TBT set-up at SLS might help understanding the nature of magnetic interaction in smallest units of Fe/Co PBA.

2) What can be said about the nature of coupling from the measurements at K edges?

To answer this question, further investigations are required to explain the differences observed in XMCD signals in Fe-precursor and in the dinuclear PBA complexes at K edge. Moreover, these K edge data can be compared with the K edge data of the tridimensional PBA. In addition, photon-in photon-out Resonant Inelastic X-ray Scattering combined with magnetic circular dichroism (RIXS-MCD) can be performed. At K pre-edge of the 3d elements, the high resolution of RIXS is an advantage combined with the bulk sensitivity and the low self-absorption effects. It was shown that hard X-ray RIXS-MCD can be a valuable alternative to soft X-ray XMCD, when using demanding sample environments, such as liquids and gas cells, or when investigating materials whose surface may be non representative of bulk properties.

The Density Functional Theory (DFT) at K edges can be applied to extract the

information about the electronic structure. A project is dedicated to the application of DFT theory at transition metal K edges in our group at IMPMC. Although, DFT lacks the multiplet effects at present, the development of the theory is in progress by a Ph.D. student Nadejda BOULDI (IMPMC).

3) How can we estimate the number of antiferromagnetically coupled Fe sites in tridimensional PBA?

A detailed LFM investigation is required to estimate the number of Fe and Co sites where the magnetic moments are aligned antiparallel. This could be achieved by simulating the XMCD signal for various magnetic induction values. The orbit and spin magnetic moments can be extracted once a good agreement between the experimental XAS/XMCD and the LFM calculated spectra is achieved. Moreover, it is worth trying to record the K edge XMCD spectra in tridimensional PBA with special attention to the K pre-edge region. This could be compared with the K edge XMCD signals of dinuclear complex **1** and **2**·2DMF.

Ligand Field Multiplet calculations need to be improved to simulate XAS and XMCD spectra of Co ions in dinuclear complex. The preliminary LFM calculations suggest that the electronic structures of Co ions in photo-induced paramagnetic state and high temperature paramagnetic state are similar. This would need a project dedicated to the LFM investigations reproducing the spectral changes with good symmetry in high temperature paramagnetic state, low temperature diamagnetic state and low temperature photo-induced state.

5) What is the next step in exploring the magnetic properties of the photomagnetic molecular systems?

The magnetic bistability occur at low temperature, so can this phenomenon of magnetic bistability be observed at higher temperatures in the sub-picosecond time domain which is the fundamental time scale of molecular motion? Thus, probing the length- and time-scales on which the photo-induced processes take place can gain a significant insight into the processes during and after the photo-induced conversion. In this regard, femtosecond optical spectroscopy and time resolved X-ray diffraction is a powerful technique for studying photoswitching dynamics. Recently, femtosecond XAS at X-FEL and optical spectroscopy are combined and the structural stabilization of photo-induced state is observed in ultrafast time scale. Thus, there is a great scope to study the ultrafast structural dynamics of the photo-induced state of PBA systems to answer the questions, for instance, why is there a slower response to the laser irradiation? Furthermore, the cooperative effects should be investigated especially for Prussian Blue Analogues where metal-to-metal electron transfer accompanies the structural relaxation around metal ions. The cooperative response in PBA can be observed on ultra-fast time scale which will enable to check whether the similar cooperative effects are present in dinuclear complexes?

The three years of the Ph.D. training provided me the opportunities to work in collaboration with different groups of chemists and physicists. Using the cutting-edge experimental facilities at SOLEIL, ESRF and SLS synchrotron sources helped in developing my experimental approach towards problem solving, critical thinking skills and team work. During my

doctoral thesis, I presented my research work in several conferences including ICMM-2014 (Saint Petersburg, Russia), JMC, CMD-2014 (Paris, France), SUM-SOLEIL (2014, 2015 and 2016), XAFS16 (Karlsruhe, Germany), GDR-MCM2 (Dourdan), Hi-SPEAR meeting (SOLEIL, 2016) and synchrotron summer school (Compinas, Brazil). Meeting people from diverse cultural and scientific backgrounds and exchange of scientific ideas have been a wonderful experience that instilled in me the vision to keep up the scientific standards in my present and future research projects.

References

[1] Silvio Decurtins, Philippe Gütlich, CP Köhler, Hartmut Spiering, and Andreas Hauser. Light-Induced Excited Spin State Trapping in a Transition-Metal Complex: The hexa-1-propyltetrazole-iron (II) tetrafluoroborate spin-crossover system. *Chem. phys. lett.*, 105(1):1–4, 1984. (see p. 19)

[2] Philipp Gütlich, Ana B Gaspar, and Yann Garcia. Spin State Switching in Iron Coordination Compounds. *Beilstein J. Org. Chem.*, 9(1):342–391, 2013. (see p. 19)

[3] Andrea Caneschi, Dante Gatteschi, Roberta Sessoli, Anne Laure Barra, Louis Claude Brunel, and Maurice Guillot. Alternating Current Susceptibility,High Field Magnetization, and Millimeter band EPR Evidence for a Ground S = 10 state in $[Mn_{12}O_{12}(CH_3COO)_{16}(H_2O)_4]\cdot 2CH_3COOH\cdot 4H_2O$. *J. Am. Chem. Soc.*, 113(15):5873–5874, 1991. (see p. 19)

[4] Roberta Sessoli, Hui Lien Tsai, Ann R Schake, Sheyi Wang, John B Vincent, Kirsten Folting, Dante Gatteschi, George Christou, and David N Hendrickson. High-Spin Molecules:$[Mn_{12}O_{12}(O_2CR)_{16}(H_2O)_4]$. *J. Am. Chem. Soc.*, 115(5):1804–1816, 1993. (Not cited)

[5] Diana Codreanu Siretanu. Functionalization of Molecular Magnetic Materials: Towards the Soluble Systems and Liquid Crystal, 2011. (see p. 19)

[6] Osamu Sato, Tomokazu Iyoda, Akira Fujishima, and Kazuhito Hashimoto. Photoinduced Magnetization of a Cobalt-Iron Cyanide. *Science*, 272(5262):704–705, 1996. (see pp. 19, 20, 38, 39, 71, 97 and 99)

[7] Osamu Sato, Yasuaki Einaga, Akira Fujishima, and Kazuhito Hashimoto. Photoinduced Long-Range Magnetic Ordering of a Cobalt Iron Cyanide. *Inorg. Chem.*, 38(20):4405–4412, October 1999. (see pp. 20, 21, 71, 97, 99 and 100)

[8] Evangelia S. Koumousi. Synthesis and Characterization of Dinuclear Fe/Co Complexes Exhibiting Metal-to-Metal Electron Transfer Properties, 2015. (see pp. 19, 67, 68, 87, 94 and 95)

[9] David Aguilà, Yoann Prado, Evangelia S. Koumousi, Corine Mathonière, and Rodolphe Clérac. Switchable Fe/Co Prussian Blue Networks and Molecular Analogues. *Chem. Soc. Rev.*, pages 203–224, 2016. (see pp. 19, 20, 21, 22, 23, 24, 35, 38, 39, 71, 72, 97, 99 and 109)

[10] Hiroko Tokoro and Shin-ichi Ohkoshi. Novel Magnetic Functionalities of prussian Blue Analogs. *Dalton Trans.*, 40(26):6825–6833, 2011. (see pp. 19, 20 and 38)

[11] Abhishake Mondal, Yanling Li, Mannan Seuleiman, Miguel Julve, Loïc Toupet, Marylise Buron-Le Cointe, and Rodrigue Lescouëzec. On/Off Photoswitching in a Cyanide-Bridged $\{Fe_2Co_2\}$ Magnetic Molecular Square. *J. Am. Chem. Soc.*, 135(5):1653–1656, February 2013. (see pp. 19, 39, 71 and 108)

[12] Juan M Herrera, Anne Bachschmidt, Françoise Villain, Anne Bleuzen, Valérie Marvaud, Wolfgang Wernsdorfer, and Michel Verdaguer. Mixed Valency and Magnetism in Cyanometallates and Prussian Blue Analogues. *Philos. Trans. Roy. Soc., A*, 366(1862):127–138, January 2008. (see p. 20)

[13] Melvin B Robin. The Color and Electronic Configurations of prussian Blue. *Inorg. Chem.*, 1(2):337–342, 1962. (see p. 20)

[14] Anne Bleuzen, Claire Lomenech, Virginie Escax, Françoise Villain, François Varret, Christophe Cartier dit Moulin, and Michel Verdaguer. Photoinduced Ferrimagnetic Systems in Prussian Blue Analogues $C^{i}_{x}Co_4[Fe(CN)_6]_y$ (C^{i} = Alkali Cation). 1. Conditions to Observe the Phenomenon. *J. Am. Chem. Soc.*, 122(28):6648–6652, 2000. (see pp. 20, 21, 72, 79, 89 and 99)

[15] Virginie Escax, Anne Bleuzen, Christophe Cartier dit Moulin, Françoise Villain, Antoine Goujon, François Varret, and Michel Verdaguer. Photoinduced Ferrimagnetic Systems in Prussian Blue Analogues $C^{i}_{x}Co_4[Fe(CN)_6]_y$($C^{i}$ = Alkali Cation). 3. Control of the Photo- and Thermally Induced Electron Transfer by the $[Fe(CN)_6]$ Vacancies in Cesium Derivatives. *J. Am. Chem. Soc.*, 123(50):12536–12543, December 2001. (see pp. 20, 72 and 99)

[16] Osamu Sato, Yasuaki Einaga, T Iyoda, A Fujishima, and K Hashimoto. Cation-Driven Electron Transfer Involving a Spin Transition at Room Temperature in a Cobalt Iron Cyanide Thin Film. *J. Phys. Chem. B*, 101(20):3903–3905, 1997. (see p. 20)

[17] Osamu Sato. Optically Switchable Molecular Solids: Photoinduced Spin-Crossover, Photochromism, and Photoinduced Magnetization. *Acc. Chem. Res.*, 36(9):692–700, September 2003. (see pp. 20 and 71)

[18] Naonobu Shimamoto, Shin-ichi Ohkoshi, Osamu Sato, and Kazuhito Hashimoto. Control of Charge-Transfer-Induced Spin Transition Temperature on Cobalt-Iron Prussian Blue Analogues. *Inorg. Chem.*, 41(4):678–684, 2002. (see pp. 20, 21, 97, 99 and 100)

[19] Osamu Sato, Tomoko Kawakami, Masanobu Kimura, Shoko Hishiya, Shoichi Kubo, and Yasuaki Einaga. Electric-Field-Induced Conductance Switching in FeCo Prussian Blue Analogues. *J. Am. Chem. Soc.*, 126(41):13176–13177, 2004. (see p. 20)

[20] Vadim Ksenofontov, Georgiy Levchenko, Sergey Reiman, Philipp Gütlich, Anne Bleuzen, Virginie Escax, and Michel Verdaguer. Pressure-Induced Electron Transfer in Ferrimagnetic Prussian Blue Analogs. *Phys. Rev. B*, 68(2):024415, July 2003. (see pp. 20 and 71)

[21] Toshihiko Yokoyama, Manabu Kiguchi, Toshiaki Ohta, Osamu Sato, Yasuaki Einaga, and Kazuhito Hashimoto. Local Structure of a Trapped Photoexcited State of a Fe-Co cyanide studied by X-ray-Absorption Fine-Structure Spectroscopy. *Phys. Rev. B*, 60(13):9340, 1999. (see pp. 20, 72 and 89)

[22] Anne Bleuzen, Virginie Escax, Jean-Paul Itié, Pascal Münsch, and Michel Verdaguer. Photomagnetism in $C_xCo_4[Fe(CN)_6]_{(8+x)/3}\cdot nH_2O$ Prussian Blue Analogues: Looking for the Maximum Photo-Efficiency. *C. R. Chimie.*, 6(3):343–352, March 2003. (see pp. 20, 99 and 109)

[23] Virginie Escax, Anne Bleuzen, Jean Paul Itié, Pascal Münsch, François Varret, and Michel Verdaguer. Nature of the Long-Range Structural Changes Induced by the Molecular Photoexcitation and by the Relaxation in the Prussian Blue Analogue $Rb_{1.8}Co_4[Fe(CN)_6\ ]_{3.3}\cdot 13H_2O$. A Synchrotron X-ray Diffraction Study. *J. Phys. Chem. B*, 107(20):4763–4767, May 2003. (see p. 89)

[24] Anne Bleuzen, Virginie Escax, Alban Ferrier, Françoise Villain, Michel Verdaguer, Pascal Münsch, and Jean-Paul Itié. Thermally Induced Electron Transfer in a CsCoFe Prussian Blue Derivative: The Specific Role of the Alkali-Metal Ion. *Angew. Chem., Int. Ed.*, 43(28):3728–3731, July 2004. (see p. 99)

[25] Virginie Escax, Guillaume Champion, Marie-Anne Arrio, Michele Zacchigna, Christophe Cartier dit Moulin, and Anne Bleuzen. The Co Ligand Field: A Key Parameter in Photomagnetic CoFe Prussian Blue Derivatives. *Angew. Chem., Int. Ed.*, 44(30):4798–4801, July 2005. (see pp. 20, 21, 22, 74, 78, 79, 102 and 109)

[26] Christophe Cartier dit Moulin, François Villain, Anne Bleuzen, Marie-Anne Arrio, Ph. Sainctavit, Claire Lomenech, Virginie Escax, François Baudelet, Elizabeth Dartyge, Jean-Jacques Gallet, and Michel Verdaguer. Photoinduced Ferrimagnetic Systems in Prussian Blue Analogues $C^i{}_xCo_4[Fe(CN)_6]_y$(C^i = Alkali Cation). 2. X-ray Absorption Spectroscopy of the Metastable State. *J. Am. Chem. Soc.*, 122(28):6653–6658, July 2000. (see pp. 21, 72, 78, 79, 102 and 109)

[27] Anne Bleuzen, Claire Lomenech, Anne Dolbecq, Francoise Villain, Antoine Goujon, Olivier Roubeau, Marc Nogues, Francois Varret, Francois Baudelet, Elisabeth Dartyge, C Giorgetti, J. J Gallet, Christophe Cartier dit Moulin, and M Verdaguer. Photo-Induced Electron Transfer and Magnetic Switching in CoFe Cyanides: Study of the Metastable State. *Mol. Cryst. Liq. Cryst.*, 335(1):253–262, 1999. (Not cited)

[28] Antoine Goujon, Olivier Roubeau, François Varret, Anne Dolbecq, Anne Bleuzen, and Michel Verdaguer. Photo-Excitation from Dia- to Ferri-Magnetism in a Rb-Co-

Hexacyanoferrate Prussian Blue Analogue. *Eur. Phys. J. B*, 14(1):115–124, 2000. (see pp. 80, 97, 99 and 100)

[29] Antoine Goujon, François Varret, Virginie Escax, Anne Bleuzen, and Michel Verdaguer. Thermo-Chromism and Photo-Chromism in a Prussian Blue Analogue. *Polyhedron*, 20(11):1339–1345, 2001. (see p. 21)

[30] Toshihiko Yokoyama, Toshiaki Ohta, Osamu Sato, and Kazuhito Hashimoto. Characterization of magnetic CoFe cyanides by x-ray-absorption fine-structure spectroscopy. *Phys. Rev. B*, 58(13):8257, 1998. (see pp. 21 and 89)

[31] M Hanawa, Yutaka Moritomo, A Kuriki, J Tateishi, K Kato, M Takata, and M Sakata. Coherent Domain Growth Under Photo-excitation in a prussian Blue Analogue. *J. Phys. Soc. Jap.*, 72(5):987–990, 2003. (see pp. 21 and 89)

[32] Christophe Cartier dit Moulin, Guillaume Champion, Jean-Daniel Cafun, Marie-Anne Arrio, and Anne Bleuzen. Structural Rearrangements Induced by Photoexcitation in a RbCoFe Prussian Blue Derivative. *Angew. Chem., Int. Ed.*, 46(8):1287–1289, February 2007. (see pp. 21, 74, 78, 79 and 102)

[33] Jean-Daniel Cafun, Guillaume Champion, Marie-Anne Arrio, Christophe Cartier dit Moulin, and Anne Bleuzen. Photomagnetic CoFe Prussian Blue Analogues : Role of the Cyanide Ions as Active Electron Transfer Bridges Modulated by Cyanide-Alkali Metal Ion Interactions. *J. Am. Chem. Soc.*, 132(33):11552–11559, August 2010. (see pp. 21, 22, 78, 79, 100, 102 and 109)

[34] Marie Anne Arrio, Philippe Sainctavit, Christophe Cartier dit Moulin, Tala Mallah, Michel Verdaguer, E. Pellegrin, and Chien-Te Chen. Characterization of Chemical Bonds in Bimetallic Cyanides using X-ray Absorption Spectroscopy at $L_{2,3}$ edges. *J. Am. Chem. Soc.*, 118(27):6422–6427, 1996. (see pp. 22, 24, 42 and 59)

[35] Sylvie Ferlay, Talal Mallah, R. Ouahès, P. Veillet, and Michel Verdaguer. A Room-Temperature Organometallic Magnet Based on Prussian Blue. *Nature*, 378(6558):701–703, 1995. (see pp. 22 and 38)

[36] Marie Anne Arrio, Philippe Sainctavit, Christophe Cartier dit Moulin, Christian Brouder, Frank De Groot, Talal Mallah, and Michel Verdaguer. Measurement of Magnetic Moment at the Atomic Scale in a High Tc Molecular Based Magnet. *J. Phys. Chem.*, 100(11):4679–4684, 1996. (see p. 22)

[37] Rosalie K. Hocking, Erik C. Wasinger, Frank M. F. de Groot, Keith O. Hodgson, Britt Hedman, and Edward I. Solomon. Fe L-Edge XAS Studies of $K_4[Fe(CN)_6]$ and $K_3[Fe(CN)_6]$: A Direct Probe of Back-Bonding. *J. Am. Chem. Soc.*, 128(32):10442–10451, August 2006. (see pp. 22, 36, 42, 43, 45, 62, 63, 74, 78, 102 and 109)

[38] Zhan Shu-zhong, Chen Xiao-yuan, Meng Qing-jin, and Xie Wei. Synthesis, Characterization and Electrochemical Properties of Cyanide-Bridged Cobalt (III)/iron(II) Complexes. *Syn. React. Inorg. Met.*, 26(2):277–284, 1996. (see pp. 23 and 71)

[39] Paul V. Bernhardt and Manuel Martinez. The First Structurally Characterized Discrete Dinuclear μ-Cyano Hexacyanoferrate Complex. *Inorg. Chem.*, 38(3):424–425, February 1999. (Not cited)

[40] Paul V. Bernhardt, Brendan P. Macpherson, and Manuel Martinez. Discrete Dinuclear Cyano-Bridged Complexes. *Inorg. Chem.*, 39(23):5203–5208, November 2000. (see pp. 23 and 71)

[41] Curtis P Berlinguette, Alina Dragulescu-Andrasi, Andreas Sieber, José Ramón Galán-Mascarós, Hans-Ulrich Güdel, Catalina Achim, and Kim R Dunbar. A Charge-Transfer-Induced Spin Transition in the Discrete Cyanide-Bridged Complex $\{[Co(tmphen)_2]_3\ Fe(CN)_6]_2\}$. *J. Am. Chem. Soc.*, 126(20):6222–6223, 2004. (see pp. 23 and 71)

[42] Kristen E Funck, Andrey V Prosvirin, Corine Mathonière, Rodolphe Clérac, and Kim R Dunbar. Light-Induced Excited Spin State Trapping and Charge Transfer in Trigonal Bipyramidal Cyanide-Bridged Complexes. *Inorg. Chem.*, 50(7):2782–2789, 2011. (see pp. 23 and 71)

[43] Dongfeng Li, Rodolphe Clérac, Olivier Roubeau, Etienne Harté, Corine Mathonière, Rémy Le Bris, and Stephen M. Holmes. Magnetic and Optical Bistability Driven by Thermally and Photoinduced Intramolecular Electron Transfer in a Molecular Cobalt-Iron Prussian Blue Analogue. *J. Am. Chem. Soc.*, 130(1):252–258, January 2008. (see pp. 23, 35, 39, 71 and 108)

[44] Rémy Le Bris, Jean-Daniel Cafun, Corine Mathonière, Anne Bleuzen, and Jean-François Létard. Optical and Magnetic Properties of the Photo-induced State in the Coordination Network $Na_2Co_4[Fe(CN)_6]_{3.3}{\cdot}14H_2O$. *New J. Chem.*, 33(6):1255, 2009. (see p. 23)

[45] Yuanzhu Zhang, Dongfeng Li, Rodolphe Clérac, Marguerite Kalisz, Corine Mathonière, and Stephen M. Holmes. Reversible Thermally Photoinduced Electron Transfer in a Cyano-Bridged $\{Fe_2\ Co_2\}$ Square Complex. *Angew. Chem. Int. Ed.*, 149(22):3752–3756, April 2010. (see pp. 23, 24, 35, 39, 71 and 108)

[46] Yuan-Zhu Zhang, Philip Ferko, Diana Siretanu, Rodica Ababei, Nigam P. Rath, Michael J. Shaw, Rodolphe Clérac, Corine Mathonière, and Stephen M. Holmes. Thermochromic and Photoresponsive Cyanometalate Fe/Co Squares: Toward Control of the Electron Transfer Temperature. *J. Am. Chem. Soc.*, 136(48):16854–16864, December 2014. (see pp. 23, 35, 39, 71 and 108)

[47] Diana Siretanu, Dongfeng Li, Lionel Buisson, Dario M Bassani, Stephen M Holmes, Corine Mathonière, and Rodolphe Clérac. Controlling Thermally Induced Electron Transfer in Cyano-Bridged Molecular Squares: From Solid State to Solution. *Chem.–A Eur. J.*, 17(42):11704–11708, 2011. (see p. 23)

[48] Norihisa Hoshino, Fumichika Iijima, Graham N. Newton, Norifumi Yoshida, Takuya Shiga, Hiroyuki Nojiri, Akiko Nakao, Reiji Kumai, Youichi Murakami, and Hiroki Oshio. Three-Way Switching in a Cyanide-Bridged [CoFe] chain. *Nat. Chem.*, 4(11):921–926, September 2012. (see pp. 23 and 71)

[49] Evangelia S. Koumousi, Ie-Rang Jeon, Qian Gao, Pierre Dechambenoit, Daniel N. Woodruff, Pascal Merzeau, Lionel Buisson, Xiaolu Jia, Dongfeng Li, Florence Volatron, Corine Mathonière, and Rodolphe Clérac. Metal-to-Metal Electron Transfer in Co/Fe Prussian Blue Molecular Analogues: The Ultimate Miniaturization. *J. Am. Chem. Soc.*, 136(44):15461–15464, November 2014. (see pp. 23, 24, 35, 39, 67, 68, 71, 72, 73, 74, 78, 80, 84, 94 and 108)

[50] Erik Dujardin, Sylvie Ferlay, X. Phan, C. Desplanches, Cristophe Cartier Dit Moulin, Philippe Sainctavit, François Baudelet, E. Dartyge, P. Veillet, and Michel Verdaguer. Synthesis and Magnetization of New Room-Temperature Molecule-Based Magnets: Effects of Stoichiometry on Local Magnetic Structure by X-ray Magnetic Circular Dichroism. *J. Am. Chem. Soc.*, 120(44):11347–11352, 1998. (see pp. 24, 27 and 31)

[51] Guillaume Champion, Virginie Escax, Christophe Cartier dit Moulin, Anne Bleuzen, Françoise Villain, François Baudelet, Elisabeth Dartyge, and Michel Verdaguer. Photoinduced ferrimagnetic systems in prussian blue analogues $C^{i}_{x}Co_4[Fe(CN)_6]_y$($C^{i}$ = Alkali Cation). 4. Characterization of the Ferrimagnetism of the Photoinduced Metastable State by K edge X-ray Magnetic Circular Dichroism. *J. Am. Chem. Soc.*, 123(50):12544–12546, 2001. (see pp. 25, 31, 39, 72, 80, 91, 94, 97, 98, 100 and 114)

[52] Matteo Mannini, Francesco Pineider, Philippe Sainctavit, Loïc Joly, Arantxa Fraile-Rodríguez, Marie-Anne Arrio, Christophe Cartier dit Moulin, Wolfgang Wernsdorfer, Andrea Cornia, Dante Gatteschi, and Roberta Sessoli. X-Ray Magnetic Circular Dichroism Picks out Single-Molecule Magnets Suitable for Nanodevices. *Adv. Mater.*, 21(2):167–171, January 2009. (see p. 27)

[53] Andrea Cornia, Matteo Mannini, Philippe Sainctavit, and Roberta Sessoli. Chemical Strategies and Characterization tools for the Organization of Single Molecule Magnets on Surfaces. *Chem. Soc. Rev.*, 40(6):3076–3091, 2011. (see p. 27)

[54] Isabelle Letard, Ph. Sainctavit, Christophe Cartier dit Moulin, Jean-Paul Kappler, Paolo Ghigna, Dante Gatteschi, and Bruno Doddi. Remnant Magnetization of Fe8 High-Spin Molecules: X-ray Magnetic Circular Dichroism at 300 mK. *J. Appl. Phys.*, 101(11):113920, 2007. (see pp. 73, 74 and 80)

[55] Paola Ghigna, A Campana, Alessandro Lascialfari, Andrea Caneschi, Dante Gatteschi, Alberto Tagliaferri, and Francesco Borgatti. X-ray Magnetic-Circular-Dichroism Spectra on the Superparamagnetic Transition-Metal ion Clusters Mn12 and Fe8. *Phys. Rev. B*, 64(13):132413, 2001. (Not cited)

[56] Yoann Prado, Marie-Anne Arrio, Florence Volatron, Edwige Otero, Christophe Cartier dit Moulin, Philippe Sainctavit, Laure Catala, and Talal Mallah. Magnetic

Anisotropy of Cyanide-Bridged Core and Core-Shell Coordination Nanoparticles Probed by X-ray Magnetic Circular Dichroism. *Chem.–A Eur. J.*, 19(21):6685–6694, May 2013. (see pp. 24 and 27)

[57] Michael L. Baker, Yasutaka Kitagawa, Tetsuya Nakamura, Kou Tazoe, Yasuo Narumi, Yoshinori Kotani, Fumichika Iijima, Graham N. Newton, Mitsutaka Okumura, Hiroki Oshio, and Hiroyuki Nojiri. X-ray Magnetic Circular Dichroism Investigation of the Electron Transfer Phenomena Responsible for Magnetic Switching in a cyanide-bridged [CoFe] Chain. *Inorg. Chem.*, 52(24):13956–13962, December 2013. (see pp. 24, 43, 71, 97 and 100)

[58] Yoshihiro Sekine, Masayuki Nihei, Reiji Kumai, Hironori Nakao, Youichi Murakami, and Hiroki Oshio. X-ray-Induced Phase Transitions by Selective excitation of Heterometal ions in a Cyanide-bridged Fe–Co Molecular Square. *Chem Commun.*, 50(31):4050, 2014. (see pp. 24, 68, 72, 73, 79 and 83)

[59] Yoshihiro Sekine, Masayuki Nihei, Reiji Kumai, Hironori Nakao, Youichi Murakami, and Hiroki Oshio. Investigation of the Light-Induced Electron-Transfer-Coupled Spin Transition in a Cyanide-bridged [Co_2Fe_2] omplex by X-ray Diffraction and Absorption Measurements. *Inorg. Chem. Front.*, 1(7):540–543, 2014. (see pp. 24, 68, 71, 72, 73, 79, 83 and 97)

[60] Eric Beaurepaire, Fabrice Scheurer, Gérard Krill, and Jean-Paul Kappler. *Magnetism and synchrotron radiation*, volume 34. Springer, 2001. (see pp. 28 and 30)

[61] Joachim Stöhr and Hans Christoph Siegmann. Interactions of Polarized Photons with Matter. *Magnetism: From Fundamentals to Nanoscale Dynamics*, pages 351–429, 2006. (see pp. 28 and 29)

[62] Gisela Schütz, W Wagner, Wr Wilhelm, P Kienle, R Zeller, R Frahm, and G Materlik. Absorption of Circularly Polarized X-rays in Iron. *Phys. Rev. Lett.*, 58(7):737, 1987. (see p. 30)

[63] Chien-T Chen, Francesco Sette, Yanjun Ma, and Silvio Modesti. Soft-X-ray Magnetic Circular Dichroism at the $L_{2,3}$ edges of Nickel. *Phys. Rev. B*, 42(11):7262, 1990. (see p. 30)

[64] Gerrit Van der Laan. Applications of Soft X-ray Magnetic Dichroism. In *Journal of Physics: Conference Series*, volume 430, page 012127. IOP Publishing, 2013. (see p. 31)

[65] Gerrit van der Laan and Adriana I Figueroa. X-ray Magnetic Circular Dichroism—A Versatile Tool to Study Magnetism. *Coord. Chem. Rev.*, 277:95–129, 2014. (see p. 31)

[66] Karsten Kuepper, Christine Derks, Christian Taubitz, Manuel Prinz, Loïc Joly, Jean-Paul Kappler, Andrei Postnikov, Wanli Yang, Tatyana V Kuznetsova, Ulf

Wiedwald, Paul Ziemann, and Manfred Neumann. Electronic Structure and Soft-X-ray-Induced Photoreduction Studies of Iron-Based Magnetic Polyoxometalates of Type $\{(M)M_5\}_{12}Fe^{iii}_{30}$ (M= Mo^{iv}, W^{vi}). *Dalt. Trans.*, 42(22):7924–7935, 2013. (see p. 31)

[67] Oana Bunau, Marrie Anne Arrio, Philippe Sainctavit, Lorenzo Paulatto, Matteo Calandra, Amélie Juhin, Valérie Marvaud, and Christophe Cartier dit Moulin. Understanding the Photomagnetic Behavior in Copper Octacyanomolybdates. *J. Phys. Chem. A*, 116(34):8678–8683, 2012. (see p. 31)

[68] Jean-Daniel Cafun, Julien Lejeune, Jean-Paul Itié, François Baudelet, and Anne Bleuzen. XMCD at the Transition Metal K-Edges as a Probe of Small Pressure-Induced Structural Distortions in Prussian Blue Analogues. *J. Phys. Chem. C*, 117:19645–19655, September 2013. (see pp. 31 and 97)

[69] B. T. Thole, Paul Carra, Francesco Sette, and Gerrit van der Laan. X-ray Circular Dichroism as a Probe of Orbital Magnetization. *Phys. Rev. Lett.*, 68(12):1943–1946, 1992. (see pp. 31, 41, 46, 72 and 74)

[70] Paum Carra, B. T. Thole, Massimo Altarelli, and X. Wang. X-ray Circular Dichroism and Local Magnetic fields. *Phys. Rev. Lett.*, 70(5):694–697, 1993. (see pp. 31, 32, 41, 46, 72 and 74)

[71] Jan Vogel and Maurizio Sacchi. Polarization and Angular Dependence of the $L_{2,3}$ Absorption edges in Ni (110). *Phys. Rev. B*, 49(5):3230, 1994. (see p. 32)

[72] Yüksel Ufuktepe, Guvenc Akgül, Funda Aksoy, and Dennis Nordlund. Thickness and Angular Dependence of the L-edge X-ray Absorption of Nickel Thin Films. *X-Ray Spectrometry*, 40(6):427–431, 2011. (see p. 32)

[73] Gerrit van der Laan. Hitchhiker's guide to multiplet calculations. In *Magnetism: A Synchrotron Radiation Approach*, pages 143–199. Springer, 2006. (see p. 33)

[74] Robert D Cowan. *The theory of atomic structure and spectra*, volume 3. Univ. of California Press, Berkeley, CA, 1981. (see pp. 33, 41 and 74)

[75] http://www.tcd.ie/physics/people/cormac.mcguinness/cowan/. (see p. 33)

[76] Dongfeng Li, Sean Parkin, Guangbin Wang, Gordon T Yee, Andrey V Prosvirin, and Stephen M Holmes. Single-Molecule Magnets Constructed from Cyanometalates:{[Tp* $Fe^{III}(CN)_3M^{II}(DMF)_4]_2[OTf]_2$}DMF ($M^{ii}$ = Co, Ni). *Inorg. Chem.*, 44(14):4903–4905, 2005. (see p. 35)

[77] Dongfeng Li, Sean Parkin, Guangbin Wang, Gordon T. Yee, and Stephen M. Holmes. Synthesis and Spectroscopic and Magnetic Characterization of Tris(3,5-dimethylpyrazol-1-yl)borate Iron Tricyanide Building Blocks, a Cluster, and a One-Dimensional Chain of Squares. *Inorg. Chem.*, 45(5):1951–1959, March 2006. (see pp. 35, 36, 39 and 71)

[78] Dongfeng Li, Rodolphe Clérac, Sean Parkin, Guangbin Wang, Gordon T Yee, and Stephen M Holmes. An S= 2 Cyanide-Cridged Trinuclear $Fe_2^{iii}Ni^{ii}$ Single-Molecule Magnet. *Inorg. Chem.*, 45(14):5251–5253, 2006. (see pp. 35 and 36)

[79] Rodrigue Lescouëzec, Jacqueline Vaissermann, Francesc Lloret, Miguel Julve, and Michel Verdaguer. Ferromagnetic Coupling between Low- and High-Spin Iron(III) Ions in the Tetranuclear Complex*fac*-{$[Fe^{III}\{HB(pz)_3\}(CN)_2(\mu\text{-}CN)]_3Fe^{III}(H_2O)_3\}\cdot 6H_2O$([$HB(pz)_3]^-$ = Hydrotris(1-pyrazolyl)borate). *Inorg. Chem.*, 41(23):5943–5945, November 2002. (see pp. 35 and 42)

[80] B. N. Figgis, Malcolm Gerloch, and R. Mason. The Crystallography and Paramagnetic Anisotropy of Potassium Ferricyanide. *Proc. Roy. Soc. London Ser. A*, 309(1496):91–118, 1969. (see p. 35)

[81] Brian N. Figgis, B. W. Skelton, and A. H. White. Crystal tructures of the Simple Monoclinic and Orthorhombic Polytypes of Tripotassium hexacyanoferrate (III). *Aus. J. Chem.*, 31(6):1195–1199, 1978. (see pp. 35 and 36)

[82] Sadaf Fatima Jafri, , Evangelia S. Koumousi, Ph. Sainctavit, Amélie Juhin, Vivien Schuler, Oana Bunau, Mitcov Dmitri, Pierre Dechambenoite, Corine Mathonière, Rodolphe Clérac, Edwige Otero, Philippe Ohresser, Christophe Cartier dit Moulin, and Marie-Anne Arrio. Large Orbital Magnetic Moment Measured in [T_P $Fe^{III}(CN)_6]^-$ the Precursor of Photomagnetic Molecular Prussian Blue Analogues. *Inorg. Chem.*, page xxx, 2016. (see pp. 35, 36, 37, 63, 64, 80 and 102)

[83] Peter Day, Christopher D. Delfs, Brian N. Figgis, Philip A. Reynolds, and Francis Tasset. Polarized Neutron Diffraction from Cs_2 $KFe(CN)_6$: The Orbital Moment and its Anisotropy. *Mol. Phys.*, 78(4):769–780, March 1993. (see pp. 36, 49 and 63)

[84] Michel Verdaguer, A Bleuzen, C Train, R Garde, F Fabrizi de Biani, and C Desplanches. Room-Temperature Molecule-Based Magnets. *Philos. Trans. Roy. Soc., London Ser. A*, 357(1762):2959–2976, 1999. (see p. 38)

[85] Osamu Sato. Photoinduced Magnetization in Molecular Compounds. *J. Photochem. Photobiol., C: Photochem. Rev.*, 5(3):203–223, December 2004. (see pp. 38 and 71)

[86] Osamu Sato, Jun Tao, and Yuan-Zhu Zhang. Control of magnetic properties through external stimuli. *Angew. Chem. Int. Edit.*, 46(13):2152–2187, 2007. (see pp. 38 and 99)

[87] Michel Verdaguer. Molecular Electronics Emerges from Molecular Magnetism. *Science*, 272(5262):698, 1996. (see pp. 38 and 71)

[88] Julio Camarero and Eugenio Coronado. Molecular vs. Inorganic Spintronics: The Role of Molecular Materials and Single Molecules. *J. Mater. Chem.*, 19(12):1678–1684, 2009. (see p. 71)

[89] Dante Gatteschi and Roberta Sessoli. Molecular Nanomagnets: The First 10 Years. *J. Magn. Magn. Mater.*, 272-276:1030–1036, May 2004. (see pp. 38 and 71)

[90] Philippe Ohresser, Edwige Otero, Fadi Choueikani, K. Chen, Stefan Stanescu, Françoise Deschamps, Thierry Moreno, Françoise Polack, B. Lagarde, Jean Pierre Daguerre, Fabrice Marteau, Fabrice Scheurer, Loïc Joly, Jean Paul Kappler, Bernard Müller, Oana Bunau, and Philippe Sainctavit. DEIMOS: A Beamline Dedicated to Dichroism Measurements in the 350–2500 eV Energy Range. *Rev. Sci. Instrum.*, 85(1):013106, January 2014. (see pp. 40, 73 and 100)

[91] Chien-T Chen, Yves U. Idzerda, H.-J. Lin, N. V. Smith, G. Meigs, E. Chaban, G. H. Ho, E. Pellegrin, and Francesco Sette. Experimental Confirmation of the X-ray Magnetic Circular Dichroism Sum rules for Iron and Cobalt. *Phys. Rev. Lett.*, 75(1):152–155, 1995. (see pp. 40, 74 and 101)

[92] Cinthia Piamonteze, Piter Miedema, and Frank M. F. de Groot. Accuracy of the Spin Sum Rule in XMCD for the Transition-Metal L edges from Manganese to Copper. *Phys. Rev. B*, 80(18):184410, NOV 2009. (see pp. 41, 46 and 50)

[93] Frank M. F. de Groot, J. C. Fuggle, B. T. Thole, and G. A. Sawatzky. 2p X-ray Absorption of 3d Transition-Metal Compounds: An Atomic Multiplet Description Including the Crystal Field. *Phys. Rev. B*, 42(9):5459–5468, September 1990. (see pp. 41, 72 and 74)

[94] Philip H. Butler. *Point group symmetry applications: methods and tables.* Springer Science & Business Media, New York, 2012. (see pp. 41, 42 and 74)

[95] Alfred Beverley Philip Lever. *Inorganic electronic spectroscopy.* Elsevier, New-York, 1984. (see p. 42)

[96] Amélie Juhin, Christian Brouder, Marie-Anne Arrio, Delphine Cabaret, Ph. Sainctavit, Etienne Balan, Amélie Bordage, Ari Seitsonen, Georges Calas, Sigrid Eeckhout, and Pieter Glatzel. X-ray Linear Dichroism in Cubic Compounds: The Case of Cr^{3+} in $MgAl_2\ O_4$. *Phys. Rev. B*, 78(19):195103, November 2008. (see pp. 42 and 88)

[97] Paul Strange and Balazs L Gyorffy. Interpretation of X-ray-Absorption Dichroism Experiments. *Phys. Rev. B*, 52(18):R13091, 1995. (see p. 46)

[98] Ruqian Wu and A. J. Freeman. Limitation of the Magnetic-Circular-Dichroism Spin Sum Rule for Transition Metals and Importance of the Magnetic Dipole Term. *Phys. Rev. Lett.*, 73(14):1994–1997, October 1994. (Not cited)

[99] Ruqian Wu, Dingsheng Wang, and A. J. Freeman. First Principles Investigation of the Validity and Range of Applicability of the X-ray Magnetic Circular Dichroism Sum Rule. *Phys. Rev. Lett.*, 71(21):3581–3584, November 1993. (see p. 46)

[100] Massimo Altarelli. Orbital-Magnetization Sum Rule for X-ray Circular Dichroism: A Simple Proof. *Phys. Rev. B*, 47(2):597, 1993. (see p. 46)

[101] Philippe Ohresser, Nicholas B. Brookes, S. Padovani, Fabrice Scheurer, and Harvé Bulou. Magnetism of Small Fe Clusters on Au(111) Studied by X-ray Magnetic Circular Dichroism. *Phys. Rev. B*, 64(10):104429, Sep 2001. (see p. 49)

[102] Pietro Gambardella, A. Dallmeyer, K. Maiti, M. C. Malagoli, W. Eberhardt, K. Kern, and C. Carbone. Ferromagnetism in One-Dimensional Monatomic Metal Chains. *Nature*, 416(6878):301–304, 2002. (Not cited)

[103] J. Bansmann, A. Kleibert, M. Getzlaff, A. F. Rodríguez, F. Nolting, C. Boeglin, and K. H. Meiwes-Broer. Magnetism of 3d Transition Metal Nanoparticles on Surfaces Probed with Synchrotron Radiation - From Ensembles Towards Individual Objects. *Phys. Status Solidi B*, 247:1152–1160, January 2010. (Not cited)

[104] Sergey Peredkov, Matthias Neeb, W. Eberhardt, J. Meyer, M. Tombers, H. Kampschulte, and G. Niedner-Schatteburg. Spin and Orbital Magnetic Moments of Free Nanoparticles. *Phys. Rev. Lett.*, 107(23):233401, November 2011. (see p. 49)

[105] Brian N Figgis and Michael A Hitchman. Ligand field theory and its applications, 2000. (see p. 49)

[106] Karl Ridier, Abhishake Mondal, Corentin Boilleau, Olivier Cador, Béatrice Gillon, Grégory Chaboussant, Boris Le Guennic, Karine Costuas, and Rodrigue Lescouëzec. Polarized Neutron Diffraction to Probe Local Magnetic Anisotropy of a Low-Spin Fe^{III} Complex. *Angew. Chem.*, 128(12):4031–4035, 2016. (see pp. 50 and 63)

[107] George Michael Sheldrick. Bruker analytical x-ray systems, 2000. (see p. 52)

[108] George Michael Sheldrick. Acta cryst. a64, 2009. (see p. 52)

[109] Stefano Sanvito. Molecular Spintronics. *Chem. Soc. Rev.*, 40(6):3336–3355, 2011. (see p. 71)

[110] Christian Joachim, James K. Gimzewski, and Ari Aviram. Electronics using Hybrid-Molecular and Mono-Molecular Devices. *Nature*, 408(6812):541–548, 2000. (see p. 71)

[111] Michael N. Leuenberger and Daniel Loss. Quantum Computing in Molecular Magnets. *Nature*, 410(6830):789–793, 2001. (see p. 71)

[112] Toshio Miyamachi, Manuel Gruber, Vincent Davesne, Martin Bowen, Samy Boukari, Loïc Joly, Fabrice Scheurer, Guillaume Rogez, Toyo Kazu Yamada, Philippe Ohresser, Eric Beaurepaire, and Wulf Wulfhekel. Robust Spin Crossover and Memristance Across a Single Molecule. *Nat. Commun.*, 3:938, July 2012. (see p. 71)

[113] Karl Ludwig Kompa and Rapheal David Levine. A Molecular Logic Gate. *Proc. Natl. Acad. Sci. U.S.A.*, 98(2):410–414, 2001. (see p. 71)

[114] Joakim Andréasson, Uwe Pischel, Stephen D. Straight, Thomas A. Moore, Ana L. Moore, and Devens Gust. All-Photonic Multifunctional Molecular Logic Device. *J. Am. Chem. Soc.*, 133(30):11641–11648, August 2011. (see p. 71)

[115] Sábastien Bonhommeau, Gábor Molnár, Ana Galet, Antoine Zwick, José-Antonio Real, John J. McGarvey, and Azzedine Bousseksou. One Shot Laser Pulse Induced Reversible Spin Transition in the Spin-Crossover Complex $[Fe(C_4H_4N_2)Pt(CN)_4]$ at Room Temperature. *Angew. Chem. Int. Ed.*, 44(26):4069–4073, June 2005. (see p. 71)

[116] Osamu Sato. Switchable Molecular Magnets. *Proc. Jpn. Acad., Ser. B, Phys. Biol. Sci.*, 88(6):213–225, 2012. (see p. 71)

[117] Tao Liu, Yan-Juan Zhang, Shinji Kanegawa, and Osamu Sato. Photoinduced Metal-to-Metal Charge Transfer toward Single-Chain Magnet. *J. Am. Chem. Soc.*, 132(24):8250–8251, June 2010. (see p. 71)

[118] Julie Mercurol, Yanling Li, Emilio Pardo, Olivia Risset, Mannan Seuleiman, Hélène Rousselière, Rodrigue Lescouëzec, and Miguel Julve. $[Fe^{II}{}_{LS}Co^{III}{}_{LS}]_2$ $[Fe^{III}{}_{LS}Co^{II}{}_{HS}]_2$ Photoinduced Conversion in a Cyanide-Bridged Heterobimetallic Molecular Square. *Chem. Commun.*, 46(47):8995, 2010. (see pp. 71 and 108)

[119] Ie-Rang Jeon, Sergiu Calancea, Anangamohan Panja, Dalice M. Piñero Cruz, Evangelia S. Koumousi, Pierre Dechambenoit, Claude Coulon, Alain Wattiaux, Patrick Rosa, Corine Mathonière, and Rodolphe Clérac. Spin Crossover or Intra-Molecular Electron Transfer in a Cyanido-Bridged Fe/Co Dinuclear Dumbbell: A Matter of State. *Chem. Sci.*, 4(6):2463, 2013. (see pp. 71 and 108)

[120] Masayuki Nihei, Yoshihiro Sekine, Naoki Suganami, and Hiroki Oshio. Thermally Two-stepped Spin Transitions Induced by Intramolecular Electron Transfers in a Cyanide-bridged Molecular Square. *Chem. Lett.*, 39(9):978–979, 2010. (see pp. 71 and 108)

[121] Ben Warner, Jenny C. Oberg, Tobias G. Gill, Fadi El Hallak, Cyrus F. Hirjibehedin, Michele Serri, Sandrine Heutz, Marie-Anne Arrio, Philippe Sainctavit, Matteo Mannini, Giordano Poneti, Roberta Sessoli, and Patrick Rosa. Temperature- and Light-Induced Spin Crossover Observed by X-ray Spectroscopy on Isolated Fe(II) Complexes on Gold. *J. Phys. Chem. Lett.*, 4(9):1546–1552, May 2013. (see pp. 72 and 79)

[122] Vincent Davesne, Manuel Gruber, Toshio Miyamachi, V. Da Costa, Samy Boukari, Fabrice Scheurer, Loïc Joly, Philippe Ohresser, Edwige Otero, Fadi Choueikani, A. B. Gaspar, J. A. Real, W. Wulfhekel, M. Bowen, and Eric Beaurepaire. First Glimpse of the Soft X-ray Induced Excited Spin-State Trapping Effect Dynamics on Spin Cross-Over Molecules. *J. Chem. Phys.*, 139(7):074708, August 2013. (Not cited)

[123] Valérie Briois, Christophe Cartier dit Moulin, Philippe Sainctavit, Christian Brouder, and A.-M. Flank. Full Multiple Scattering and Crystal Field Multiplet Calculations Performed on the Spin Transition $Fe^{II}(phen)_2(NCS)_2$ Complex at the Iron K and $L_{2,3}$ X-ray Absorption Edges. *J. Am. Chem. Soc.*, 117(3):1019–1026, January 1995. (see p. 72)

[124] Paolo Dapporto, Andrea Dei, Giordano Poneti, and Lorenzo Sorace. Complete Direct and Reverse Optically Induced Valence Tautomeric Interconversion in a Cobalt-Dioxolene Complex. *Chem.–A Eur. J.*, 14(35):10915–10918, December 2008. (see p. 72)

[125] Giordano Poneti, Matteo Mannini, Lorenzo Sorace, Ph. Sainctavit, Marie-Anne Arrio, Andrei Rogalev, Fabrice Wilhelm, and Andrea Dei. X-ray Absorption Spectroscopy as a Probe of Photo- and Thermally Induced Valence Tautomeric Transition in a 1:1 Cobalt-Dioxolene Complex. *ChemPhysChem*, 10(12):2090–2095, August 2009. (see pp. 83 and 95)

[126] Giordano Poneti, Matteo Mannini, Lorenzo Sorace, Ph. Sainctavit, Marie-Anne Arrio, Edwige Otero, Julio Crisginski Cezar, and Andrea Dei. Soft-X-ray-Induced Redox Isomerism in a Cobalt Dioxolene Complex. *Angew. Chem. Int. Ed.*, 49:1954–1957, March 2010. (see pp. 78 and 79)

[127] Giordano Poneti, Matteo Mannini, Brunetto Cortigiani, Lorenzo Poggini, Lorenzo Sorace, Edwige Otero, Philippe Sainctavit, Roberta Sessoli, and Andrea Dei. Magnetic and Spectroscopic Investigation of Thermally and Optically Driven Valence Tautomerism in Thioether-Bridged Dinuclear Cobalt–Dioxolene Complexes. *Inorg. Chem.*, 52(20):11798–11805, October 2013. (see pp. 72 and 79)

[128] Matteo Mannini, Francesco Pineider, Ph. Sainctavit, Loïc Joly, Arantxa Fraile-Rodríguez, Marie-Anne Arrio, Christophe Cartier dit Moulin, Wolfgang Wernsdorfer, Andrea Cornia, Dante Gatteschi, and Roberta Sessoli. X-Ray Magnetic Circular Dichroism Picks out Single-Molecule Magnets Suitable for Nanodevices. *Adv. Mater.*, 21(2):167–171, January 2009. (see p. 73)

[129] José Goulon, Andrei Rogalev, Fabrice Wilhelm, Nicolas Jaouen, Chantal Goulon-Ginet, and Christian Brouder. Optical Activity Probed with X-rays. *Journal of Physics: Condensed Matter*, 15(5):S633, 2003. (see pp. 73 and 88)

[130] José Goulon, Andrei Rogalev, Christophe Gauthier, Chantal Goulon-Ginet, Sté phane Paste, Riccardo Signorato, Claus Neumann, Laurence Varga, and Cécile Malgrange. Instrumentation Developments for X-ray Linear and Circular Dichroism at the ESRF Beamline ID12a. *Journal of Synchrotron Radiation*, 5(3):232–238, May 1998. (see pp. 73 and 88)

[131] Christian Brouder and Jean-Paul Kappler. Prolegomena to Magnetic Circular Dichroism in X-ray Absorption Spectroscopy. *Magnetism and Synchrotron Radiation*, pages 19–32, 1997. (see pp. 73 and 101)

[132] Frank de Groot. Multiplet Effects in X-ray Spectroscopy. *Coord. Chem. Rev.*, 249(1):31–63, 2005. (see p. 74)

[133] Frank De Groot and Akio Kotani. *Core level spectroscopy of solids*. CRC press, 2008. (see p. 74)

[134] B. T. Thole and Gerrit Van der Laan. Linear relation between x-ray absorption branching ratio and valence-band spin-orbit expectation value. *Phys. Rev. A*, 38(4):1943, 1988. (see p. 77)

[135] B. T. Thole and Gerrit Van der Laan. Branching ratio in x-ray absorption spectroscopy. *Phys. Rev. B*, 38(5):3158, 1988. (see p. 77)

[136] Sébastien Bonhommeau, Niko Pontius, Saioa Cobo, Lionel Salmon, Frank MF de Groot, Gábor Molnár, Azzedine Bousseksou, Hermann A Dürr, and Wolfgang Eberhardt. Metal-to-Ligand and Ligand-to-Metal Charge Transfer in Thin Films of Prussian Blue Analogues Investigated by X-ray Absorption Spectroscopy. *Phys. Chem. Chem. Phys.*, 10(38):5882–5889, 2008. (see pp. 78 and 97)

[137] Giordano Poneti, Lorenzo Poggini, Matteo Mannini, Brunetto Cortigiani, Lorenzo Sorace, Edwige Otero, Philippe Sainctavit, Agnese Magnani, Roberta Sessoli, and Andrea Dei. Thermal and Optical Control of Electronic States in a Single Layer of Switchable Paramagnetic Molecules. *Chem. Sci.*, 6(4):2268–2274, 2015. (see p. 79)

[138] Tami E. Westre, Pierre Kennepohl, Jane G. DeWitt, Britt Hedman, Keith O. Hodgson, and Edward I. Solomon. A Multiplet Analysis of Fe K-edge 1s $\rightarrow$ 3d Pre-edge Features of Iron Complexes. *J. Am.Chem. Soc.*, 119(27):6297–6314, 1997. (see pp. 83, 88 and 89)

[139] Olivier Mathon, François Baudelet, Jean Paul Itié, Sébastien Pasternak, Alain Polian, and Sakura Pascarelli. Xmcd Under Pressure at the Fe K edge on the Energy-Dispersive Beamline of the ESRF. *J. Syn. Rad.*, 11(5):423–427, 2004. (see p. 88)

[140] Andrei Rogalev, José Goulon, Chantal Goulon-Ginet, and Cécile Malgrange. Instrumentation Developments for Polarization Dependent X-ray Spectroscopies. In *Magnetism and Synchrotron Radiation*, pages 60–86. Springer, 2001. (see p. 88)

[141] Marie Anne Arrio, Stéphanie Rossano, Christian Brouder, Laurence Galoisy, and George Calas. Calculation of Multipole Transitions at the Fe K Pre-Edge through p - d Hybridization in the Ligand Field Multiplet model. *Europhys. Lett.*, 51(4):454–460, August 2000. (see pp. 88, 89 and 95)

[142] Anne Bleuzen, Jean-Daniel Cafun, Anne Bachschmidt, Michel Verdaguer, Pascal Münsch, François Baudelet, and Jean-Paul Itié. CoFe Prussian Blue Analogues under Variable Pressure. Evidence of Departure from Cubic Symmetry: X-ray Diffraction and Absorption Study. *J. Phys. Chem. C*, 112(45):17709–17715, November 2008. (see pp. 89 and 97)

[143] Isabelle Maurin, Dmitry Chernyshov, François Varret, Anne Bleuzen, Hiroko Tokoro, Kazuhito Hashimoto, and Shin-ichi Ohkoshi. Evidence for Complex Multistability in Photomagnetic Cobalt Hexacyanoferrates from Combined Magnetic and Synchrotron

X-ray Diffraction Measurements. *Phys. Rev. B*, 79(6):064420, 2009. (see pp. 89 and 97)

[144] Daniel M Pajerowski, V Ovidiu Garlea, Elisabeth S Knowles, Matthew J Andrus, Matthieu F Dumont, Yitzi M Calm, Stephen E Nagler, Xin Tong, Daniel R Talham, and Mark W Meisel. Magnetic Neutron Scattering of Thermally Quenched K-Co-Fe Prussian Blue Analog Photomagnet. *Phys. Rev. B*, 86(5):054431, 2012. (see pp. 97, 98 and 100)

[145] Virginie Escax, Christophe Cartier dit Moulin, Françoise Villain, Guillaume Champion, Jean-Paul Itié, Pascal Münsch, Michel Verdaguer, and Anne Bleuzen. Photoinduced electron transfer in ferrimagnetic Prussian-blue analogues $X^{I}{}_{x}Co_4[Fe(CN)_6]_y$ (X^{I} = alkali cation). *C. R. Chim.*, 6(8-10):1165–1173, August 2003. (see p. 99)

[146] Anne Bleuzen, Jean-Daniel Cafun, Anne Bachschmidt, Michel Verdaguer, Pascal Münsch, François Baudelet, and Jean-Paul Itié. CoFe Prussian Blue Analogues under Variable Pressure. Evidence of Departure from Cubic Symmetry: X-ray Diffraction and Absorption Study. *J. Phys. Chem. C*, 112(45):17709–17715, November 2008. (see p. 99)

[147] Patrick Franz, Christina Ambrus, Andreas Hauser, Dmitry Chernyshov, Marc Hostettler, Jürg Hauser, Lukas Keller, Karl Krämer, Helen Stoeckli-Evans, Philip Pattison, Hans-Beat Bürgi, and Silvio Decurtins. Crystalline, Mixed-Valence Manganese Analogue of Prussian Blue: Magnetic, Spectroscopic, X-ray and Neutron Diffraction Studies. *J. Am. Chem. Soc.*, 126(50):16472–16477, 2004. (see p. 100)

[148] Sadaf Fatima Jafri, , Evangelia S. Koumousi, Marie-Anne Arrio, Amélie Juhin, , Mathieu Rouzières, Pierre Dechambenoite, Corine Mathonière, Rodolphe Clérac, Edwige Otero, Fabrice Wilhelm, Andrei Rogalev, Loïc Joly, Jean-Paul Kappler, Christophe Cartier dit Moulin, and Ph. Sainctavit. Atomic Scale Evidence of the Switching Mechanism in a Photomagnetic CoFe Dinuclear Prussian Blue Analogue. *J. Am. Chem. Soc.*, page xxx, 2016. (see pp. 100 and 103)

[149] Masayuki Nihei, Yoshihiro Sekine, Naoki Suganami, Kento Nakazawa, Akiko Nakao, Hironori Nakao, Youichi Murakami, and Hiroki Oshio. Controlled intramolecular electron transfers in cyanide-bridged molecular squares by chemical modifications and external stimuli. *J. Am. Chem. Soc.*, 133(10):3592–3600, 2011. (see p. 108)